CELLS ON GRIDS OF NANOSTRUCTURES: FROM SINGLE CELL DISTORTION QUANTIFICATION TO CELL ENSEMBLE TOXICITY ASSAYS

JÜRGEN STEPHAN

München 2018

CELLS ON GRIDS OF NANOSTRUCTURES: FROM SINGLE CELL DISTORTION QUANTIFICATION TO CELL ENSEMBLE TOXICITY ASSAYS

JÜRGEN STEPHAN

Dissertation
Fakultät für Physik
Ludwig-Maximilians-Universität

vorgelegt von
Jürgen Stephan
aus Annaberg-Buchholz

München, den 30. November 2018

ERSTGUTACHTER: Prof. Joachim Rädler
ZWEITGUTACHTER: Prof. Eva Weig
TAG DER MÜNDLICHEN PRÜFUNG: 21.03.2019

"Men say they know many things;
But lo! they have taken wings, —
The arts and sciences,
And a thousand appliances;
The wind that blows
Is all that any body knows"

Henry David Thoreau, *Walden*, 1854

ZUSAMMENFASSUNG

Die Nanotechnologie und insbesondere nanostrukturierte Oberflächen haben sich als vielversprechende Werkzeuge für Sensoranwendungen in der zellbasierten Forschung herausgestellt. Zwei Bereiche, in denen bestehende Techniken von dem Einsatz nanostrukturierter Oberflächen profitieren können, sind die Lokalisationsmikroskopie und das Wirkstoffscreening. Die Zugkraftmikroskopie und die Fluoreszenzlokalisationsmikroskopie basieren auf der genauen und präzisen Erfassung von Marker-Positionen. Sie werden jedoch durch optische Brechung beim Mikroskopieren durch die Probe hindurch beeinträchtigt, was die Genauigkeit der Messung einschränkt. Beim Wirkstoffscreening werden zellbasierte Testverfahren zur Untersuchung der Zytotoxizität eingesetzt. Häufige Limitationen solcher Testverfahren sind die Notwendigkeit von Markern oder speziellen Kulturschalen und die Tatsache, dass sie oft nur eine einzige Endpunktauswertung liefern.

In dieser Arbeit werden nanostrukturierte Oberflächen als neuartige optische Sensorwerkzeuge in der *in vitro* Zellbiologie eingesetzt. Zunächst wird eine Quantifizierung der Zell-induzierten Verzerrungen vorgenommen, indem die Zellen direkt auf einem nanostrukturierten Substrat platziert werden. Dabei fungieren die Nanostrukturen als Referenzpunkte und ihre optischen Verschiebungen, die durch die Brechung an der Zelle entstehen, werden mit einer Genauigkeit von wenigen Nanometern gemessen. Um diese Einzelzell-induzierten Verzerrungen zu korrigieren, wird eine Relation zwischen dem Brechungsindex der Zelle, ihrer 3D-Form und den Zell-induzierten Verzerrungen durch geometrische Optik hergestellt. Durch die Messung der 3D-Zellenform ermöglicht die eingeführte Relation die Korrektur von Bildverzerrungen, indem sie die erwarteten Verzerrungen berechnet und das Bild entsprechend entzerrt. Umgekehrt wird die Relation als neuartiges Verfahren zur markerfreien 3D-Zellformrekonstruktion aus einem einzigen Bild genutzt.

Zweitens wird ein beugungsbasiertes Wirkstoff-Screening-Verfahren ohne die oben genannten Nachteile eingeführt. Dabei fungieren die periodischen Nanostrukturen als Beugungsgitter. Ein Laser beleuchtet das Gitter und die Intensität eines Beugungsmaxiums wird aufgezeichnet. Durch Zellen in die Nähe des Beugungsgitters wird die Interferenzbedingung des gebeugten Laserlichts verändert, da die Zellen als Phasenobjekte wirken, die auch Licht absorbieren und brechen. Es wird ein optisches Modell vorgestellt, das diese physikalischen Größen berücksichtigt. In Folge dessen wird gezeigt, dass die gemessene Intensität des Beugungsmaxiums gut mit der Modellvorhersage übereinstimmt. Daher wird das Verfahren zur Messung der Zellproliferation und der zellmorphologischen Veränderungen von Zell-Ensembles eingesetzt. Das Verfahren wird außerdem verwendet, um Krebszellen auf Reaktionen auf Dimethylsulfoxid und Cisplatin

zu untersuchen. Darüber hinaus wird der gebaute Aufbau verwendet, um Zellmorphologieänderungen an Medikamenten nicht nur mit 2D adhärenten Zellen, sondern auch in 3D-Zellkulturen zu messen, wobei dieselben Kulturschalen verwendet werden. Dies bietet die Möglichkeit, Zellantworten innerhalb der beiden Frameworks ohne systematische Fehler, die durch die Arbeit mit verschiedenen Setups entsteht, zu vergleichen.
Zusammen zeigen die in dieser Arbeit vorgestellten Ergebnisse, dass periodische Nanostrukturen als optische Abbildungs- und Beugungssensoren mit Gewinn in der zellbasierten Forschung eingesetzt werden können.

ABSTRACT

Nanotechnology and in particular nano-structured surfaces emerge as promising tools for sensing applications in cell-based research. Two areas where existing techniques can benefit from employing nano-structured surfaces are localization microscopy and drug screening. Traction force microscopy and fluorescence localization microscopy rely on accurate and precise detection of marker positions. However, they are distorted due to optical refraction when imagining through the specimen, thus limiting the accuracy of the measurement. In drug screening, cell-based assays are utilized to study cytotoxicity. Common limitations of such assays are the need for labels or specialized culture dishes and the fact that they often only provide a single endpoint readout.

In this thesis, nano-structured surfaces are utilized as novel optical sensing tools in *in vitro* cell biology. First, a quantification of cell-induced distortions is provided by placing the cells directly on a nano-structured substrate. The nanostructures hereby act as reference points and their optical displacements, occurring due to refraction at the cell, are measured with an accuracy of a few nanometers. To correct for these single-cell-induced distortions, a relation between the cell's refractive index, its 3D shape, and the cell-induced distortions is derived from geometrical optics. Through the measurement of the 3D cell shape, the introduced relation allows correcting image distortions by calculating the expected distortions and remapping the image accordingly. Conversely, the relation is utilized as a novel method for label-free 3D cell shape reconstruction from a single image.

Second, a diffraction-based drug screening method, without the drawbacks mentioned above, is introduced. Now, the periodic nanostructures act as a diffraction grating. A laser illuminates the grating, and the intensity of a diffraction peak is recorded. By bringing cells into the vicinity of the diffraction grating, the interference condition of the diffracted laser-light is changed, as the cells act as phase objects, which also absorb and refract light. An optical model is introduced that incorporates these physical quantities. It is shown that the measured diffraction peak intensity correlates well with the model prediction. Therefore, the method is employed to measure cell-proliferation and cell-morphology changes of cell ensembles. The method is also used to screen cancer cells for drug responses to dimethyl sulfoxide and cisplatin. Additionally, the built setup is utilized to measure cell morphology changes to drugs not only with 2D adherent cells but also in 3D cell culture, using the same culture dishes. This provides an opportunity to compare cell-responses within these two frameworks, without the bias introduced by working with different setups.

Together, the results presented here show that periodic nanostructures can be employed as imaging- and diffraction-sensors in cell-based research.

CONTENTS

Part I

INTRODUCTION, CONCEPTS AND BASIC THEORY

1 INTRODUCTION

1.1 MOTIVATION

One fundamental part of how we humans understand the world around us is by sensing our surroundings. We perform this sensing by seeing, hearing, smelling, feeling or tasting. Seeing, in particular, defines how we interact with our surroundings from childhood onward. It is fascinating how the mechanisms of seeing and the working principle of the human eye rely on the interplay of sensory and neural systems. While the geometric and optical properties of the eye allow an image to be formed on the retina, the brain needs to ‚make sense'of the visual input by correlating the complex electrical signals that the retina neurons transmit to the brain via the optical nerve. When permanently wearing image-reversing [1] or image-distorting goggles [2], the human brain can even adjust and undo the artificial image aberration and ‚make sense'of the world again. However, while this functionality is inherent to our visual sense, it is not implemented into the devices we use to optically resolve structures that are very small or far away. When working with microscopes or telescopes, we lack the feedback loop with our other senses to check whether the image we are seeing or recording ‚make sense'and whether it is optically aberrant or not. This rather phenomenological introduction points towards well understood optical effects, which occur in imaging but are only spotted by a qualitative analysis of the images, as they are not apparent by eye. In order to explain the occurrence of such effects in microscopy, a brief history of optical devices with a focus on their historic limitations is outlined. The pertinent question that follows is whether and where such error-inducing optical effects still affect microscopy today.

A Brief History of Microscopy

The first optical tools known today date back to about 750 BC and were used in ancient Egypt, Greece, and Babylon. These tools were simple lens-shaped objects, made from polished crystal. The Layard lens / Nimrud lens (see Figure 1.1 a)) is supposedly the oldest lens in the world. It was found in the Assyrian palace of Nimrud, but there is no evidence that it had any practical optical applications [3]. However, there are other lenses from around the same time, providing magnification of about $2.5 - 10$ times [4] that are thought to have been used for magnification or for making fire. In the course of the following centuries, there is very little evidence of optical tools. The first reliable evidence of the use of a magnification device dates back to the Roman empire in the 1st century AD. Seneca fa-

mously wrote that *"Letters, however small and indistinct, are seen enlarged and more clearly through a globe of glass filled with water"* [5]. It took another 900 years until the next practical improvement was made and so-called ‚reading stones'became widespread in the middle ages at around 1000 AD. Such reading stones could be produced as plan-convex spheres from rock crystal as stone grinding advanced especially around monasteries. They are the predecessor of modern magnifying glasses. These first visual aids were used to read by presbyopic monks [6] and were later developed further to spectacles or reading glasses in Venice and Florence.

The era of scientific use of optical devices began with the invention of the microscope in Europe at around 1600. The first compound microscopes consisted of a combination of two lenses in a tube, but the inventor is unknown (see Figure 1.1 b)). There are opposing claims that the Dutch optician Zacharias Janssen, his father Hans Martens, or their rival Hans Lippershey was the original inventor. The earliest compound microscopes were used to view small insects, as the lenses were of rather poor quality and provided only low magnification. The microscopes had a limited field of view, which additionally was curved due to spherical aberrations of the imperfect lenses. Another optical effect that troubled contemporary scientists like Robert Hooke and limited the microscope resolution was chromatic aberration [5].

Although theoretically inferior, the best performing microscopes of the 17th century were simple one-lens-microscopes made by the Dutch scientist Antoni van Leeuwenhoek. Van Leeuwenhoek was not a famous scholar, but instead solved the engineering problem of creating more precise lenses with fewer aberrations [7]. His lenses were tiny glass spheres that he produced by melting glass. They had a magnification of up to 270 times. Indeed, it required 250 more years to achieve this resolution with the compound microscope. With his lenses, van Leeuwenhoek was the first to document the existence of muscle fibers, bacteria, and red blood cells [8].

In the 19th century, optical distortions of the lenses and small movements of the microscope were the limiting factors [8]. Further milestones include the production of compound lenses by Jackson Lister, which significantly reduced spherical and chromatic aberration, as well as the mass production of high-quality lenses by Carl Zeiss [8]. Theoretical understanding of microscopy was advanced by Ernst Abbe and his optical theory, acknowledging the diffraction limit of light.

In the early 20th century August Köhler vastly improved the homogeneous illumination of the sample. He was also the first person to observe fluorescence in microscopy in 1904 [9]. This lead to the construction of the first fluorescence microscopes in the first half of the 20th century. With the introduction of immunofluorescence in 1942 and the development of various fluorescent dyes, specific bio-molecules could now be visualized within a living biological specimen [9]. Simultaneously, contrast enhancing light microscopy techniques such as phase contrast microscopy, and differential interference contrast microscopy were developed. Today, super-resolution techniques in fluorescence microscopy exist, which allow imaging living

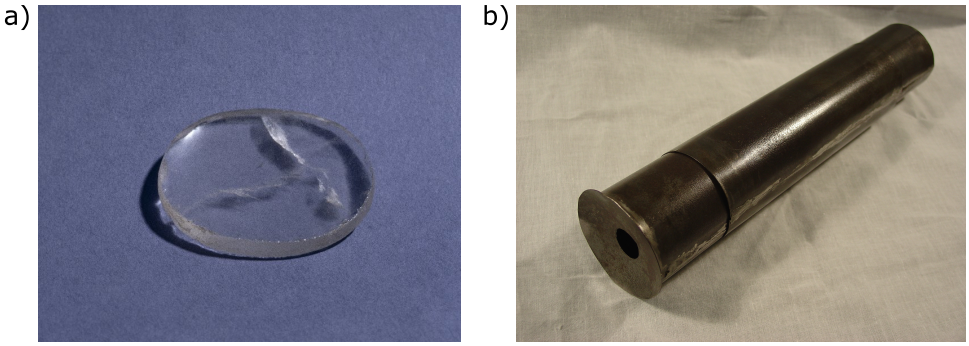

Figure 1.1: a) The Layard lens / Nimrud lens as displayed in the British Museum. The image copyright is in the public domain. b) Reproduction of an optical device that is claimed to be an early microscope which is attributed to Zacharias Janssen. Image by Alan Hawk, National Museum of Health and Medicine, Armed Forces Institute of Pathology, Department of Defense, U.S. Government - National Museum of Health and Medicine network. The image copyright is in the public domain.

specimen with a resolution of a few nanometers. With its inventors receiving the Noble Prize in Chemistry in 2014 [10], these techniques are now widely used to image small structures inside of biological tissues and resolve single molecules inside cells. However, with the increased magnification and resolution of these techniques, also the optical aberrations that have previously been corrected for lower resolutions, such as spherical aberrations and distortions, need to be eliminated with higher precision. Additionally, such microscopes are often utilized at the limit of their performance. The conditions needed to provide images without aberrations and limitations are often neglected [11].
To sum up this short walk through history: Improvements in the resolution and the image quality of optical devices has historically been linked to the ability to recognize and correct the aberrations of the optical components of the devices. The subsequent incremental steps, correct for aberrations and lead to higher resolutions and a better quality of the produced images. Even super-resolution microscopes today can still be improved upon, especially by focusing on their current limitation and the sources for aberrations.

Optical Properties of Biological Specimen

State of the art microscopy systems are optimized to be free of aberrations that originate in component imperfections or faulty alignment of these components [12]. However, there is one component in the microscopy system that cannot be optimized a priori: the specimen itself. A living biological specimen is, in fact, an optical component with varying optical properties. Such variations were not a problem in the early days of microscopy since back then a phenomenological description or a sketch of the biological specimen was sufficient. Today, phenomenological descriptions have

been supplanted by quantitative descriptions and high-resolution images. Modern microscopy systems can image into cells and resolve sub-cellular structures and single molecules inside of the cells [13]. It is possible to observe cellular processes *in vivo* or through thicker tissue with focus depths of up to 200 μm into the specimen [14]. With the advent of intracellular markers, single molecules inside the biological specimen can be tracked over time. Molecule distributions and distances between molecules can be quantitatively analyzed [15].

For such applications, the optical properties of the specimen can no longer be left aside as they can contribute to the quality and precision of the image data. There are several optical properties of biological tissues, like the refractive index or the absorption, which can influence the microscopy images. The refractive index of the specimen is typically not the same as the refractive index of the surrounding medium. Additionally, the refractive index may be subject to spatial variations within the specimen. Therefore, light refraction at the specimen boundary or inside the specimen can occur, which changes the focus of the imaging system and induces image aberrations. When imaging through thick tissue, resolution and contrast of the image can also be compromised due to the refractive index variations inside the tissue. This effect increases with the focus depth into the biological specimen and in turn limits the thickness of the observable specimen [14]. In order to address these refractive-index-induced limitations, they first have to be recognized as such. For this, a feedback loop is needed, that is able to provide a quantitative analysis of whether an image does ‚make sense'or whether it is aberrant.

In this thesis, it is proposed that nano-structured gold grids are utilized to act as a reference that can provide feedback about specimen-induced distortions in microscopy images. By imaging the nanostructures once without and once with the specimen on top of them, these nano-structured grids allow quantifying the distortions that are induced by the specimen. This framework can then be used to correct specimen-induced errors in localization microscopy techniques.

Another optical effect of biological specimens is that the phase of the light that travels through a specimen changes due to the refractive index difference between the specimen and the surrounding medium. This property does not affect localization microscopy but is utilized for example in quantitative phase microscopy [16]. In this thesis, the phase-changing properties of biological specimens are employed similarly for optical sensing. For this purpose, an interferometric setup is introduced. Here, the diffraction intensity of laser light that is diffracted on a nano-structured grid with cells on top depends, as will be shown, on the optical properties of the cells and can thus act as an indicator of cell morphology changes.

By utilizing the optical properties of the biological specimen itself, this thesis aims to employ typically unwanted optical effects to provide new sensing approaches.

1.2 SCOPE OF THIS WORK

This thesis focuses on the optical properties of single adherent cells with respect to image quality and sensing applications. The goal is first: to quantify the magnitude of the optical effects that occur when imaging through or into single cells. Second: these findings are utilized for error correction in existing localization techniques and to provide new sensing approaches. To this end, the thesis is structured into four parts.
In ***Part I*** the basic optics theory is introduced in ***Chapter 2***. In addition to summarizing image-formation- and diffraction-concepts, an overview of common microscopy methods is given, and their limitations and sources for errors are discussed. In ***Chapter 3*** the employed materials and methods are presented, and the nano-structured gold grids that are utilized throughout the thesis are introduced.
Part II summarizes the results that were achieved through the imaging of the nano-structured gold grid. ***Chapter 4*** focuses on the detection of optical distortions induced by single cells. First, the nano-structured grid and high-resolution microscopy are employed to quantify the distortion magnitude. Second, an optical model is introduced to correct these distortions in localization microscopy. In ***Chapter 5***, the introduced optical model is then used to provide a single shot, label-free 3D cell shape reconstruction from the distortion data.
In ***Part III***, the results of a diffraction-based detection of cell morphology changes, utilizing the optical properties of the cells and the diffraction of light on the grid of gold nanostructures, are summarized. To this end, the working principle of a diffraction setup for cell measurements is presented in ***Chapter 6***. Additionally, it is derived how such a diffraction setup can be utilized as an optical drug-screening assay to measure cell ensemble morphology responses in high throughput and without the need for labels. As an example, the dose-dependent responses of cell ensembles to two different drugs are measured, and the findings are assessed. In ***Chapter 7*** it is first discussed how cell culture experiments in 3D can provide a platform that is closer to *in vivo* studies than typical 2D cell culture experiments. Additionally, the current limitations for 3D assays are discussed. It is shown that the diffraction setup can provide an assay format that can measure cell responses in 2D cultures as well as in 3D hydrogels, using only standard cell culture dishes. It can thus be used to investigate the drug-response differences between 2D and 3D culture.
Finally, in ***Part IV***, the results are summarized, and an outlook to future perspectives is provided.

2

BASIC OPTICS CONCEPTS

In this chapter, a brief overview of the optical theory that is relevant to the context of this work is given. First, fundamental optical phenomena are highlighted to provide an introduction to the optical effects that are of interest when discussing light passing through the biological specimen. Second, imaging theory is introduced, and a few state-of-the-art methods for biological imaging are examined, and the limitations of these methods are highlighted. Particular interest is given to image aberrations that are induced to the imaging system by the sample (in this work, the biological specimen). In the last section of this chapter diffraction theory is discussed, again with a particular focus on the effects of a biological specimen.

Optics theory is discussed and presented in many textbooks. Therefore only a short introduction to the fundamental topics discussed in this work is given. The books by Perez [17], Klein [18] and Hecht [19] provide the primary basis for this chapter and should be consulted for a more comprehensive summary.
Historically, there are two formulations of optics theory: wave optics and geometrical optics (also called ray optics). These two formulations are founded in two fundamental principles that can be formulated independently from each other. Huygens principle provides a theory for light wave propagation and is the foundation of the wave optics theory. It states that every point of a wavefront is itself a point source of spherical wavelets. Therefore, the wave field is formed as the sum of all the point sources emitting spherical waves with the wavelength of the initial wavefront, while the wave amplitude drops linearly with the distance. Reflection and refraction can already be explained with Huygens principle, but Fermat's principle, the foundation of geometrical optics, provides an intuitive description of these phenomena. Fermat's principle originally states that light follows the path between two points in space that takes the least time. A more precise and modern formulation of the principle states that the light path between two points is stationary. To exemplify Fermat's principle and derive the optical laws that follow, one can examine light paths in different geometries. In the most straightforward case light appears to go straight from point A to point B in free space, where it travels with the speed of light c. Inside homogeneous media, light travels with a medium specific speed v. The refractive index n of an optical medium is defined based on this as the ratio between the speed of light in vacuum c and the speed of light within the medium v.

$$n \equiv \frac{c}{v} \tag{2.1}$$

It is about $n_{air} \approx 1$ for air, about $n_{water} \approx 1.33$ for water and about $n \approx$

$1.34 - 1.4$ for water-based solutions and biological specimen that have a high water content. For glass, which most optical lenses are made out of, it is about $n_{glass} \approx 1.49 - 1.66$. The optical path length OPL between A and B is now defined by the line-integral:

$$OPL(AB) \equiv \int_A^B n \, \mathrm{d}l = \int_A^B \frac{c}{v} \, \mathrm{d}l \tag{2.2}$$

For homogeneous media, this formula can be simplified to $OPL = n\Delta l$. In inhomogeneous media, the refractive index is not uniform, and the light path is curved and appears to take the optical path of least time.

$$OPL(AB) = \int_A^B n(x, y, z) \, \mathrm{d}l \tag{2.3}$$

The law of refraction can now be derived as follows: At the boundary between two homogeneous media with different refractive index, the light waves change their speed at the leading edge, thus altering the propagation direction. Following the principle of taking the path of least time, one can depict the generalized light path from a point S in a medium with refractive index n_1 to a point P in a medium with refractive index n_2 through a generalized point O on the boundary, as depicted in Figure 2.1. The total traveling time t is calculated by:

$$t = \frac{\overline{SO}}{v_1} + \frac{\overline{OP}}{v_2} \tag{2.4}$$

or:

$$t = \frac{\sqrt{h^2 + x^2}}{v_1} + \frac{\sqrt{b^2 + (a - x)^2}}{v_2} \tag{2.5}$$

For the minimum time t in relation to x, $\mathrm{d}t/\mathrm{d}x = 0$ has to hold true. Therefore it follows:

$$\frac{\mathrm{d}t}{\mathrm{d}x} = \frac{x}{v_1\sqrt{h^2 + x^2}} + \frac{-(a - x)}{v_2\sqrt{b^2 + (a - x)^2}} = 0 \tag{2.6}$$

Using the trigonometric relations, this can be rewritten to:

$$\frac{\sin \alpha_1}{v_1} = \frac{\sin \alpha_2}{v_2} \tag{2.7}$$

Using Equation 2.1, this yields Snell's law of refraction:

$$n_1 \sin \alpha_1 = n_2 \sin \alpha_2 \tag{2.8}$$

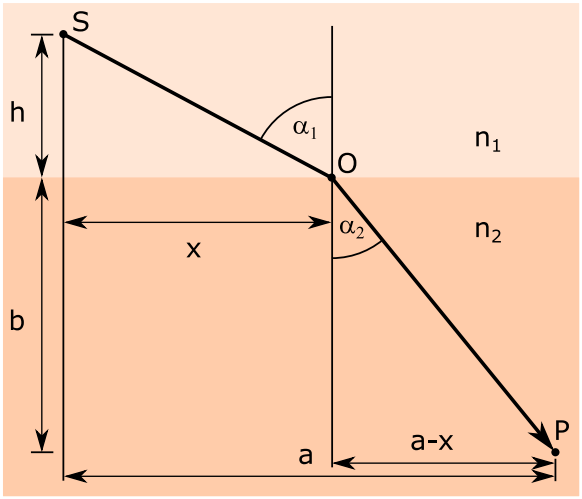

Figure 2.1: Application of Fermat's principle for the derivation of Snell's law of refraction. Figure adapted from [19]

.

2.1 IMAGING THEORY

Optical lenses are the foundation of many optical instruments, such as microscopes and telescopes. Their working principle is based on Snell's law of refraction on a curved surface. Lenses are typically made out of glass or plastics and thus have a different refractive index than air. Therefore, the light rays from a point in front of the lens are refracted on the lens surface. If a convex lens geometry is chosen correctly, all the light rays from a particular point in front of the convex lens will be refracted into another particular point behind the lens. This geometry enables lenses to image an object placed at one point in an optical system at another point in that system. For thin lenses, the relationship between its focus length f and its distances to the object s_1 and to the image s_2 is given by:

$$\frac{1}{f} = \frac{1}{s_1} + \frac{1}{s_2} \tag{2.9}$$

In wave optics, this property of a convex lens can be formulated as its ability to convert planar wavefronts into converging spherical wavefronts. Lenses are not only utilized to image objects but in particular to image small or far away objects. A key quantity of a lens is its magnification M, which is determined by:

$$M = \frac{f}{s_1 - f} = \frac{s_2 - f}{f} \tag{2.10}$$

In optical microscopes, several lenses are mounted with specific distances to each other, which together form an optical system that can image an extended object in focus onto a screen or detector with a particular magnification. However, there are some limitations to the microscope's performance.

The numerical aperture NA of an optical system is a measure of the systems ability to collect and emit light. It is defined through the maximal half-angle θ of the cone of light that can enter or exit the system times the refractive index of the medium on the object-side of the last system lens.

$$NA \equiv n \sin \theta \tag{2.11}$$

The NA is an essential parameter for microscope objectives, as it characterizes the objects ability to collect light from the sample. Due to immersion media like oil or water, which have a higher refractive index than air, modern objectives can achieve high NAs. This high NA is especially relevant as the NA also defines the resolution of an optical system. The resolution of an optical system is a quantification of the systems ability to resolve two objects that are close to each other, separately.
There are several definitions for this resolving power. The Abbe resolution limit [20] is defined by the diffraction of light on a small grid: Abbe stated that in order to resolve the grid, the principal diffraction maximum, as well as the first side maximum of the grid diffraction pattern, have to be collected by the objective. With this, he was able to formulate the resolution limit of a classical microscope with central illumination as:

$$d = \frac{\lambda}{NA} \tag{2.12}$$

Here, λ is the wavelength of the light. For cone illumination with the same objective, as in epi-setups (see Figure 2.2 b), or when illuminating the object with a condenser of equal or higher NA, the Abbe limit is defined in its most common form:

$$d = \frac{\lambda}{2NA} \tag{2.13}$$

The Rayleigh criterion formulates another definition of a microscopes resolution. When light passes through the finite aperture of an optical system, it gets diffracted and interferes with itself (analogous to the diffraction on the grid used in the Abbe limit), thereby creating a ring-shaped diffraction pattern in the image (see Section 2.3). This pattern is known as the Airy pattern. The Rayleigh criterion states that two point sources (e.g., fluorescent molecules) are defined as resolvable when the two images are at least as far apart so that the principal diffraction maximum of one image coincides with the first minimum of the other.

$$d = 1,22 \frac{\lambda}{2NA} \tag{2.14}$$

The Abbe resolution limit and the Rayleigh criterion both formulate physical resolution limit for microscope systems, due to the wave nature of

light. For light within the visible spectrum of $400\,nm - 700\,nm$, the minimal resolvable distance is thus about $d \approx 200\,nm$. Several so-called super-resolution techniques overcome this formal resolution limit and can resolve even smaller structures.

Microscopy Methods and Limitations

There is a variety of different microscopy techniques used in the life sciences. Here, a short, non-complete overview of the various methods that are used to image living biological specimen is given. Their applications and limitations are highlighted.

Bright field microscopy: From a historical perspective, bright field imaging is the most basic mode in microscopy. In bright field microscopy, the sample is illuminated with a light source from one side, and the transmitted light is imaged with the help of an objective on the opposing side of the sample (see Figure 2.2 a). This configuration is also often referred to as trans-illumination since the light is transmitted through the sample. In order to utilize transmitted light, the biological sample has to be very thin or nearly transparent. However, a sample with these specifications often does not absorb much light and thus provides nearly no contrast to the background. Therefore it often has to be stained [21].

Phase contrast microscopy, invented nearly 100 years ago by Frits Zernike [22] is a technique similar to bright field that utilizes the phase difference of the transmitted light that is scattered at the sample and converts it to an intensity difference in the image. The sample-induced phase difference originates in the difference in refractive index between the sample and its surrounding and the thus changed optical path length (see Equation 2.3). This is accomplished by using a condenser annulus that limits the angular incidence of the illumination light. The light that passes through the sample without scattering forms the background light that can be weakened by using a grey filter at the same angles as the condenser annulus after the sample. The remaining light from the sample is scattered light that covers not only the angle given by the condenser annulus but the full numerical aperture of the objective. By utilizing a phase shift ring, this light constructively interferes with the background light in the image, thereby enhancing the image contrast at the sample borders and at areas with different refractive index [23].

Differential interference contrast (DIC) is another technique utilizing phase differences to enhance image contrast. It relies on two Nomansik prims that are placed in the illumination- and the detection- light path. The prism in the illumination-light path splits the illumination light rays into two rays that are slightly apart and polarized at 90° to each other. The second prism in the detection-light path recombines the two rays, which leads to interference. Since the two rays traveled through the specimen slightly next

to each other, they also traversed slightly different parts of the specimen, which again leads to a different interference condition and an enhanced contrast at the sample areas where the optical path length gradient is high, like the sample borders.

Phase contrast microscopy and DIC, as well as bright field microscopy, are routinely used in biological imaging. They are especially applied when a quick assessment of cell morphology and motility is needed, for example in addition to fluorescence microscopy, in cell culture control [24] but also for the detection of apoptosis [25]. However, the main limitations are that these methods do not provide any quantitative measured variables and that they need an illumination light path that differs from the fluorescence light path (see below), which additionally needs spatial filters, phase rings or optical prisms. Additionally, in many sophisticated experiments, the area of interest is limited to only a small part of a cell, where optical path length differences are small [25].

Quantitative phase microscopy is a relatively new technique that allows recording phase images of biological specimen [16]. These phase images give quantitative information about the specimen-induced phase shift and provide non-invasive and label-free insight into the refractive index structure of bacteria-, blood- or tissue- cells [26]. Various sub-techniques, like diffraction phase microscopy [27], digital holographic microscopy [28] and Hilbert phase microscopy [29] exist, which even allow to reconstruct the 3D cell shape without labeling.

Fluorescence microscopy is the most commonly used technique in biological imaging. It is based on the fact that fluorescent dyes and markers can be excited by light of a certain wavelength and subsequently will emit light with a slightly shifted, higher wavelength (and thus lower energy). By filtering out the excitation light, the emitted light can be recorded separately, thereby allowing only to visualize the fluorescent dye or marker. As the background remains dark, this technique provides high sensitivity and a high signal to noise ratio. There are a plethora of fluorescence dyes at the researcher's disposal today. Cellular substructures (like the nucleus, the membrane, actin or microtubules) and single molecules can be labeled and visualized with probes spanning the entire visible spectrum [30]. Additionally, the cellular state (e.g., the cell cycle and the redox cycle), as well as cellular processes (e.g., apoptosis), can be marked with fluorescent probes [30]. With the discovery of the green fluorescent protein, it became possible to incorporate the fluorescent marker into the DNA of an organism and thus utilize it as a reporter molecule for gene expression [31].
Fluorescence microscopes are typically built in an epi-illumination (as opposed to trans-illumination) configuration as depicted in Figure 2.2 b. The sample is imaged and illuminated through the same objective. A dichroic mirror (together with an excitation- and emission-filter) is used to separate the excitation light from the emission light. This configuration provides

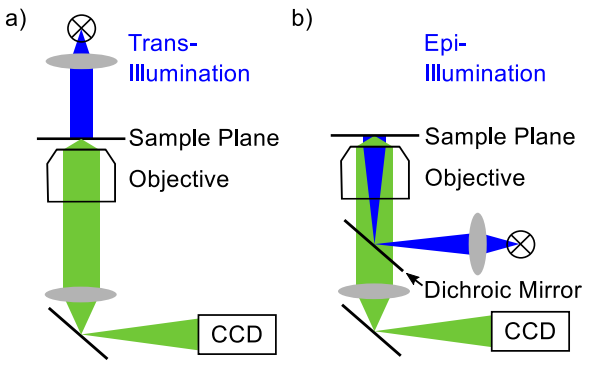

Figure 2.2: Comparison of trans- and epi-illumination microscopy: (a) Schematic of a trans-illumination microscope setup (b) Schematic of an epi-illumination microscope setup. The dichroic mirror reflects light up to a certain wavelength and transmits light with higher wavelengths.

a higher signal to noise ratio compared to the trans-illumination configuration, as most of the scattered excitation light is not directed into the imaging light path. Fluorescence microscopes can be used with widefield and confocal illumination. In widefield illumination, all illumination light is used to illuminate the sample. In confocal microscopy, a pinhole in the illumination light path is utilized to eliminate out of focus illumination and therefore suppresses background fluorescence [32]. This addition again increases the signal to noise ratio in the image but limits the speed of image acquisition as the focus spot has to be scanned across the whole sample to produce a complete image [25]. Spinning disk confocal microscopy incorporates a spinning array of rotating microlenses to increase the imaging speed [33]. Lattice light sheet microscopy is another application that offers fast imaging, while also reducing background fluorescence. The technique utilizes an illumination limited to a thin plane, the light sheet, which is aligned orthogonal to the detection light path [34]. Fluorescence microscopy however also has some drawbacks. The main one is that the fluorescence marker can alter the cellular function itself, thereby impacting measurement results [35, 36]. Additional drawbacks are induced phototoxicity and photobleaching of the fluorophores, which limit exposure times and resolution [37, 38].

Super-resolution Microscopy

The previously stated Abbe resolution limit for microscopy has been a dogma in microscopy for many years. However, in the last 20 years, techniques have been developed that can circumvent this limit and thus provided significant new insight into biological structures and processes on length scales below the diffraction limit. These techniques are summarized under the term super-resolution microscopy, and the Nobel prize in chemistry has been awarded for their development in 2014 [39]. There are three distinct approaches to super-resolution microscopy: (1) Stimulated emission depletion (STED), (2) Structured illumination microscopy (SIM)

and (3) single molecule approaches under which Photo-activated localization microscopy (PALM) and Stochastic optical reconstruction microscopy (STORM) are summarized.

STED microscopy falls under the laser scanning confocal microscopy, where the illumination laser is scanned across the sample. However, it utilizes an additional, donut-shaped depletion laser beam that switches off the excited fluorophores in the outer region of the laser beam by stimulated emission. It thereby reduces the effective excitation volume and allows to achieve a higher resolution down to 20 nm [13, 15].

In *SIM*, interference generated light patterns are utilized to form a Moire pattern illuminating the sample, from which higher-resolution information can be generated. The technique uses widefield microscopy setups and lowers the x- and y-resolution down to about 100 nm while the axial resolution remains unchanged [13, 15].

The *PALM* and *STORM* techniques are methods that utilize single molecule localization in a large number of images to reconstruct the underlying biological structure in a single frame. In order to achieve that, the fluorophores have to be well-separated from each other in the images. This separation can be achieved by utilizing photoswitchable proteins (PALM) or photoactivated organic dyes (STORM) [40]. These techniques can resolve biological structures with a resolution down to 10 nm but are reliant on a large number of subsequent images and thus can not resolve fast biological processes [13].

There is a variety of other techniques that do not belong into the super-resolution microscopy category but are still able to provide deep, but specific insight on biological samples with sub-diffraction-limited resolution. Such techniques include electron microscopy, X-ray scattering, and atomic force microscopy. As with all the other techniques, each of these methods has distinct advantages and limitations: Electron microscopy utilizes electrons instead of light to image the specimen, which provides a resolution down to 0.1 nm. However, the drawback is that electron microscopy needs to be performed under high vacuum, which excludes living specimen from the measurement. A biological specimen also has to be extensively prepared, as water has to be removed and a thin gold layer has to be evaporated onto the sample to ensure the generation of secondary electrons [41]. These processes can introduce artifacts to the specimen [42].
Another approach to lower the resolution limit is to use smaller wavelengths, e.g. X-rays. However, most substances have a refractive index very close to 1 for such wavelengths, which makes the manufacturing of x-ray optics difficult. X-rays are thus mainly used as a scattering technique that does not provide images of the sample but from which characteristic length scales can be deduced [43]. It is therefore applied to understand crystal structures but can also be utilized to investigate less ordered biological

structures like lipid membranes [44] or DNA origami [45].
Atomic force microscopy is a scanning probe technique that utilizes a cantilever with a small tip on the nanometer scale. This tip is scanned across the sample, and its deflection is recorded via laser interferometry [46]. With this technique, it is possible to scan biological samples with a vertical resolution below $1\,nm$ and an axial resolution of about $10\,nm$. It is further possible to utilize the atomic force microscope to measure forces of single molecules [47]. Main disadvantages of the technique include that as a scanning probe techniques it is inherently slow as well as that the finite size of the tip can introduce scanning artifacts.

2.2 IMAGE-ABERRATIONS AND CORRECTION

Types of Aberrations

In imaging theory, it is common to formulate equations using an approximation for light rays that are close to the optical axis, also called paraxial rays. However, in reality, not all rays in an optical system are always paraxial rays, which causes deviations from the perfect image in a measurement with that optical system. Such deviations are called optical aberrations. One can distinguish between two types of aberrations: a) chromatic aberrations that result from the wavelength-dependence of the refractive index, and b) monochromatic aberrations that result from deviations of the paraxial approximation. The monochromatic aberrations again can be split into two groups: a) aberrations that affect the image quality like spherical aberrations, coma and astigmatism and b) aberrations that distort the image.

Chromatic aberrations: When the imaging in an optical system is performed with non-monochromatic light sources, chromatic aberrations can occur. This is because light rays passing through a lens will be refracted by this lens depending on the lens radii (R_1 and R_2) and refractive index (n_l) as defined by the lensmaker's equation for thin lenses: Equation 2.15. The refractive index $n(\lambda)$ of a medium is however dependent on the wavelength of the light via $n(\lambda) = \lambda_0/\lambda$, where λ_0 is the wavelength in vacuum. Therefore different wavelengths will be refracted under slightly different angles on a normal lens, and the focus f of the lens will thus also depend on the light wavelength.

$$\frac{1}{f} = (n_l(\lambda) - 1) * \left(\frac{1}{R_1} - \frac{1}{R_2}\right) \tag{2.15}$$

In Figure 2.3 a) this is depicted schematically. The blue light is refracted more than the red light. To correct for chromatic aberrations, objectives in modern microscopes are often constructed with achromatic lens systems that combine two or more thin convex and concave lenses to cancel out the difference in focal length for to different wavelengths. For a more detailed description see e.g. [17, 19].

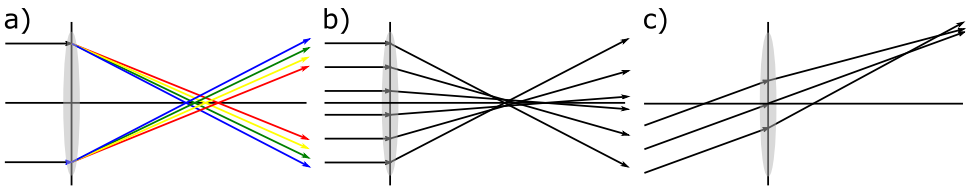

Figure 2.3: Different optical aberrations of a single lens: (a) Chromatic aberration. (b) Spherical aberration. (c) Coma.

Spherical aberrations: For light rays traveling with only a small angle difference α to the optical axis, the paraxial approximation $sin\alpha = \alpha$ is valid. Spherical aberrations arise when also the rays at the outer lens diameter contribute to the image formation. These rays will be refracted stronger than the paraxial rays and thus focus in a point closer to the lens (see Figure 2.3 b). The spatial difference in focal length depends on the aperture and the paraxial focal length of the lens, but also on the form of the lens. To minimize spherical aberration, plano-convex and combinations of convex and concave lenses are used. Furthermore, in oil-immersion objectives, the meniscus of the oil droplet is utilized not only to widen the aperture of the objective but also to minimize spherical aberrations.

Coma: Coma denotes an aberration that arises for object points, which are not on the optical axis. It originates in the fact that a bundle of parallel rays traveling parallel to the optical axis will be focused in one point by a lens (without spherical aberrations), but a bundle of parallel rays that is not parallel to the optical axis will be refracted differently on the principal plane of the lens (see Figure 2.3 c), which is not plane in reality but slightly curved. Therefore the image will be sharp in the center but blurred at the edges.

Astigmatism: Another aberration that arises for off-axis object points is astigmatism. A lens that is perpendicular to the optical axis in a specific plane is not perpendicular to the axis between an off-axis object point and the corresponding image point in the same plane. This causes the lens to be shorter in perspective and results in a shorter focal length of the lens for the off-axis object. The astigmatism of a lens depends on the angle between the object rays and the optical axis as well as the focal length, thickness, and geometry of the lens.

Field curvature: A lens that exhibits field curvature will produce a sharp image not on a flat but on a curved surface. Thus, when a planar object is imaged on an also planar surface, a lens with field curvature can only image the center of the object in focus while the outer regions will be defocused (or vice versa).

Image distortions: In contrast to the previously described aberrations, image distortions do not affect image quality. Instead, they cause the object to be

reproduced by the imaging system in a deformed shape. The origin of distortions lies in the lens geometry and the fact that different areas of a lens can have different focal lengths and magnifications. While the resulting distortions can have all kinds of shapes, there are some common distortion patterns. Examples are pincushion distortion, where the magnification of the lens gets bigger the further away from the optical axis the imaged object point is, or barrel distortion where magnification gets smaller for further away object points. In order to visualize distortions, a periodic grid can be used as an object and the discrepancies from an undistorted image can be deduced as distortions of the imaging system (see Figure 2.4).

State of the art research microscopes and specialized objectives are constructed to minimize the aberrations mentioned above for microscope optics, but since the underlying optics are also valid for any refraction at a boundary between two media with different refractive indexes, the imaged specimen itself can induce additional aberrations to the image. In order to correct for such specimen-induced aberrations, additional measures have to be taken.

Adaptive Optics for Thick Tissue Imaging

There is a variety of sources that can cause aberrations in an optical microscope. They can be summarized into three categories: imperfect optical components, faulty alignment of the optical components in the microscope, and specimen-induced aberrations [12]. The first two of these categories are allocated to the microscope fabrication process. From the theoretical design of the objective by the manufacturer to the right assembly of the microscope components, this process has been perfected in state of the art microscopes to minimize aberrations in the optical system. The third category of aberration, specimen-induced aberrations, however, can not be eliminated a priory, since these aberrations depend on the microscope application and the specimen that is imaged and in case of a living specimen can change from frame to frame. Therefore, an adaptive system that can dynamically measure and correct for these aberrations is needed. This is the purpose of adaptive optics.
Adaptive optics was first introduced to optical systems in astronomy, where earthbound telescopes, which have to image through the earth's atmosphere had to be corrected for refractive index variations in the turbulent atmosphere [48]. Adaptive optics has since also been applied in eye care [49] and more importantly for this work, in thick tissue imaging.
When imaging through thick tissue, resolution, and contrast of the image can be compromised due to refractive index variations inside the tissue. This effect increases with the depth of the specimen and in turn, limits the observable thickness of the biological specimen to only a few cellular layers near the surface [14]. To observe cellular processes *in vivo* or through thicker tissue with a thickness of up to $200\,\mu m$, adaptive optics can be

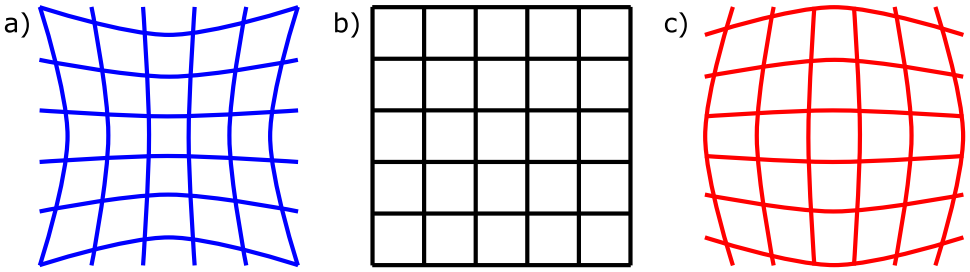

Figure 2.4: Different optical aberrations of a single lens: (a) Grid with pincushion distortion, (b) Undistorted grid. (c) Grid with barrel distortion.

applied. To visualize the working principle of adaptive optics and the effect of refractive index variations in thick specimens, one can look at the propagation of the wavefronts in the microscope. Figure 2.5 schematically depicts the planar wavefronts that are focused into spherical wavefronts by an objective (depicted by a single lens). In the un-aberrated case (a), the planar wavefronts in the pupil plane are converted into perfect spherical ones that converge in one focus spot. When there is a planar refractive index mismatch ($n_1 \neq n_2$) (b), e.g., at the interface between objective and immersion medium or when using a cover glass, the focus spot is shifted, and there is a loss of resolution and intensity [50–52]. If the focusing is done through a complex biological specimen with unknown shape and refractive index (c), the converging wavefront is distorted by the specimen and aberrations are introduced to the image. With adaptive optics, the distortion of the wavefront is corrected by introducing a non-planar wavefront in the pupil plane, which is conjugate to the wavefront distortion by the specimen and thus cancels out this distortion, forming an again perfect spherical wavefront that converges into the focus (d).
There are two different approaches to implementing adaptive optics practically in microscopy: active wavefront sensing and computational adaptive optics. In both cases, the objective is to generate a conjugate wavefront that cancels out the wavefront distortion. With active wavefront sensing, an optical element, typically a Shack-Hartmann Wavefront Sensor [48], is utilized to measure the aberrated wavefront. With the information of the shape of the aberrated wavefront, a second optical element (the adaptive element) in the optical path, either a deformable mirror or a spatial light modulator, then changes the previously planar incoming wavefront to the conjugate of the measured aberrated wavefront to correct the aberration. This active wavefront-sensing method is widely implemented in eye care and astronomy but has some drawbacks in microscopy [12]. While in astronomy an isolated guide star is utilized for the wavefront measurement, in microscopy the light often comes from different overlapping points in the specimen, making a single wavefront measurement complicated [53]. To mitigate this problem, methods that use the backscattered light [54, 55] or block the light outside the focal region e.g. through utilizing artificial guide stars [56–58], have been applied and established as adaptive optics approaches e.g. in widefield- [56–58] and two-photo-microscopy [54]. In

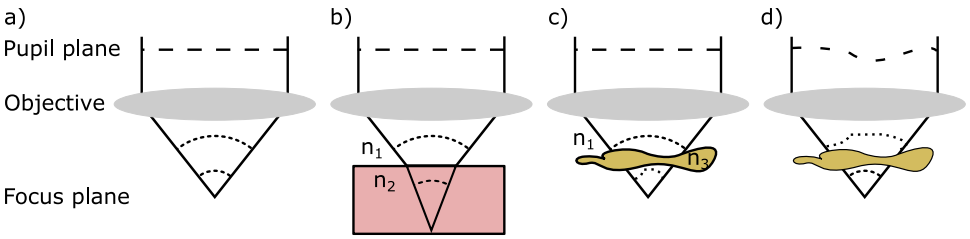

Figure 2.5: Wavefront aberration. a) Unaberrated planar wavefront in the pupil plane converges into spherical wavefront. b) Refractive index mismatch shifts the focus as the wavefront is distorted. c) Specimen-induced distortion of the wavefront. d) Adaptive optics principle of correcting the wavefront in the focus by introducing a conjugate wavefront in the pupil plan, which cancels out the wavefront distortion by the specimen. Figure adapted from [14]

computational adaptive optics, the wavefront aberration is corrected indirectly. Images are taken with the adaptive element that corrects the incoming wavefront in a series of predefined shapes. The image quality is analyzed, and the wavefront correction is iterated systematically via an active feedback loop between the image analysis and the adaptive element [53]. Alternatively, pupil segmentation can be used to find the best wavefront correction [59]. Computational adaptive optics has been successfully applied in widefield- [57], differential interference contrast- [60], two-photon [59, 61] and single-molecule switching- microscopy [62] among others.
In thick tissue imaging, adaptive optics has been used to image at depths of up to $200\mu m$ in brain tissue and up to $100\mu m$ in mouse embryo tissue [63]. Due to the correction of the aberrated wavefront, the image quality and more precisely the resolution and contrast of the previously blurred images has been improved substantially. However, imaging quality compromising specimen-induced aberrations are the only aberrations that are examined in the context of adaptive optics and thick tissue imaging. Image distortions are generally not considered and hence not well studied in biological imaging. For thin tissue, such as single cells, aberrations are generally considered to be insignificant for image quality [53], and image distortions due to optical deflection are assumed to be small [64]. However, this is an assumption that needs to be assessed critically in the context of high-resolution localization techniques, where localization with nanometer accuracy is often needed.

Aberration Analysis with Zernike-Polynominals

This subsection is summarized from Kubby et al. [12].

Aberrations can be quantified by analyzing the shape of the wavefront in the pupil plane of the lens. An ideal lens focuses a planar excitation wavefront to a diffraction-limited focal spot. When only specimen-induced refractive index variations $n(\tilde{x}, \tilde{y}, \tilde{z})$ along the light path occur, the absolute

phase Φ of a point at location $L(x,y,z)$ within the light path can be written as:

$$\Phi(L(x,y,z)) = \int_F^{L(x,y,z)} \frac{2\pi}{\lambda}\, n(\tilde{x},\tilde{y},\tilde{z})\, \mathrm{d}\omega \tag{2.16}$$

Here, the phase is given with respect to the focal point, with F denoting the position of the focal point. Additionally λ is the free space wavelength, and ω denotes the distance traveled. The wavefront aberration function $\Psi(x,y)$ in the pupil plane can now be defined as:

$$\Psi(x,y) = \int_F^{L(x,y,z_0)} \frac{2\pi}{\lambda}\, (n(\tilde{x},\tilde{y},\tilde{z}) - n_0(\tilde{x},\tilde{y},\tilde{z}))\, \mathrm{d}\omega \tag{2.17}$$

where z_0 is the axial position of the pupil plane and $n_0(\tilde{x},\tilde{y},\tilde{z})$ denotes the un-aberrated case. The established method to analyze this aberration function is to decompose it into a sum of polynomials, the so-called Zernike polynomials [65, 66] as follows:

$$\Psi(r,\theta) = \sum_{i=1}^{\infty} M_i Z_i(r,\theta) \tag{2.18}$$

M_i is a modal coefficient that describes the strength of the i-th Zernike polynomial $Z_i(r,\theta)$. The Zernike polynomials are a set of orthogonal functions defined over the unit circle. Therefore the set of Zernike coefficients M_i fully describes the aberration function $\Psi(r,\theta)$:

$$M_i = \frac{1}{\pi} \int_0^1 \int_0^{2\pi} \Psi(r,\theta)\, Z_i(r,\theta)\, r\, \mathrm{d}\theta\, \mathrm{d}r \tag{2.19}$$

Using the definition by Neil et al. [67], the Zernike polynomials can now be written by mapping of indices as follows:

$$Z_n^m(r,\theta) = \begin{cases} m < 0 : \sqrt{2} R_n^{-m}(r) \sin(-m\theta) \\ m = 0 : 0 \\ m > 0 : \sqrt{2} R_n^m(r) \cos(m\theta) \end{cases} \tag{2.20}$$

$$R_n^m(r) = \sqrt{n+1} \sum_{s=0}^{(n-m)/2} \frac{(-1)^s (n-s)!}{s!((n+m)/2-s))!\ ((n-m)/2-s)!} r^{n-2s} \tag{2.21}$$

where $n \geq |m|$ and $n - |m| = even$; i starts at 1 for $n = 0$ and rises first with n, then with the allowed absolute values for m and finally with the sign of m with the positive value going first. The first 11 Zernike polynomials are listed in Table 2.1.

Some of the Zernike polynomials correspond to the previously intro-

i	n	m	Polynomial	Aberration Term
1	0	0	1	Piston
2	1	1	$2r\cos(\theta)$	Tip
3	1	-1	$2r\sin(\theta)$	Tilt
4	2	0	$\sqrt{3}(2r^2-1)$	Defocus
5	2	2	$\sqrt{6}r^2\cos(2\theta)$	Astigmatism
6	2	-2	$\sqrt{6}r^2\sin(2\theta)$	Astigmatism
7	3	1	$2\sqrt{2}(3r^3-2r)\cos(\theta)$	Coma
8	3	-1	$2\sqrt{2}(3r^3-2r)\sin(\theta)$	Coma
9	3	3	$2\sqrt{2}r^3\cos(3\theta)$	
10	3	-3	$2\sqrt{2}r^3\sin(3\theta)$	
11	4	0	$\sqrt{5}(6r^4-6r^2+1)$	Spherical (1st)

Table 2.1: Definition of the first 11 Zernike polynomials. Table adapted from [12]

.

duced aberrations, which can thus be conveniently described and quantified by wavefront analysis. Polynomial 2 corresponds to Tip, polynomial 3 to Tilt, and polynomial 4 to Defocus. Therefore these three polynomials completely represent the geometrical distortion that is induced in the wavefront in x- (tip), y- (tilt) and z-direction (defocus). They alter the focus but do not affect the shape of the point spread function and therefore the resolution and contrast of the image. That is why they typically do not need to be corrected using adaptive optics. However, the image distortion in x-, y- and z-direction can be directly calculated from the corresponding Zernike coefficients M_2, M_3 and M_4 as follows:

$$\Delta x = -\frac{M_2\lambda}{\pi n \sin\alpha}; \quad \Delta y = -\frac{M_3\lambda}{\pi n \sin\alpha}; \quad \Delta z = -\frac{M_4\sqrt{3}\lambda}{2\pi n \sin^2(\alpha/2)} \tag{2.22}$$

where the term $n\sin\alpha$ refers to the numerical aperture of the lens. For a step by step derivation, see Kubby et al. [12].

2.3 DIFFRACTION THEORY

Introduction to Diffraction

At the beginning of this chapter, Huygens principle has already been introduced. The physical phenomenon of diffraction can be explained with this principle, but the rigorous mathematical description is given by Kirchhoff's theory and diffraction formula [43]. With Kirchhoff's formula, the light wave propagation after an aperture can be calculated. The formula can be derived by applying Green's theorem to the wave equation, as shown in, e.g. the textbook of Hecht [19]. Two approximations help to solve Kirchhoff's diffraction formula for various cases, the Fresnel approximation, and

the Fraunhofer approximation. The Fresnel approximation can be applied to the propagation of waves in the near field (i.e., in close proximity to the aperture). The Fraunhofer approximation provides the diffraction pattern at an infinite distance to the aperture but can be applied as long as it is in the far field. The diffraction experiments in this thesis are evaluated in the far field, which is why the Fraunhofer approximation is sufficient here.
In its most general form, Kirchhoff's integral under the Fraunhofer approximation is given by:

$$\Psi_p \approx \frac{a_Q\, k_0}{2\pi\, i} \frac{e^{i\, k_0 (L_1 + L_2 + \frac{p^2}{2L_2})}}{L_1\, L_2} \int\int_{aperture} f_S(x,y)\, e^{-i\, \vec{K}\cdot\vec{s}}\, \mathrm{d}x\, \mathrm{d}y \tag{2.23}$$

Here Ψ_p is the wave amplitude at a point in the image plane with a distance to the optical axis p ($\vec{p}$ points from the optical axis in the image plane to p). a_Q is the wave amplitude at the source. $k_0 = 2\pi/\lambda$ is the absolute of the wave vector, were λ is the light wavelength. L_1 is the distance between the light source and the aperture. L_2 is the distance between aperture and image plane. f_S is the aperture function. $\vec{s}$ is the vector from the optical axis in the aperture to the border of the aperture parallel to $\vec{p}$ and $\vec{K} = k_0/L_2\, \vec{p}$. Since the quantities in front of the integral are all constants, they can be summed together as C:

$$\Psi_p \approx C \int\int_{aperture} f_S(x,y)\, e^{-i\, \vec{K}\cdot\vec{s}}\, \mathrm{d}x\, \mathrm{d}y \tag{2.24}$$

This formula has the exact form of a Fourier transform (with an additional constant C in front of the integral), which makes the benefit of the Fraunhofer approximation apparent: The diffraction pattern of any aperture can be calculated by a Fourier transform of the aperture function. In the following, diffraction patterns and their intensity distributions $I(P) = |\Psi_P|^2$ for different apertures are examined. For this chapter, the Fourier transform is defined as:

$$FT(f(x)) = F(k) = \int_{-\infty}^{\infty} f(x)\, e^{2\pi\, i\, k\, x}\, \mathrm{d}x \tag{2.25}$$

The inverse transform is then defined as:

$$f(x) = \int_{-\infty}^{\infty} F(k)\, e^{-2\pi\, i\, k\, x}\, \mathrm{d}k \tag{2.26}$$

Note that the $2\,\pi$ are included in the exponent in this definition. In other definitions, they are included as a constant or placed only in the inverse transform.

Diffraction on a Single Slit

The calculations in the following subsections are summarized from the textbook of Cowley [43].

The aperture function of a single slit with width a is given by:

$$f(x) = \begin{cases} |x| > a/2 & : \quad 0 \\ |x| \leq a/2 & : \quad 1 \end{cases} \tag{2.27}$$

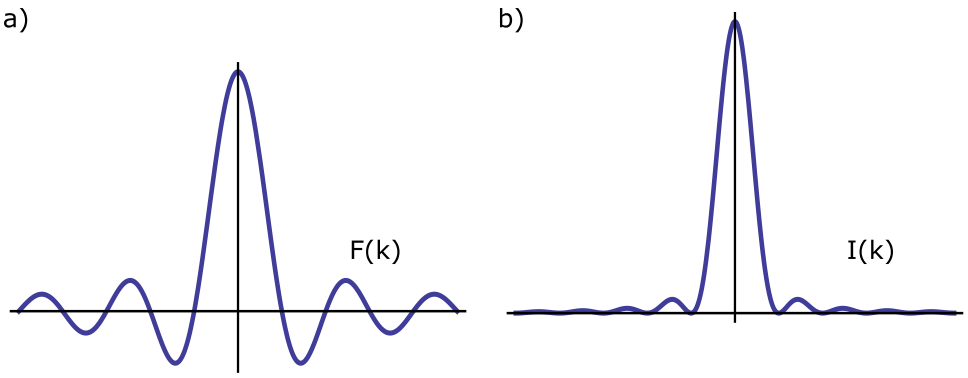

Figure 2.6: a) Normalized distribution of the electrical field under Fraunhofer diffraction on a single slit. b) Normalized intensity distribution under Fraunhofer diffraction on a single slit.

The Fourier transform is then given by:

$$F(k) = \int_{-a/2}^{a/2} e^{2\pi i k x}\,\mathrm{d}x = \frac{\sin(\pi a k)}{\pi k} \tag{2.28}$$

The intensity is distributed as:

$$I(k) = \frac{\sin^2(\pi a k)}{(\pi k)^2} \tag{2.29}$$

Diffraction on a Circular Aperture

Similar to the single slit in one dimension, a two-dimensional circular aperture has an aperture function given by:

$$f(x,y) = \begin{cases} \sqrt{(x^2+y^2)} < a/2 & : \quad 1 \\ \sqrt{(x^2+y^2)} \geq a/2 & : \quad 0 \end{cases} \tag{2.30}$$

The Fourier transform of this aperture function then yields:

$$F(k) = \frac{\pi a^2}{2} \frac{J_1(\pi a k)}{\pi a k} \tag{2.31}$$

Here, k is a radial coordinate and $J_1(x)$ is the first order Bessel function. The function $J_1(x)/x$ is similar to $sin(x)/x$ as encountered for the single slit. However, the first zero occurs not at a^{-1} but at $1.22\,a^{-1}$. The Rayleigh criterion, as already seen in Equation 2.14, is derived from this diffraction on a circular aperture. The resulting diffraction pattern, called the Airy pattern is furthermore used to describe the point spread function (PSF) of

an aperture, typically an objective lens or an imaging system. The image of an object that is imaged with an optical system is a convolution of the systems PSF and the intensity in the object plane [12]. The resolution of the image can thus be enhanced by deconvolution of the systems PSF and original image. Calculation of the PSF is sufficient in some cases, while in other cases the PSF is distorted through lens aberrations and has to be measured experimentally [68].

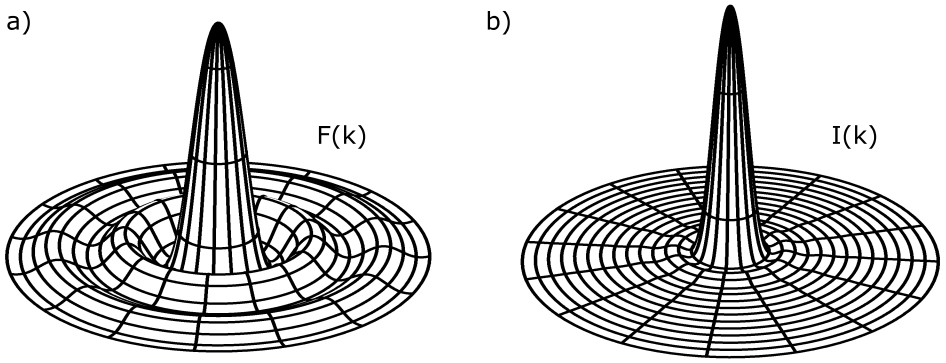

Figure 2.7: Airy pattern. a) Normalized distribution of the electrical field under Fraunhofer diffraction on a circular aperture. b) Normalized intensity distribution under Fraunhofer diffraction on a circular aperture.

Diffraction on a Double Slit

One of the most famous examples of diffraction is Young's double slit experiment, first performed in 1801. Thomas Young produced interference patterns from sunlight that got diffracted at a double slit aperture. With a single slit in front of the aperture, he was able to generate spatial coherent light rays that illuminated both slits equally. He was furthermore able to qualitatively explain the interference pattern with Huygens principle as shown in Figure 2.8. To mathematically explain the diffraction pattern within the Fraunhofer approximation, the convolution theorem has to be introduced. It states that if $f(x)$ and $g(x)$ are two integrable functions with the respective Fourier transforms $F(k)$ and $G(k)$, then the Fourier transform of the convolution of these functions is given by the product of their respective Fourier transforms: $F(k) \cdot G(k)$. For two slits with a width of a and a distance between the slits of A, the aperture function can be written as:

$$f(x) = s(x) * (\delta(x + A/2) + \delta(x - A/2)) \tag{2.32}$$

Here, $s(x)$ denotes the aperture function of a single slit (see Equation 2.27) and the second term is the aperture function for two very narrow slits

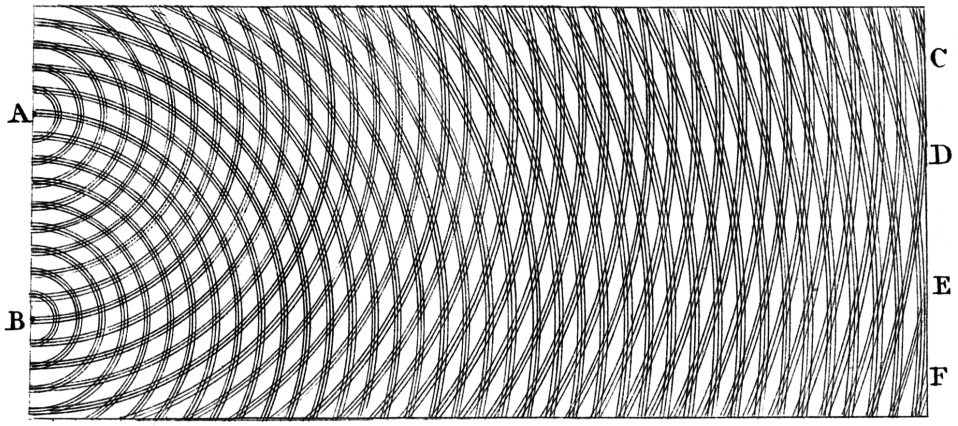

Figure 2.8: Scan of Thomas Young's original sketch of the double slit experiment. Spherical waves that originate in A and B interfere in various phases at the points C, D, E and F. The image copyright is in the public domain.

(represented by two delta functions) which have a distance A from each other. The Fourier transform is then given by:

$$F(k) = a\,\frac{\sin(\pi\,a\,k)}{\pi\,k}\,\left(e^{-\pi\,i\,A\,k} + e^{\pi\,i\,A\,k}\right) = 2a\,\frac{\sin(\pi\,a\,k)}{\pi\,k}\,\cos\left(\pi\,A\,k\right) \quad (2.33)$$

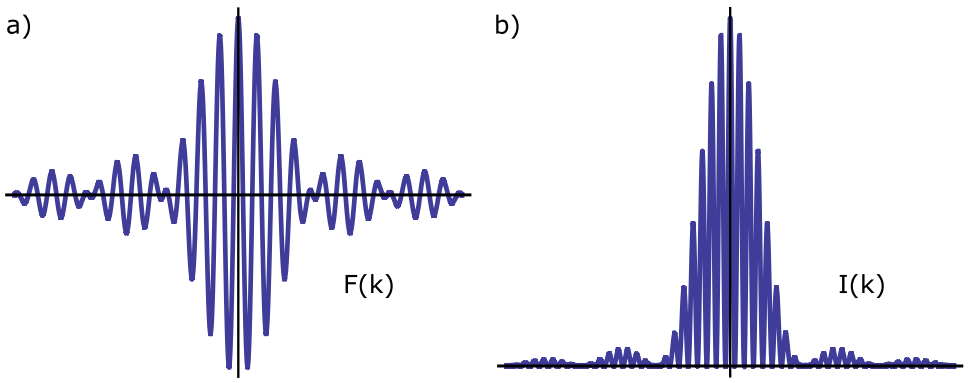

Figure 2.9: a) Normalized distribution of the electrical field under Fraunhofer diffraction on a double slit (with $A = 8 * a$). b) Normalized intensity distribution under Fraunhofer diffraction on the same double slit.

Diffraction on a Two-Dimensional Periodic Grid

Analogous to the double slit convolution, the aperture function of a 2D periodic grid of circular apertures can be calculated from the convolution of a single circular aperture $s(x,y)$ as given by Equation 2.30 and a 2D grid of delta-functions.

$$f(x,y) = s(x,y) * P^2 \sum_{n=0}^{N-1} \delta(x - nP) \sum_{m=0}^{M-1} \delta(y - mP) \quad (2.34)$$

Here, the number of periodically spaced apertures in the x-direction is N, and in y-direction, there are M apertures. The periodic distance in both directions is P. Utilizing linearity, translation and other relationships of the Fourier transform as provided in the book by Cowley [43], the Fourier transform of the grid can be calculated. A full derivation has been provided elsewhere [69].

$$\begin{aligned} F(k_x, k_y) &= P^2 S_e(k_x, k_y) \sum_{n=0}^{N-1} (e^{-ik_x P})^n \sum_{m=0}^{M-1} (e^{-ik_y P})^m \\ &= P^2 S_e(k_x, k_y) \frac{e^{.ik_x PN} - 1}{e^{-ik_x P} - 1} \cdot \frac{e^{.ik_y PM} - 1}{e^{-ik_y P} - 1} \end{aligned} \tag{2.35}$$

Here, $S_e(k_x, k_y)$ is the Fourier transform of a single circular aperture as given by Equation 2.31. With $I(k_x, k_y) = F(k_x, k_y) \cdot F^*(k_x, k_y)$, the intensity distribution follows.

$$I(k_x, k_y) = P^4 S_e^2(k_x, k_y) \left(\frac{\sin(N\frac{k_x P}{2})}{\sin(\frac{k_x P}{2})} \right)^2 \cdot \left(\frac{\sin(M\frac{k_y P}{2})}{\sin(\frac{k_y P}{2})} \right)^2 \tag{2.36}$$

It should be noted that in a diffraction experiment, usually only the intensity distribution after an aperture can be recorded. The field amplitude can typically not be measured, which leads to a loss of the phase information. However, the position of the diffraction maxima and minima, as well as grid-perturbation-induced intensity changes can be assessed by measuring the intensity distribution.

3

MATERIALS AND METHODS

In this chapter, the general experimental methods that are utilized throughout the following chapters of this work are introduced from a technical and methodological perspective.

3.1 NANOSTRUCTURE FABRICATION

For the image-based-detection in Part ii, transparent pre-cut ($(5 * 5)\, mm^2$) fused silica samples (SiO_2) are utilized as substrates. For the diffraction-based-detection in Part iii, non-transparent silicon samples (Si) of the same size are used. To remove dust particles from the samples, they are cleaned with dimethyl sulfoxide (DMSO) in an ultrasound bath. Afterward, polymethyl methacrylate (PMMA), a positive resist, is spin-coated onto the substrate. In a high-vacuum chamber, a $3\, nm$ thick layer of chromium (Cr) is evaporated onto the sample for the SiO_2 substrates to reduce surface charging during electron-beam lithography. Using an eLine plus (Raith), the desired circular structures (with a radius of $225\, nm$ or $375\, nm$ and a periodicity of $1.2\, \mu m$ or $2.0\, \mu m$) are inscribed on the sample. Nanostructure lattices of various sizes ($(40 * 40)\, \mu m^2 - (800 * 800)\, \mu m^2$) are produced. For the SiO_2 substrates, the chromium layer is then removed by wet chemical etching, and the resist is developed and removed from the areas that were previously illuminated by the electron beam. This removal is performed using a solvent. A $3\, nm$ thick layer of titanium (Ti) is then evaporated onto the sample as an adhesion promoter, followed by a $60\, nm$ thick layer of gold (Au). The remaining resist is then lifted off in DMSO, leaving behind the gold nanostructure lattice. This process is summarized in Figure 3.1. Figure 3.2 shows section of a scanning electron micrograph of a finished Si sample.

3.2 CELL-CULTURE

The experiments in this work are performed with four different human cell lines: The adenocarcinomic alveolar basal cell line A549 [70], the hepatocyte-derived carcinoma cell line HuH7 [71], the human-breast-adenocarcinoma cell line MDA-MB-231 [72], and a primary human melanoma cell line. The cells are grown in a standardized cell culture procedure and incubated at 37° Celsius and 5 % CO_2. A549 cells are cultured in growth medium consisting of Minimum Essential Medium supplemented with 10 % fetal bovine serum and $2,5\, mM$ L-Glutamine. Cells are grown in a culture flask up to $65 - 85$ % confluency. Every 2-3 days this confluency is reached, and they are washed in a PBS buffer solution and trypsinized for 3 minutes at 37° Celsius. Afterward, the trypsin is removed by refilling the flask with

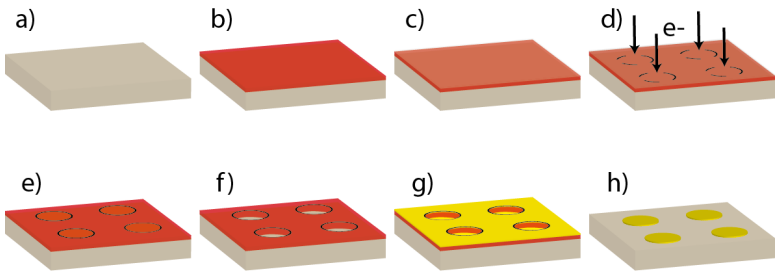

Figure 3.1: Sample fabrication steps: a) *Si* or SiO_2 substrate, b) PMMA spin-coating, c) *Cr* evaporation (for SiO_2 substrates only), d) electron beam exposure, e) *Cr* etching (for SiO_2 substrates only), f) PMMA developing, g) *Ti* and *Au* evaporation, h) final sample after the liftoff. Reprinted with permission from Nano Letters, 2017, 17 (12), pp 8018–8023. Copyright 2017 American Chemical Society.

medium and then centrifuging the mixture for 3 minutes at 1000 rounds per minute. The trypsin and medium are withdrawn, and the cells are resuspended in the desired splitting ratio (1/3 ratio, to reach the same confluency level again in two days). This procedure is the same for HuH7 (MDA-MB-231, primary) cells, with the exception that the utilized culture medium is Dulbecco's modified Eagle's medium (L-15 medium without the 5 % CO_2 atmosphere, RPMI medium) with the same supplements. For the experiments that utilize the microscopy setup (3.3), the cells are resuspended and seeded on the prepared nano-structured sample slide in the desired confluency. Since the microscope is working under atmospheric air composition in contrast to the 5 % CO_2 in the incubator, the culture medium is changed to Leibovitz L-15 medium that is supplemented as before for resuspension. For the diffraction experiments, the medium is the same as the growth medium, as these experiments are performed in an incubator with 5 % CO_2. In both cases, 1 % penicillin/streptomycin is added to the medium to avoid bacterial infections. Experiments are either performed with the cells adhered to standard cell dishes made of plastics or SiO_2 or with the cells adhered directly to the nano-structured substrate made of SiO_2 or *Si*, another biocompatible material [73]. Biocompatibility tests of the structured substrates compared to standard cell dishes reveal no changes in cell adhesion, migration or proliferation.

3.3 MICROSCOPY SETUP AND IMAGE ANALYSIS

Distortion Detection

To quantify distortions in Part ii, high resolution microscopy is utilized. A Ti-E Eclipse inverted microscope (Nikon Instruments), employed for bright-field and epi-illumination, is equipped with a $100x$ oil immersion objective ($NA = 1.4$) that, in epi-illumination, also functions as a condenser with

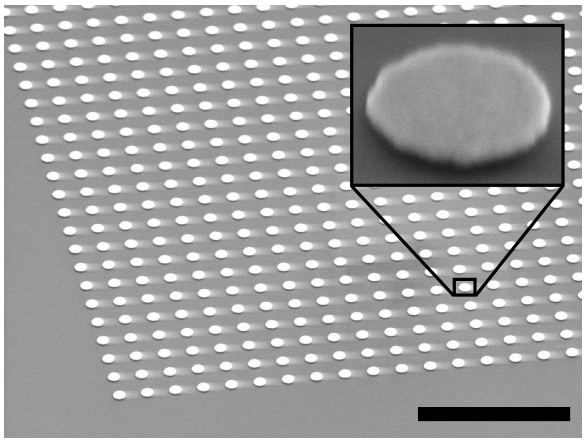

Figure 3.2: Scanning electron microscopy image of a Si substrate patterned with a grid of Au structures. The structures have a diameter of 750 nm and the grid periodicity is 2 μm. The scale bar is 10 μm.

matching NA. The epi-illumination setup is modified from a fluorescence setup by removing the excitation filter to permit reflection measurements. A SOLA lamp (Lumencore) and an optical filter with a bandpass wavelength centered at 628 nm and a bandwidth of 40 nm is used. The images are acquired with a Clara-E CCD camera (Andor). Samples growing in a Petri dish (ibidi) are mounted upside down on the inverted microscope, hence imaging the gold structures through the cell. With this experimental setup, the images of several thousand gold nanostructures in the field of view (66 $\mu m * 89\,\mu m$) and up to several hundred structures per cell are recorded and serve as reference points for the localization. The microscope is equipped with a heating chamber, which keeps the whole setup on a constant temperature of 37° Celsius. This ensures that cell survival is only limited by the amount of nutrients in the medium and that measurements can be performed over several days. Furthermore, thermal drifts imaged sample over time are minimized. For the optical measurement in Part iii of this work, a specialized microscope of the same type (Ti-E Eclipse) is utilized. It has the same operating composition but slightly different components. The microscope is equipped with a second set of objectives on top of the sample-holder in addition to inverted detection arm. Therefore, the cell-induced distortions can additionally be measured without having to image through the bottom of the Petri dish with a CFI Plan Achro 100x water dipping objective ($NA = 1.1$). This procedure omits to have to mount the sample upside down. The setup employs Zyla 5.5 sCMOS cameras (Andor) in both optical arms, which have a four-times bigger sensor and thereby also a four-times greater field of view.

Image Analysis and Localization Accuracy

To precisely localize the gold structures, rapidSTORM [74] is used to fit a 2D normal distribution to every single nanostructure automatically. It records the center of the fit with sub-pixel accuracy (see Figure 3.4 a)).

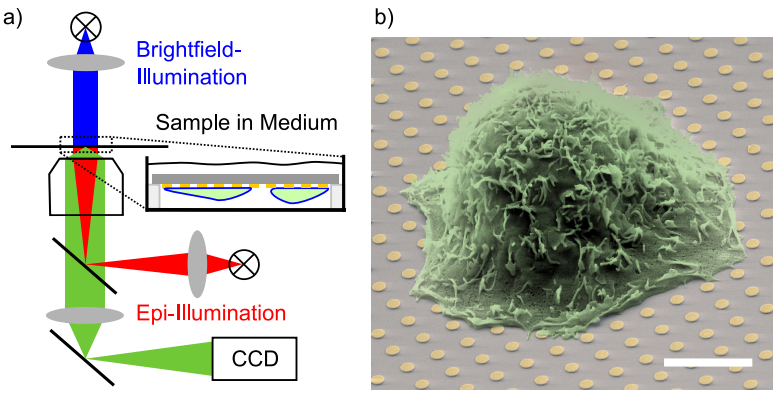

Figure 3.3: a) Schematic diagram of the experimental set-up. Bright-field illumination (blue) is used for cell imaging, while epi-illumination (red) is essential for nanostructure localization. b) Colored scanning electron micrograph of an A549 cell (green) on a surface periodically patterned with gold nanostructures (yellow). Scale bar: 5 μm. Reprinted (modified) with permission from Nano Letters, 2017, 17 (12), pp 8018–8023. Copyright 2017 American Chemical Society.

Through this procedure, a centroid-localization-precision that is comparable to super-resolution microscopy [13] is achieved. The optical displacement vector is determined by calculating the difference between the original (un-distorted) and the optically displaced image position of each structure in Mathematica (see Figure 3.4 b)). The original position can be obtained from a calculated or an experimental reference framework without any cell. The calculated reference framework is computed, based on the periodicity of the fabricated lattice. For the experimental reference framework, the same gold-structures are imaged in the absence of cells to yield the unbiased positions of the gold structures. The accuracy of both methods is assessed by measuring the distortion field in a cell-free image, to find the more precise method. Since no cell-induced distortion is expected in such an image, any measured distortions can be attributed to characteristic precision-dependent measurement errors inherent to the method. For the experimental reference frame, an image of the gold lattice without any cells is taken. The sample is then removed from the microscope stage and remounted to simulate the procedure performed in the measurements with cells (where the cells have to be seeded onto the substrate after the reference images have been taken). A second image is then taken, and structure localization is performed in both images using rapidSTORM. Then the two lattices of structure localizations are fitted onto each other in Mathematica, using only translation and rotation of the whole lattice as free parameters. The resulting distortions of all the structures in the image and hence the methodological errors are shown in a histogram plot in Figure 3.5 a). A mean distortion of 1.1 nm is measured. For the calculated reference framework, a periodic lattice of gold structure localizations with the same number of rows and columns of structures as observed in the image is generated. This lattice of structure localizations is fitted to the measured lattice using the same fitting parameters as before, but with additional parameters

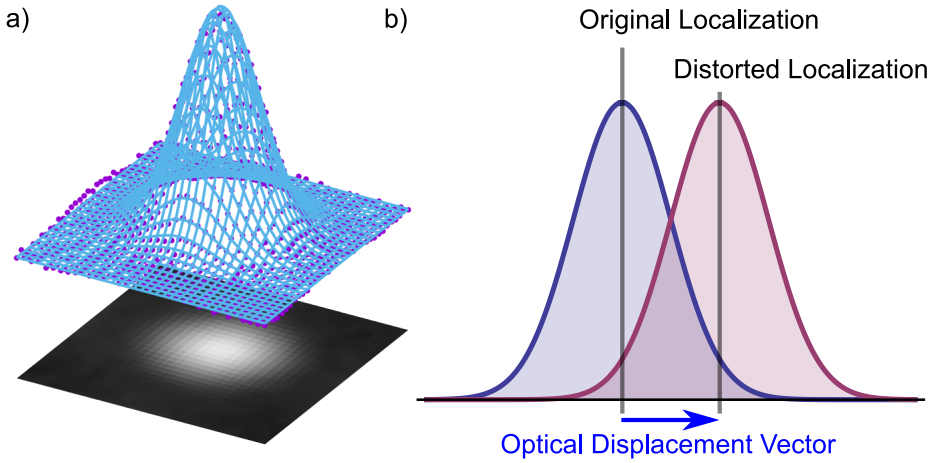

Figure 3.4: a) Schematic of fitting a 2D normal distribution (light blue) to the intensity distribution for every pixel (purple) of an image of a single nanostructure, to enhance localization accuracy. b) The optical displacement vector for each structure is defined as the vector pointing from the original (undistorted) position (center of the fit) to the optically displaced position.

for tip, tilt and stretch in x- and y-direction. Even with the additional free parameters, this procedure yields a calculated mean distortion of 11.0 nm for the same lattice assessed with the experimental reference (see Figure 3.5 b)). This larger mean distortion is mainly attributable to the precision (typically about 10 nm) attainable with e-beam lithography [75]. Because of the ten-fold smaller localization error, the experimental reference frame is used for all experiments. Thus, before each cell measurement, the sample is imaged without cells in order to obtain this experimental reference. It should be noted that the accuracy achieved with the experimental reference is dependent on the precise focus in both the reference frame and the cell frame since even a small defocus or vibrations of the microscope in one of the frames can decrease the accuracy. Also, additional distortions can occur due to small differences in the volume or the composition of the cell medium between the two measurements.

Confocal Microscopy

In Chapter 5, the cell shape is reconstructed from the data acquired in the distortion measurement and compared to the actual 3D cell shape. The 3D cell shape is therefore measured independently with a confocal fluorescence microscope by labeling the cell membrane with the Cell Mask Orange plasma membrane stain (Invitrogen) prior to the measurement of the optical distortion field. The confocal measurement is performed using a spinning-disk unit (Yokogawa) and an EMCCD Camera on an inverted microscope with a Plan-Apochromat 63x Oil objective (Zeiss, $NA = 1.46$). To minimize the change in the shape of the living cell over time, the confocal measurement and the distortion measurement are performed within

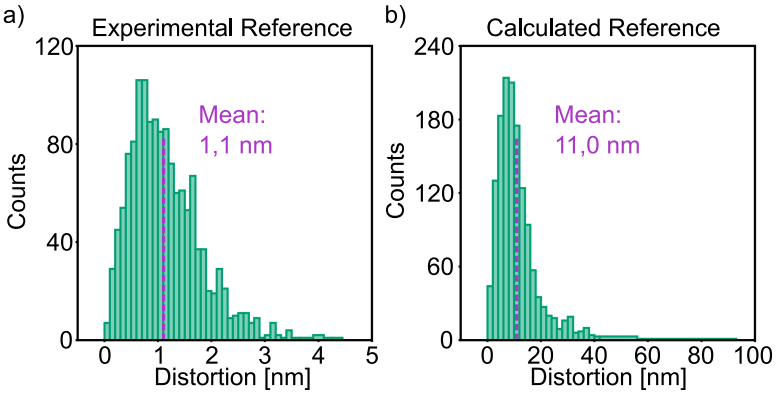

Figure 3.5: Comparison of accuracies achieved by experimental and calculated reference frameworks. a) Histogram of the distribution of structural distortions in a frame without a cell, derived from an experimental reference frame. b) Histogram for the same frame as in a), this time derived from a calculated reference framework. Reprinted with permission from Nano Letters, 2017, 17 (12), pp 8018–8023. Copyright 2017 American Chemical Society.

10 minutes of each other. Images with a vertical spacing of 100 nm are recorded. The images are subsequently thresholded and a bivariate polynomial in x and y, consisting of all terms up to degree twelve, is fitted to the thresholded data to compute the cell shape.

3.4 DIFFRACTION MEASUREMENT

Setup

Within this thesis, a diffraction setup to measure drug responses of cell ensembles in high throughput has been devised and build up. The main components of the setup are a laser diode, a diffraction grating, and a CMOS sensor. The utilized laser diode is a 5 mW ultra-low noise diode laser (Coherent) with a wavelength of $\lambda = 635\,nm$, which provides a coherent light source with very low noise. As a diffraction grating, a nano-structured gold lattice on a Si substrate with a lattice size of $((800 * 800)\,\mu m^2)$ and a structure periodicity of $2.0\,\mu m$ is used (see Section 3.1). The laser light gets diffracted on the diffraction grating, and the resulting diffraction pattern can be analyzed. This analysis is done with a UI-1541LE-M monochromatic CMOS sensor (IDS). It records the shape and intensity of a single diffraction peak over time. The CMOS sensor has an image area of $6.66\,mm * 5,33\,mm$ and a large $5.2\mu m$ pixel size, which ensures a high signal-to-noise ratio. To measure cell-ensemble responses, the cells are seeded in a 6-channel μ-slide (6-channel 0.4 ibiTreat, ibidi), which is placed directly above the diffraction grating. As the cells have a refractive index that differs from the one of the surrounding medium, they change the phase of the laser light that passes through them. Hence, they change the interference condition for the diffraction at the diffraction grating, which in turn

changes the shape and intensity of the diffraction peak. To assess multiple positions within one channel and to perform high-throughput experiments with multiple channels and up to four 6-channel slides at the same time, the slides are placed on a motorized, high-precision x-,y-,z-scanning stage H101P1F (Prior Scientific). The stage can be programmed to automatically measure and loop various samples at defined times (see below). The whole setup is placed on a damped optical plate to guarantee high mechanical stability and reduce noise from external vibrations. To enable a diffraction detection with the cells under typical culture conditions, the diffraction setup is built inside a cell culture incubator. An INCOmed 246 incubator (Memmert) is used. It provides standard cell culture conditions (5 % CO_2, 37° Celsius, 95% humidity) during the experiment and high thermal stability of the setup. An additional imaging setup is implemented into the setup, to survey optical information of the measured cell ensemble like cell confluency, cell proliferation over time, cell adherence and cell clustering during the experiment. Since microscopy setups are bulky, expensive and difficult to operate in an incubator automatically, a holographic imaging setup consisting of only a Kingbright L-9294SECK LED (Kingbright Electronic Co.) with a wavelength of $\lambda = 610\,nm$ and a OV5640 CMOS sensor (OmniVision) is employed. The sensor is mounted next to the diffraction grating, and the motorized scanning stage can move the sample to the area of interest in between the diffraction measurement. The CMOS sensor is then illuminated by the low coherent light from the LED (placed above the sensor) and records the holographic image (diffraction pattern) of the cells. Such an imaging configuration is described in detail in [76] and provides low-resolution images but a large field of view (image area: $3670\,\mu m * 2735\,\mu m$) of the cell ensemble. The complete setup is stylized and pictured in Figure 3.6. For a simultaneous measurement of a) the cell shapes of cells in a small ensemble on top of a diffraction grid and b) the change in diffraction peak intensity that these cells induce over time, the diffraction setup is furthermore build up within a high-resolution microscopy setup that is presented in Section 3.3.

For the diffraction measurement, the $(2|0)$-diffraction peak is recorded. This peak has been chosen since it is diffracted from the grid under an angle (see Equation 6.8) that is easily detectable. The same is true for the $(1|0)$-diffraction peak, but it is found experimentally that the higher diffraction order peak provides a better signal-to-noise ratio in the intensity signal. To analyze the diffraction peak in the far field, the Fraunhofer condition (see Section 2.3) has to be met. One rough criterion to define the near and far field approximations is established by the Fresnel number F as defined by:

$$F = \frac{a^2}{L * \lambda} \tag{3.1}$$

Here, L is the distance between the diffracting aperture and the screen, λ is the wavelength and a is a characteristic size of the aperture. For $F \gg 1$ one is in the regime of geometrical optics, for $F \approx 1$ the Fresnel approxima-

tion holds true and for $F \ll 1$ the Fraunhofer condition is met. Therefore, the utilized illumination wavelength of $\lambda = 635\,nm$ and the aperture size $a = 400\,\mu m$ [1] define a minimum distance between the diffraction grid and the CMOS sensor in order to detect the diffraction peak in the Fraunhofer regime. For this, a Fresnel number smaller than 0.5 defined as the Fraunhofer regime [77] This yields:

$$L \geq \frac{400 * 10^{-6}m * 400 * 10^{-6}m}{0.5 * 635 * 10^{-9}m} = 0.504\,m \tag{3.2}$$

The detector has to be set up at a distance of at least $50cm$ from the grating. Therefore two optical mirrors are utilized in the setup to facilitate an optical distance of about $60cm$ within the incubator. This configuration guarantees a distinct main peak and distinctly separated side peaks on the detector.

Signal Read Out and Software

Julian Aschauer [78] developed the measurement program utilized in the diffraction setup in *c++* on the basis of the *UEyeDemo* program provided with the IDS CMOS sensor. The program provides a graphic user interface to design experiments, which are then automatically run by the program. For this, the program directly communicates with the motorized stage, the CMOS sensor for the diffraction detection and the LED and sensor of the holographic imaging setup. The sample and mirrors are manually adjusted so that the diffraction peak is imaged in the center of the CMOS sensor. Then the peak intensity is maximized by fine adjusting the center of the laser to the center of the diffraction grid. The program now tracks the peak maximum over time by fitting an ellipse area onto the detected intensity profile. The major and minor semi-axis of the ellipse are calculated by fitting normal distributions to the peak intensity in these semi-axes and setting the respective semi-axis diameter to four standard deviations of the fitted normal distribution. The peak intensity is calculated by summation over all pixel intensities within the fitted ellipse and recorded with a frame rate of 5 frames per second. The diffraction peak in each channel is analyzed for a particular time (typically one minute), then an image of the sample area is optionally taken with the holographic imaging setup, and the next channel is analyzed. For each distinct channel measurement, the center of the ellipse fit and the ellipse fitting parameters are saved in a log file, and a single image of the peak distribution is recorded for easily accessible drift detection. In addition to the peak intensity, the standard deviation of the peak intensity over the last 50 frames and the time of recording are saved for every frame in a data file for further analysis. A more detailed description of the functionality of the program, the working principle of the tracking algorithm as well as a software manual can be found in [78].

1 Here, a is defined as half the structure size in accordance with utilizing the radius for circular apertures, and the use of the half-angle in the definition of the numerical aperture.

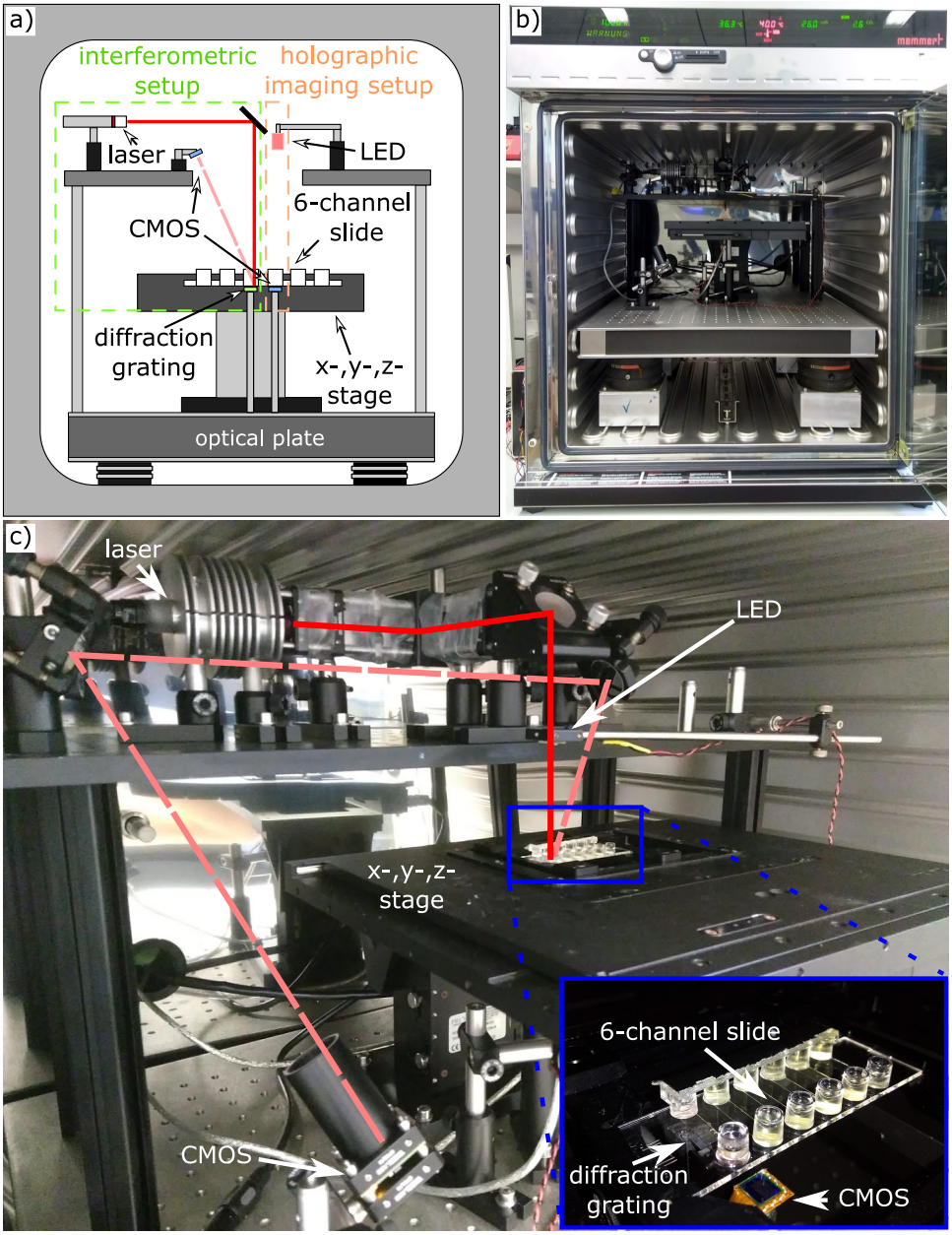

Figure 3.6: a) 2D schematic of the diffraction setup: the setup is built on an optical plate inside a CO_2-incubator to provide stable measurement conditions. The cells are seeded in 6-channel slides on a motorized, high-precision x-,y-,z-stage to allow for high throughput measurements. An ultra-low noise diode laser provides the coherent light source that illuminates the diffraction grating below the cell-sample. A CMOS sensor is utilized to record the intensity and the profile of a resulting diffraction peak. An LED and an additional CMOS sensor underneath the sample form an additional functional unit that provides holographic images of the cell-sample, which are used as an optical control. b) Image of the CO_2-incubator that houses the diffraction setup. The incubator provides standard conditions (5 % CO_2, 37° Celsius, high humidity) for the experiment. c) Image of the diffraction setup. The laser light path is stylized by the red line. The diffraction peak is reflected toward the CMOS sensor via two optical mirrors (dashed, light-red line), which guarantees that the recorded diffraction pattern is within the Fraunhofer regime. The subsequent channels of the 6-channel slide are scanned in by driving the stage in the x-direction, while the sample is placed on top of the CMOS sensor when driving the stage in the y-direction.

3.5 HYDROGEL FABRICATION

To encapsulate cells in a hydrogel, a pre-polymer solution containing cells is produced, which is then polymerized inside a culture dish by light-illumination. A detailed protocol can be found in Dietrich et al. [79]. The pre-polymer solution is prepared in PBS buffer with 20 kDa 4-armed polyethylene glycol norbornene (PEG-NB, JenKem Technology), dithiol-containing, MMP-degradable cross-linking peptide (KCGPQGIWGQCK, Iris Biotech), CRGDS-peptide (RGD, Iris Biotech) and the photo-initiator lithium phenyl-2,4,6-trimethylbenzoylphosphinate (LAP, custom synthesized, see also [80]). Cells are suspended in PBS and added to the pre-polymer solution. The amount of each substance used can be found in Table 3.1. After the addition of the suspended cells, the pre-polymer solution is pipetted into a channel of a 6-channel μ-slide (6-channel 0.4 ibiTreat, ibidi) and the hydrogel is polymerized by illumination with collimated UV light ($\lambda = 365\,nm$) through a custom-made chrome mask at $10\,mW/cm^2$ for 30 seconds. The remaining pre-polymer solution is washed out with PBS, and the hydrogel is incubated in culture medium under standard conditions for at least two hours before the start of the experiment to allow the hydrogel to swell to a steady state. The process yields one hydrogel structure per illuminated channel with a structure width of $1\,mm$, a length of $2\,mm$ and a height of $400\,\mu m$ (limited by the channel height). Figure 3.7 shows two images of a polymerized hydrogel in a channel of a 6-channel slide, one without cells (a) and one with a low cell density (b).

Substance	Substance Concentration	Volume
PEG-NB	20 mM	$6.75\,\mu l$
RGD	20 mM	$2.25\,\mu l$
KCGPQGIWGQCK	40 mM	$4.05\,\mu l$
LAP	20 mM	$6.75\,\mu l$
PBS		$10.20\,\mu l$
Cells in PBS	$1 - 1.5 \cdot 10^6 cells/ml$	$15.00\,\mu l$
Sum		$45.00\,\mu l$

Table 3.1: Composition of the pre-polymere solution for the hydrogel fabrication.

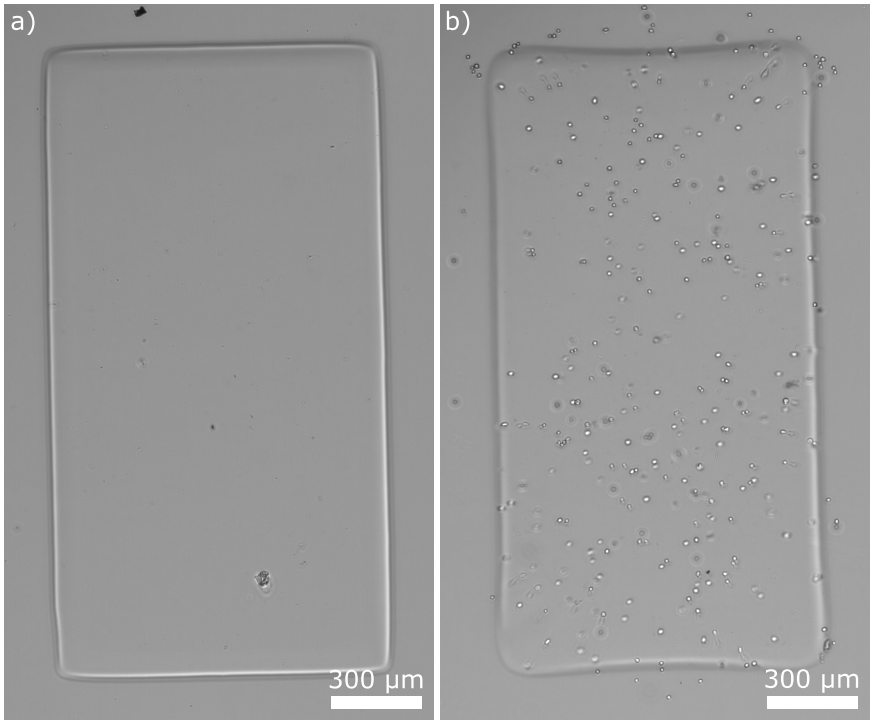

Figure 3.7: Images of a polymerized hydrogel in a channel of a 6-channel slide without cells (a) and with a low cell density (b).

Part II

RESULTS - IMAGE-BASED DETECTION

The results presented in this part are summarized in the publication:
"Single-Cell Optical Distortion Correction and Label-Free 3D Cell Shape Reconstruction on Lattices of Nanostructures"
by Stephan, Jürgen and Keber, Felix and Stierle, Valentin and Rädler, Joachim O. and Paulitschke, Philipp. [81]

4

QUANTIFICATION AND CORRECTION OF SINGLE-CELL-INDUCED DISTORTIONS

4.1 SPECIMEN-INDUCED DISTORTIONS IN MICROSCOPY

On the one hand, adaptive optics is a heavily studied field in biological imaging and has helped to improve image contrast and resolution in thick tissue imaging (see Section 2.2). On the other hand, specimen-induced distortions have not received a substantial amount of attention in biological imaging. In 2002, James Pawley qualitatively showed that refractive index variations in thin cell sheets significantly distorted the imaged in live-cell confocal microscopy [82]. He thereby challenged the prevailing notion that the nearly constant refractive index within a cell and thus within a thin tissue does not induce significant image distortions.
A quantitative measure of specimen-induced distortion in light microscopy was then provided in 2007 by Schwertner et al. [64]. By interferometrically measuring wavefront distortions and subsequent Zernike polynomial analysis, they were able to show that biological specimen of only $20\,\mu m$ thickness can cause image distortions of up to several hundred nanometers in x-, y- and z-direction. They furthermore showed that even by utilizing wavefront sensors in confocal and two-photon microscopes, image distortions cannot be fully corrected when operating these microscopes in the standard epi-configuration [83], which is characterized by imaging and illuminating with the same objective. For very thin specimen or single cells the effect of specimen-induced distortions has previously been considered to be small [64], but for imaging techniques that measure spatial distances in or through such specimen, even small distortions in the order of a $10 - 50\,nm$ can significantly impair the accuracy of the measurement.
One such technique is traction-force-microscopy [84–89]. In this technique, cells are placed on a flexible substrate, which is either a gel with fluorescent beads or a grid of flexible pillars or nanowires. Cell forces are calculated by measuring the mechanical displacement of the beads, pillars or nanowires. This calculation can be done by knowing the spring-constant of the pillars and nanowires or the stiffness of the gel. The technique allows quantifying cell forces with a precision down to the piconewton regime by employing high-resolution localization microscopy. For thicker transparent [90, 91] or non-transparent samples [92–95], imaging through the cell is typically unavoidable. In these cases, the accuracy of force calculation may be impaired, since the optical distortions in the measurement can superimpose the mechanical displacements.
In fluorescence localization microscopy and single-particle tracking [15, 96–98] the imaging is also often done through or into living cells, and localization accuracies in the nanometer range are required. These accuracies can

again be limited by optical refraction at the specimen, and consequently, an optical correction might be of need [99]. To asses the magnitude of distortion in traction-force- and localization-microscopy and thus determine whether or not a distortion correction is needed, a quantitative measurement of single-cell-induced distortions is required. However, until now optical distortions induced by single cells have not been investigated.

4.2 OPTICAL QUANTIFICATION ON NANO-STRUCTURED GRID

Quantification Method

As distortions are not directly visible in an image, they cannot be quantified by only imaging the specimen. One empirical approach to quantify distortions is the utilization of a calibration specimen as a reference framework [100, 101]. Such a calibration specimen is characterized by a repetitive pattern or lattice with known spatial distances [102]. The distortion field (i.e., the spatially resolved distribution of optical distortions) in an image can then be quantified by the difference between the actual and the measured distances between characteristic points of the calibration specimen. Since here the distortions induced by single cells are of interest, and hence the cells inducing the distortions and the calibration specimen have to be imaged at the same time, the substrate on which the cells are seeded is periodically patterned with gold nanostructures to act as the desired calibration specimen.
To this end, a precise lattice of periodically patterned gold nanostructures is lithographed onto the substrate as described in the fabrication process (see Section 3.1). To quantify the optical distortions induced by living single cells growing on such a substrate, typical adherent cell lines are chosen, and these cells are cultured and seeded as described in Section 3.2. With the help of a high-resolution localization microscopy set-up, which is introduced in Section 3.3, the local cell-induced distortion can be quantified with reference to the fixed underlying lattice.
Figure 4.1a) shows a bright-field image of a typical adherent A549 cell. This image allows for localization of the cell but is not suited for a comprehensive localization of the gold structures due to the similarity in gray-scale intensities between the cell and the structures. This becomes particularly obvious in the close-up and the plotted intensity profile (e.g., at $5 - 10\,\mu m$) in Figure 4a). However, the gold structures can be localized either by fluorescence labeling or by measuring in reflection mode (epi-illumination), which permits clear differentiation between the gray-scale intensities associated with intracellular structures and the underlying nanostructures. In this work, the reflection measurement is chosen (see Figure 3.3a)), since no additional labeling is needed and the bleaching of fluorophores (which would otherwise limit the observation time) is avoided. The localization is done by fitting a 2D normal distribution to every single nanostructure, as described in Section 3.3. This procedure allows achieving a centroid local-

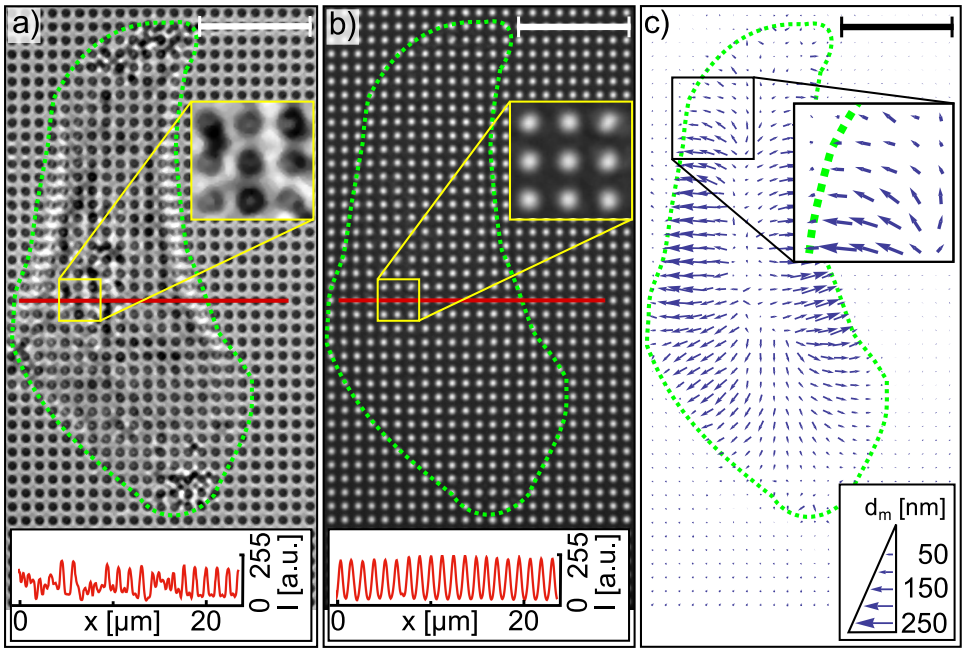

Figure 4.1: a) Bright-field image of a single adherent A549 cell on a nano-structured substrate. The cell outline is highlighted in green. The lower inset shows the intensity profile of the cross-section corresponding to the red line, while the upper inset shows a close-up. b) Reflection image of the same sample as in a). c) Vector plot of the distortion field. The vectors point from the original to the displaced positions of the gold nanostructures in the images. The upper inset shows a two-fold enlargement. The bottom inset shows the scaling vectors. Scale bars: 10 μm. Reprinted with permission from Nano Letters, 2017, 17 (12), pp 8018–8023. Copyright 2017 American Chemical Society.

ization precision comparable to super-resolution microscopy [13].
A typical reflection image is shown in Figure 4.1b), where localization of the gold structures is achieved even inside the area occupied by the cell (highlighted in the close-up and the intensity profile). With the help of a reference frame of the undistorted structures, the local cell-induced distortions can be quantified with an ultra-high accuracy down to 1.1 nm (see Section 3.3). Figure 4.1c) shows a vector plot of the distortion field induced by the single cell. For better visualization the optical displacement vectors are enhanced in comparison to the spatial distance in the image. The apparent distinction between the vector sizes in the areas with and without the cell highlights the high signal to noise ratio of the method.

Distortion Magnitude

For the depicted cell, absolute values of the measured optical displacement vectors $\vec{d_m}$ range from a few nm to a maximum distortion of 240 nm, with an average of the absolute values of the distortions of 85 nm inside the area covered by the cell. Table 4.1 summarizes the mean and maximum distor-

Cell	Mean Distortion	Max. Distortion	Datapoints	rdError
1	85 nm	240 nm	456	13 %
2	50 nm	150 nm	149	8 %
3	79 nm	172 nm	65	8 %
4	126 nm	227 nm	90	6 %
5	60 nm	144 nm	93	4 %
6	103 nm	187 nm	69	9 %
7	111 nm	362 nm	76	13 %
8	101 nm	493 nm	110	17 %
9	75 nm	192 nm	92	8 %
10	142 nm	315 nm	143	10 %
Average	93 nm	248 nm		10 %

Table 4.1: Mean- and maximum-vaules for distortions induced by 10 different measured A549 cells. Additionally the number of data points per cell and the maximum of the relative distortion-induced distance error (rdError) is obtained.

tions measured for a total of 10 different A549 cells. (Note that cell 1 is the depicted cell, and cells 2-10 have been measured with 2.0 μm grids.) On average these cells distort the image by about 90 nm with a total maximum distortion of about 490 nm being measured. Additional time-lapse measurements of the distortion fields induced by Huh7 cells show similar optical displacements of up to 400 nm (see Section 5.2).

The distortion measurement should be independent of the mode of illumination (trans- or epi-illumination) as the distortions occur due to a change of the imaging light path after the gold structures, which is the same in brightfield-, reflection-, and fluorescence-measurements. To illustrate this, one can look at the optical effects of the cell and how they would alter the image.
In the experimental distortion measurement, the light travels through the cell twice. Once in the illumination path entering the cell and once in the scattered light path from the gold structures leaving the cell again. The illumination light path is responsible for the homogeneous illumination of the sample. The only effect that would lead to distortions in the image caused by this path is inhomogeneous illumination. Refraction and absorption at the cell can alter the local illumination at the gold structure plane and therefore lead to inhomogeneous illumination. This, in turn, could lead to a distorted center of the structures when imaging them. However, no significant inhomogeneities are observed.
This can be seen in Figure 4.1 b) and the corresponding inset, where the gold structure intensity profiles (inset) in the cell area and the non-cell area are not significantly different from each other. Therefore, it can be

assumed that inhomogeneous illumination and cell-induced effects due to distortions on the illumination path are negligible. Hence, the cell-induced change to the light path after the reflection is decisive for the distortions that occur in the imaging of the gold structures. The light originating from each structure is collected by the objective and forms the image, in general regardless of the illumination light path. Thus, only the displacement of the light path between the sample and the image causes the optical distortion of the structure in the image. The order of magnitude of the measured distortions is further validated by ray tracing simulations of a model cell in the microscope system, which show comparable image distortions (see Section 4.4).

Implications for Localization Microscopy

To put these results into perspective, the distortions (optical displacements) are compared to the observed pillar and nanowire displacements in state-of-the-art traction-force microscopy set-ups that also image through single cells. Typically reported displacements range from a few 10 nm up to 1 μm [90, 92] and are thus in the same order of magnitude as the cell-induced distortions reported here. Distortions can also affect distance measurements between two different read-out points, e.g. in fluorescence localization and single-particle tracing.[15] The measured distortion fields can be utilized to assess the distortion-induced error caused in such a distance measurement. To this end, the optical displacement vector difference between two spatial points is calculated, which represents the optical error in a distance measurement between these two points. For the distortion field depicted in Figure 4.1 c), the optical errors for all points that are 1.2 μm apart from each other within one cell are computed. Here, a maximum vector difference of 0.15 μm is calculated, which is equivalent to an error of about 13 % over the measured distance. For all the measured cells a maximum error in the relative distance between two nanostructures due to cell-induced distortions of up to 17 % is observed (see Table 4.1).
To summarize, the measured optical displacements show that distortions reduce the accuracy of localization and distance determination, and cannot be considered negligible when imaging through a single cell.

4.3 QUANTIFICATION MEASUREMENT IN TRACTION FORCE MICROSCOPY

This section is based on the results published in the associated manuscript "Ultra-Flexible Nanowire Array for Label- and Distortion-Free Cellular Force Tracking" by Paulitschke, Philipp and Keber, Felix and Lebedev, Andrej and Stephan, Jürgen and Lorenz, Heribert and Hasselmann, Sebastian and Heinrich, Doris and Weig, Eva M. [103].

Here, as a proof of principle, a distortion quantification is performed in a traction force microscopy setup. To this end, cells of the slime mold *Dictyostelium discoideum* are seeded on a grid of *GaAs*-nanowires. The nanowires

have a periodicity of 2.8 μm, a length of 4.6 μm and a head diameter of 1.4 μm. This geometry yields a nanowire-spring-constant of about 165 N/m, making them completely rigid. Therefore, any detected nanowire displacement is not due to a mechanical displacement but due to optical distortion. The spacing also guarantees that the cells do not adhere in between the pillars but atop of the array as shown in Figure 4.2 a). A confocal spinning disk microscope is employed to simultaneously monitor the cells (labeled with Lim-GFP), and the reflected intensity of the nanowire heads over time in two distinct color channels. As the $GaAs$-sample and the nanowires are non-transparent the imaging is performed in a similar epi-configuration as utilized in Section 4.2.
Figure 4.2 b) depicts an overlay of the two channels with a cell in green and the nanowires in blue. The white arrows indicate displacements between the depicted frame and a reference frame without a cell. These displacements are calculated as described before. The arrows have again been enhanced in scale compared to the spatial distance, to provide visibility of the effect. Since the nanowires are completely immobile due to cell-forces, the apparent displacements are due to cell-induced distortions to the image. The time evolution of the distortions on four different nanowires (labeled 1-4) is presented in Figure 4.2 c). As the cell migrates from Nanowire 3 and Nanowire 4 towards Nanowire 2, the measured distortion changes at these positions, while it is relatively constant at Nanowire 1, which is not in contact with the cell at any time.
Similar to the results of the previous section, optical distortion of up to 150 nm are observed due to imaging through *Dictyostelium discoideum* cells in a traction force microscopy configuration. When utilizing such an optical configuration (i.e., imaging through the cells), these distortions lead to false mechanical displacement recordings and thus falsify the cell-force calculations. Thus, the prevention of a falsified detection or a correction of the optical distortions is needed.

One way to circumvent the problem of imaging through the cells is introduced in the associated manuscript [103]. Here, an improved geometrical design of the nanowire array is provided, which allows the cells to adhere between the nanowires. Thus the optical properties of the cell are separated from the cell-induced mechanical nanowire-displacements. For this, the *Dictyostelium discoideum* cells are seeded onto a sample with flexible nanowires. These nanowires have a lattice periodicity of 5.0 μm, a length of 8.8 μm and a head diameter of 0.6 μm. In this geometry, the cells adhere in between the nanowires, and by migrating on the surface, they deflect the nanowires mechanically. The mechanical displacement of the nanowires can be measured with the epi-setup utilized before, without having to image through the cells and thus without interference from overlaying optical distortions.
Figure 4.3 shows such an experiment. Here, a *Dictyostelium discoideum* cell inside a nanowire array is imaged over time. The mechanical nanowire displacement is calculated from a reference frame of undisplaced nanowires.

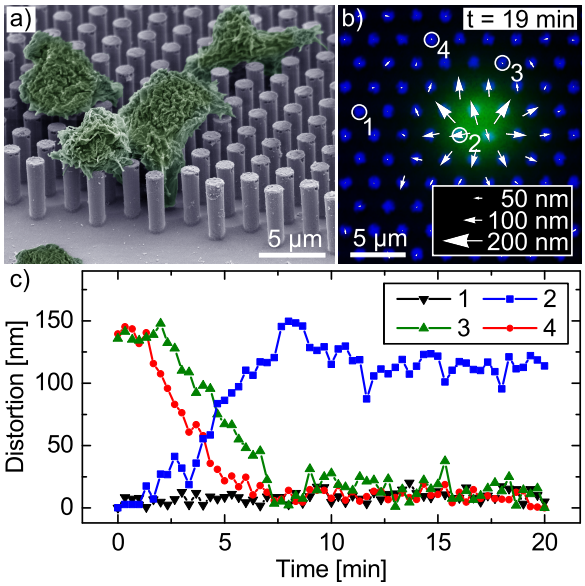

Figure 4.2: Cell-induced distortions in a traction force setup. a) Scanning electron micrograph of *Dictyostelium discoideum* cells (false color) on an array of rigid *GaAs*-nanowires. b) Fluorescence image of a cell (green) labeled with Lim-GFP on the immobile nanowire-heads (blue, reflection signal). The white arrows indicate the magnitude of the cell-induced optical distortions (scaled by a factor of 17.75 for better visualization). c) Distortion measurement over time for four distinct nanowires. Reprinted with permission from Nano Letters, Article ASAP, 2018. Copyright 2018 American Chemical Society.

While on Nanowire 1 a maximum deflection of over 3 μm due to cell forces is measured, Nanowire 2 and Nanowire 4 exhibit displacements in the same order of magnitude as the previously presented distortion measurement. These measures validate the concern of a falsified detection on relevant length scales in uncorrected traction force setups that image through the cells.
Therefore, a more general distortion correction that does not need a modified geometry of the nanowire array, is desirable. A correction that also works for force traction setups, which utilize cells on top of pillars, nanowires or gels, can provide an even greater benefit for researchers.

4.4 IMAGE CORRECTION FOR LOCALIZATION MICROSCOPY

To improve distortion-limited accuracies in quantitative localization techniques on a widely applicable basis and without posing an a priori restriction on the experiment design and sample geometry (as done in the previous chapter), an ex-post correction of the distortions in the microscope images is proposed. This correction is done by performing a pixel-wise remapping of the distorted image based on the inverted distortion vector at each pixel. The inverted distortion vector is derived by applying a simplified geometrical optics approach that allows one to link the 3D cell shape and the distortions without the need for a reference framework. The 3D

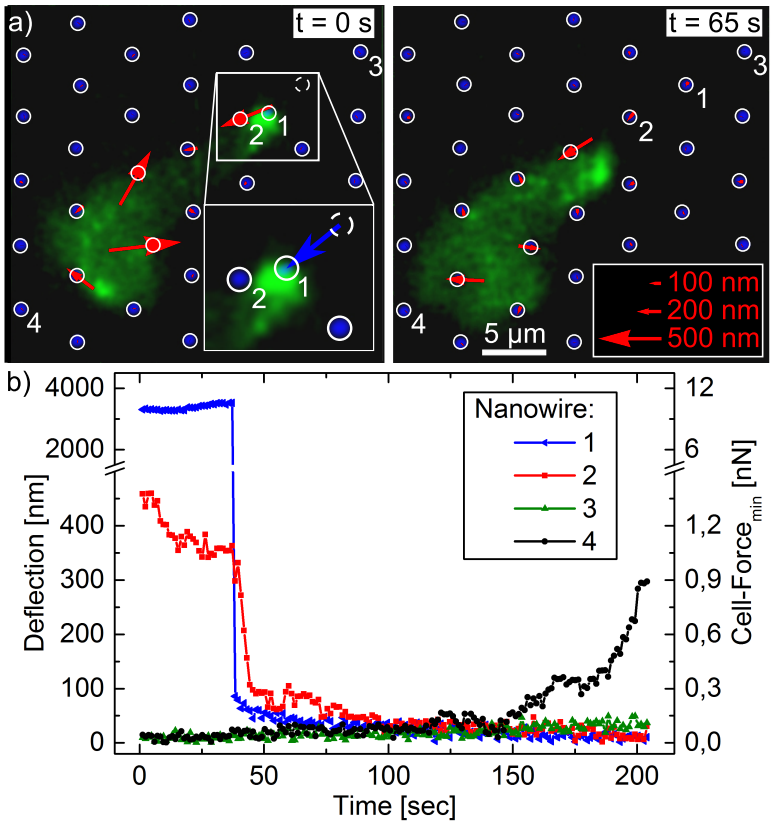

Figure 4.3: Cell-induced mechanical deflection measurement, without distortions. a) Fluorescence images of a migrating cell (green) labeled with Lim-GFP between the flexible nanowires (blue, reflection signal) at two time points. The red arrows denote observed nanowire deflections in respect to the reference frame. The red arrows are scaled by a factor of 10 for better visualization. The blue deflection vector in the inset is unscaled. b) Deflection measurement and calculated cell force over time for four distinct nanowires. Note that the contact height of the cell and the nanowire has to be obtained (e.g., from the confocal data) to calculate cell forces in this configuration. Reprinted with permission from Nano Letters, Article ASAP, 2018. Copyright 2018 American Chemical Society.

cell shape is accessible by a variety of optical microscopy techniques. Here, it is measured by confocal fluorescence microscopy as described in Section 3.3.

A Geometric Optics Model for Distortion Correction

In the proposed geometrical optics approach, the optical rays that are refracted at the cell boundaries are traced. With the help of two approximations, a differential equation that links the distortions to the 3D cell shape can be formulated: First, since the differences in refractive index within cells are in general smaller than the refractive index difference between the cell and the surrounding medium, an approximation of the cell as a compartment with a constant refractive index is made. The second approxima-

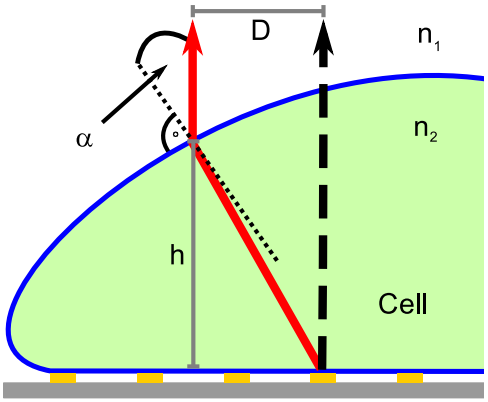

Figure 4.4: Schematic illustration of the optical refraction caused by an adherent cell. The apparent optical displacement D of a structure underneath the cell, caused by refraction, is shown by the path of the refracted ray (red arrow) and the reference ray without a cell (black dotted arrow). Reprinted (modified) with permission from Nano Letters, 2017, 17 (12), pp 8018–8023. Copyright 2017 American Chemical Society.

tion is that the distortion vector $\vec{d}(x,y)$ at a certain image position (pixel) is equal to the displacement $\vec{D}(x,y)$ of a single specific ray that exits the cell parallel to the optical axis at that position. In this subsection, the resulting model equation to correct for cell-induced distortions is derived. Then, in the following two subsections the two approximations that are made are discussed in detail.

The geometrical optics approach is schematically depicted in Figure 4.4, where the rays in the presence (red arrow) or absence (black dotted arrow) of a cell are displaced by a distance D due to Snell's law (see Equation 2.8). The differential equation for $d_x(x,y)$ is then given by Equation 4.1. For simplicity only the x-component of the distortion vector is displayed (for the derivation and the full equation, see Appendix A.1):

$$d_x(x,y) = \tan\left(-\sin^{-1}\left(\sin\left(\tan^{-1}\left(\frac{\mathrm{d}h(x,y)}{\mathrm{d}x}\right)\right)\cdot\frac{n_1}{n_2}\right) + \tan^{-1}\left(\frac{\mathrm{d}h(x,y)}{\mathrm{d}x}\right)\right) * h(x,y) \tag{4.1}$$

Here n_1 and n_2 are the refractive indices of the surrounding medium and the cell, respectively, which are taken from established literature (surrounding medium: $n_1 = 1.34$ [104] and A459 cell: $n_2 = 1.36$ [105]). Furthermore, $h(x,y)$ is the cell height at the point of refraction and $\mathrm{d}h(x,y)/\mathrm{d}x$ denotes the tangent of the angle α at that point, whereas α is the angle between the surface normal and the incident light ray.

Discussion on the Constant Refractive Index Approximation

In this subsection, specific considerations on common refractive index variations inside a cell are provided. Various causes for intracellular refractive

index differences have been reported in literature [106]. The cell refractive index can vary spatially, but also due to cell cycle, cell passage and from cell to cell. However, the most common distinction that is being made and quantitatively assessed, is the difference in refractive index between the cytoplasm and the nucleus [105, 107–110].
For that reason, here, the focus is put on this refractive index difference. To quantify such intracellular refractive index differences in relation to the refractive index difference to the surrounding medium, a ratio r is defined as $r = |n_{cytoplasm} - n_{medium}| \,/\, |n_{cytoplasm} - n_{nucleus}|$. The greater this ratio r, the more accurate is the approximation.
For the utilized cell line, A549, the refractive index difference between the cytoplasm and the nucleus is about 0.004 refractive index units while the difference between the cell and the medium is about 0.02 refractive index units [104, 105]. Therefore, a ratio of $r = 5$ is obtained. Furthermore, the feasibility of the approximation is assessed for various other cell lines, for which literature values for cytoplasm and nucleus refractive index could be found. The results are summarized in Table 4.2. No ratios $r < 1$ are reported.

Cell Line	$n_{cytoplasm}$	$n_{nucleus}$	Reference	r
A549	1.356	1.352	[105]	5.00
HeLa	1.360-1.390	1.355-1.365	[107]	1.42-4.00
HeLa	1.375	1.371	[108]	8.75
BEAS-2B	1.366	1.353	[105]	2.00
HVE	1.373	1.343	[105]	1.10
MCF-7	1.378	1.351	[105]	1.40
ASM	1.357-1.364	1.360	[109]	5.67-∞
CHO	1.372	1.392	[110]	1.60
HEK 293	Similar to HeLa	Similar to HeLa	[107]	See HeLa
Primary Rat Neuron	Similar to HeLa	Similar to HeLa	[107]	See HeLa
B35 Neuroblastoma	Similar to HeLa	Similar to HeLa	[107]	See HeLa

Table 4.2: Literature refractive index values of cytoplasm and nucleus for various cell lines and the corresponding ratio $r = |n_{cytoplasm} - n_{medium}| \,/\, |n_{cytoplasm} - n_{nucleus}|$ to estimate the feasibility of the constant refractive index approximation.

Discussion on the Single Ray Approximation

The second approximation that is used is that the image distortion d is equal to the displacement D of the ray that exits the cell parallel to the optical axis. To show that the single ray gives a good measure of the displacement of all the rays originating in a single point that exit the cell and are then collected by the objective, ray-tracing simulations of the optical system are performed. The microscope system is simulated with the cell as an additional lens, using ZEMAX (ZEMAX Development Corporation). The "cell-lens" is constructed as a hemisphere with 26 μm diameter whose center is located at $z = -3\,\mu m$, so that its maximum height is 10 μm. The refractive index of the cell is taken to be $n_{cell} = 1.36$, and a refractive index of $n_{medium} = 1.34$ is assumed for the medium. Rays that are emitted by point sources directly underneath the cell are refracted at the cell/medium interface, depending on the local cell shape (see Figure 4.5 a)). All the rays collected by the NA of the objective can now be traced to the image plane (see Figure 4.5 b)). It can be observed that the traced rays disperse in the image, but the chief (primary) ray position is in the center of the distribution. Additionally, the expected cell-induced distortions are computed with Equation 4.1. Comparable displacements are found for the chief ray in the ray-tracing simulation, and the ray traced in the model (see Figure 4.6). Hence, it is concluded that the single-ray approximation is reasonable.

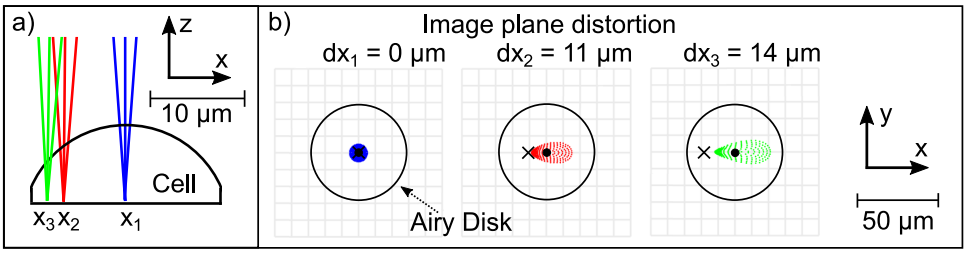

Figure 4.5: Ray-tracing simulation. a) Model of the cell as a lens in the microscopy system. Point sources directly underneath the cell emit light rays that are refracted at the curved cell boundary and then gathered by the objective to be imaged in the image plane. b) Image plane distortions of the rays from a). The colored dots mark the distorted rays that are imaged. The cross marks the undistorted image spot in the system without the cell. The black dot marks the centroid position of all imaged rays. Distortions in the image plane are magnified by a factor 100, corresponding to the magnification of the objective. Reprinted with permission from Nano Letters, 2017, 17 (12), pp 8018–8023. Copyright 2017 American Chemical Society.

Correcting Image Distortion

With the geometric optics model and Equation 4.1, the cell-induced distortions in an image can be predicted from the 3D shape of the cell, and in

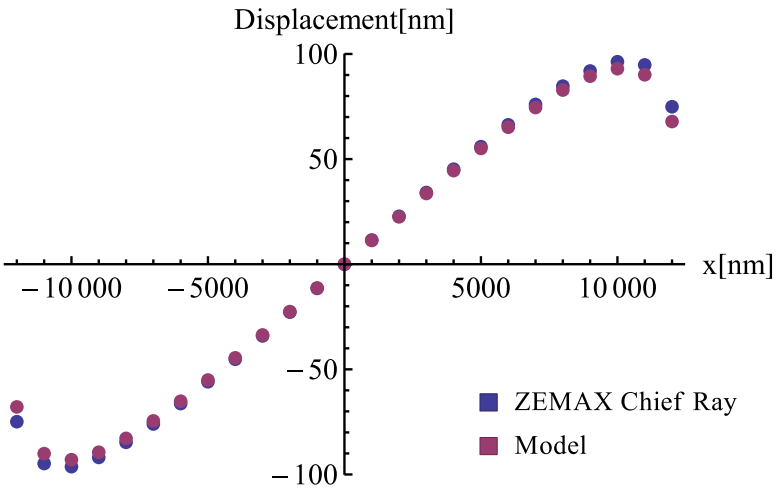

Figure 4.6: Cell-induced optical displacements of the chief ray derived from ray tracing (blue) and calculated using the single ray approximation (purple). The cell is modeled as a hemisphere, with a radius of 13 μm (centered at $x = 0\,\mu m$; $y = 0\,\mu m$; $z = -3\,\mu m$). Reprinted with permission from Nano Letters, 2017, 17 (12), pp 8018–8023. Copyright 2017 American Chemical Society.

turn, the image can be corrected by remapping it accordingly. Here, the 3D shape is obtained with confocal fluorescence microscopy as described in Section 3.3. For the previously analyzed cell in Figure 4.1 the confocally measurement 3D shape is depicted in Figure 4.7 a). For the remapping, the confocal measurement and the distorted image are aligned in x- and y-directions by aligning distinct structure localizations. For each image pixel, a distortion vector is calculated utilizing Equation 4.1. The parameters $h(x,y)$ and $\mathrm{d}h(x,y)/\mathrm{d}x$ are obtained by fitting a 2D polynomial to the confocal data. To correct image distortions, each image pixel is translated in accordance with the inverted distortion vector $-\vec{d}(x,y)$ at that pixel (purple translation grid in Figure 4.7 b)), thus deforming the image grid. The deformed grid is then mapped to the new, corrected image grid. This procedure is done using the OpenCV function "remap". In the Appendix A.2 the distorted image and the corrected image are shown (see Figure A.2). Even though little difference can be discerned by eye, the following distortion analysis reveals the achieved correction.

To quantify the quality of the correction, the corrected image is analyzed with the same reference framework as the original image. This is depicted in Figure 4.7 c). Compared to the measured displacement vectors $\vec{d}_m$ in the original image (see Figure 4 c)), the corrected displacement vectors $\vec{d}_c$ in the corrected image are distinctly reduced in the area occupied by the cell. The reduction is depicted quantitatively in the optical displacement distribution in Figure 4.7 d). The effective mean distortion induced by the cell, as well as the width of the distortion distribution, is reduced by as much as a factor of three, from 85 nm to 27 nm and from 52 nm to 17 nm, respectively. To evaluate the correction for systematic errors the angle φ between the corrected and measured distortion vectors (see inset in Figure

4.7 d)) is analyzed. The distortion at a structure is defined as being under-corrected if the vector $\vec{d}_c$ points in same direction as $\vec{d}_m$ ($|\varphi| < \pi/2$) and over-corrected if it is pointing in the opposite direction ($|\varphi| > \pi/2$). In Figure 4.7 e) the absolute change in vector length through the correction $d_\varphi = |(|(\vec{d}_m)| - |(\vec{d}_c)|)|$ is depicted for each structure, using a separate color scale for under-corrected (blue) and over-corrected (purple) structures (for details, see Figure A.3 in the Appendix A.2).

The largest corrections are achieved at the border region of the cell, where the greatest distortions occur. These areas tend to be slightly under-corrected. Note that there are no distinctly visible correction errors induced in the cell center, where the nucleus is located, which confirms the constant refractive index approximation. No free fitting parameters are used, as the correction solely relies on Equation 4.1, the confocal data and literature values. The correction approach dispenses with the use of a reference framework. It therefore enables distortion correction for techniques that cannot practically implement a reference framework, like traction-force microscopy, but also for fluorescence methods that image at various planes inside the cell. The correction by a factor of three also improves the localization accuracy in these techniques by the same amount. This improvement is comparable in magnitude to image quality improvements due to adaptive optics in thick tissue imaging [111] and does not require extensive computing.

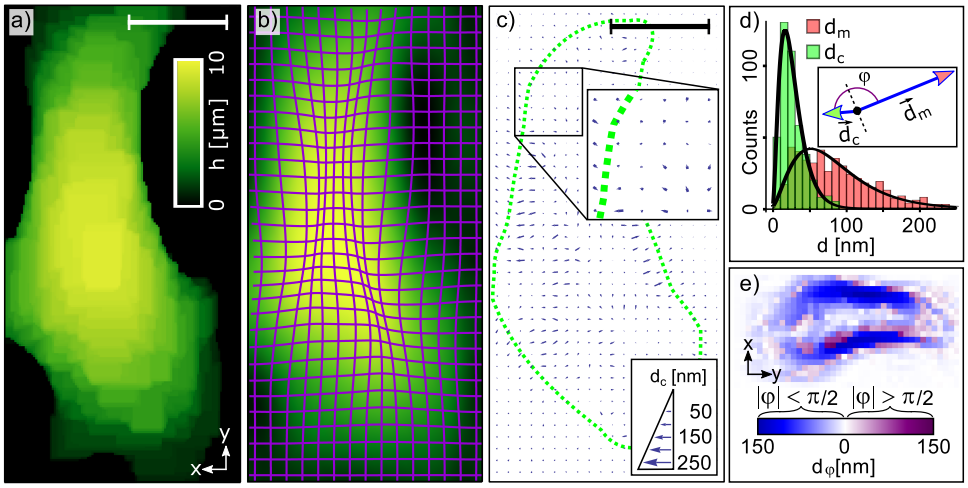

Figure 4.7: Correction method and quality of correction. a) Derivation of cell heights from confocal fluorescence measurement. Scale bar: 10 nm. b) Cell shape fitted to confocal data (yellow-green with the same scale bar as in a) and corresponding translation grid for the remapping (purple). c) Distortion field (d_c) of the corrected image. The top inset shows a two-fold enlargement, while the bottom inset shows the scaling vectors. d) Absolute distortion distribution in the original (d_m) and the corrected (d_c) image. The inset shows a cartoon schematically depicting structure distortions before and after correction. e) Absolute change in distortion following the correction. Under-corrected areas are defined as areas where the vectors point in the same direction ($|\varphi| < \pi/2$) before and after correction, and over-corrected areas are defined as areas where they point in opposite directions ($|\varphi| > \pi/2$). Blue colors denote under-corrected distortions, while purple colors denote over-corrected distortions. Reprinted with permission from Nano Letters, 2017, 17 (12), pp 8018–8023. Copyright 2017 American Chemical Society.

5

3D CELL SHAPE RECONSTRUCTION FROM DISTORTIONS

5.1 CELL SHAPE VISUALIZATION METHODS OVERVIEW

Methods that allow measuring the shape of living cells are of interest when looking for cell responses to external cues and measuring cell dynamics. Examples are the exposure of cells to confined surroundings [112, 113] or the testing of cell morphology responses to drug exposure [114, 115]. Furthermore, the cell shape can be used to detect the state of the cell in the cell cycle [116–118], the fitness of cells [119] and the occurrence of specific cell programs like necrosis or apoptosis [120] as well as cell differentiation [121].

The most commonly utilized tool to measure cell shape in 3D is fluorescence microscopy, where for example the cell membrane is labeled with a fluorescent marker, and the fluorescence signal of the marker is measured and tracked over time (see Section 2.1). However, there is one inherent drawback to this technique: The fact that the label itself can induce changes to the cell behavior and therefore bias results [122]. Additional disadvantages are the effects of phototoxicity and photobleaching of the fluorescent marker over time, which limit the time and number of images that can be taken [36, 123]. Together these drawbacks foster a need for other label-free and fast 3D cell shape visualization techniques [124, 125].

Atomic force microscopy is another invasive technique that can be used, but since it is inherently slow, it does not provide a suitable option for most 3D live cell imaging tasks.

More recently, quantitative phase imaging [126, 127] has been established as a method for single-shot, label-free 3D cell shape measurements, as it can circumvent the drawbacks of the fluorescence techniques. The method can thus be utilized to measure fast cell volume changes, e.g. due to osmotic changes [128] or apoptosis [129]. To measure the 3D shape of cells, such techniques utilize the cell refractive index and are thus similar to the method proposed here. However, they are reliant on measuring cell-induced phase shifts, thereby requiring specialized equipment like Michelson interferometer-based setups [126].

5.2 SINGLE SHOT, LABEL-FREE 3D CELL SHAPE RECONSTRUCTION

In addition to the enabled correction in Section 4.4, one further advantage of the derived relation is that Equation 4.1 and the measured distortion field can also be used for fast 3D cell shape reconstruction without the need for labeling. For the 3D reconstruction, the initial value problem (Equation

4.1) needs to be solved for the cell height $h(x, y)$ for the measured distortion field. The mathematical procedure is provided in the following paragraph.

For the 3D reconstruction, Equation 4.1 is solved for $h(x, y)$ using Mathematica. This is done in 1D along different paths. The need to use this procedure arises from the fact that the measured discrete vector field cannot be assumed to be conservative, and therefore the line-integral cannot be assumed to be path independent. Figure 5.1 a) shows the distortion measurement of the cell previously evaluated in Chapter 4. The distortions have been quantified for periodic points along 40 lines and 23 columns. Here, each line is chosen as a 1D path to solve Equation 4.1. The red outline in Figure 5.1 a) is an exemplary part of one such path and is depicted in magnification in Figure 5.1 b). For each path, the projection of the distortion vectors along the path direction is taken (see Figure 5.1 c)), and the distortions are interpolated between the measured data points. The distortion vectors below a length threshold of $5\,nm$ are set to $0\,nm$ in order to minimize noise errors outside the cell. For each path, the boundary condition of the ordinary differential equation is fixed by setting the height at the lowest point (determined by prior evaluation) outside of the cell to $0.01\,\mu m$. This procedure guarantees that the equation is solvable along the whole path and yields only positive values. In this way, Equation 4.1 can be solved numerically. For the exemplary measured distortions (the red framed distortions in Figure 5.1 a-c)) the resulting solution to Equation 4.1 for h_1 is depicted in Figure 5.1 d). To minimize height errors due to the interpolation between the measured discrete 2D lattice of optical displacement vectors, the equation is not only solved along the 40 lines. Instead, for each lattice point, the equation is solved along four different straight paths (line, column, and two diagonal directions) and the resulting heights h are subsequently average. After interpolating between the 2D lattice points, the 3D cell shape is obtained, as depicted in Figure 5.1 e).

5.3 COMPARISON TO CONFOCAL MICROSCOPY

To validate the proposed 3D cell shape reconstruction method, the cell shape of the reconstructed cell has also been measured by using fluorescent labels (see Section 3.3). Figure 5.2 a) depicts the 3D reconstruction from the distortion data for the cell shown in Figure 4.1. Figure 5.2 b) shows a comparison of the reconstructed (red) and confocal (white) cell shapes in three equidistant cell cross-sections (c1-c3). The reconstructed cell heights overlap well with the outlines of the raw confocal data. The two methods exhibit a close shape and volume resemblance (see Appendix A.3), showing only a 3% volume difference. The quality of agreement is particularly striking, given that no free fitting parameters are used for the 3D reconstruction, and only a single 2D image is required.

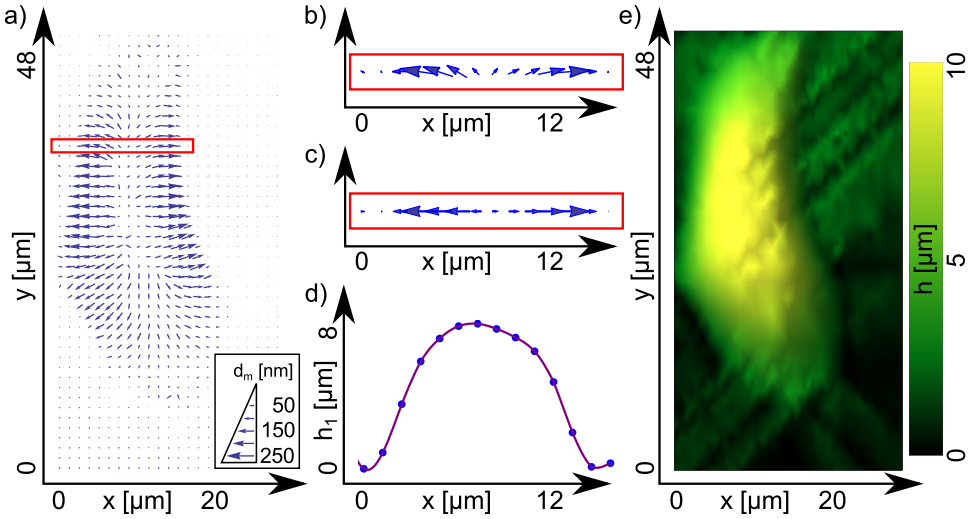

Figure 5.1: 3D reconstruction procedure. a) Distortion measurement of a cell. For the 3D reconstruction the differential Equation 4.1 is solved along 1D paths. b) Exemplary part of one path, magnified from a). c) Projection of the distortion vectors (from b)) along the path direction. d) Numerical solution to the differential equation utilizing the projections from c). e) Label-free 3D reconstructed cell shape after solving the equation for each lattice point along four different paths and subsequent averaging.

Since the proposed 3D cell shape reconstruction is label-free and relies only on a single shot 2D image, it offers the advantage of low system requirements in comparison to confocal microscopy. Furthermore, the cell function is not impaired by markers [130] and the method thus provides a tool for cell volume studies [128, 129, 131, 132] on long time scales, since it is not limited by the bleaching of fluorophores or long exposure times. In the Appendix A.4 a 3D reconstruction time-series is depicted from a time-lapse measurement of the cell-induced distortion field over a period of 4.5 hours with 8.000 frames. Figure 5.3 a) shows three representative frames of the distortion field induced by three cells at the beginning of this time-lapse series. Due to the high signal-to-noise ratio between the cell and the background, the distortion measurement also enables a high-contrast 2D visualization of the cells by using a color scale for the absolute vector lengths (see Figure 5.3 b)). In Figure A.5 in the Appendix A.4 and Figure 5.3 c) the cells are reconstructed in 3D and typical changes of the cell contour during cell migration, such as leading-edge lamellipodia and cell contraction at the trailing edge [21], as well as cell division, are observed.

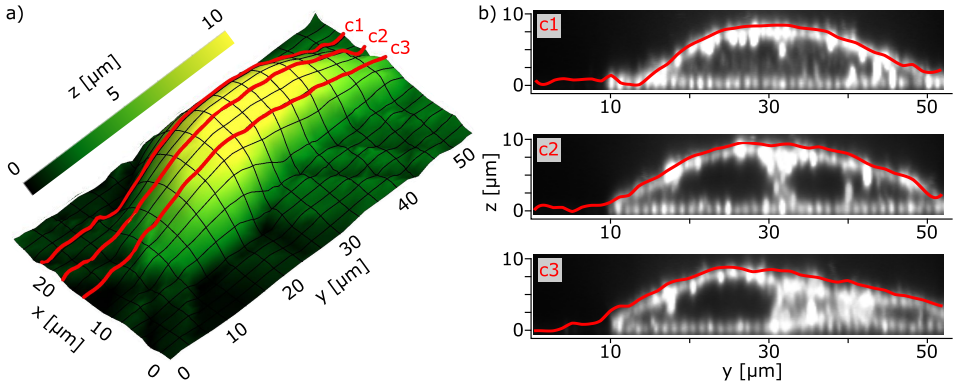

Figure 5.2: Validation of the 3D reconstruction method. a) Reconstructed shape of the cell depicted in Figure 4.1 a). b) Micrographs of the labeled cell at different cross-sectional levels (c1-c3). The red lines correspond to the reconstructed height, while white areas show high fluorescence intensity in the confocal measurement. Reprinted with permission from Nano Letters, 2017, 17 (12), pp 8018–8023. Copyright 2017 American Chemical Society.

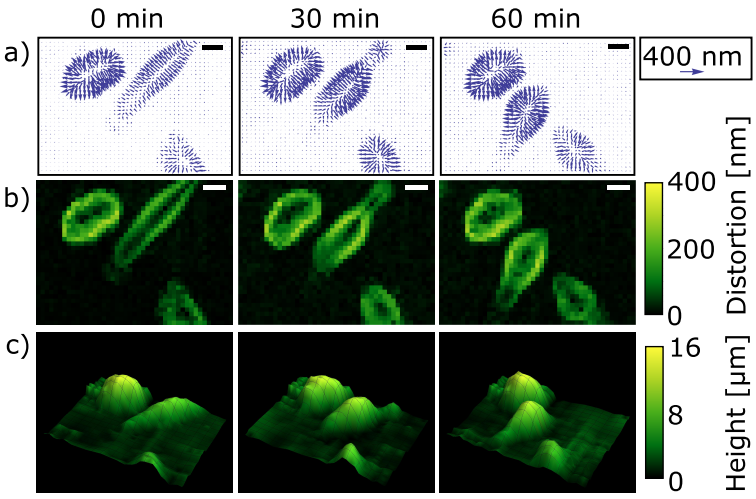

Figure 5.3: Time series of the distortion field induced by HuH7 cells on a lattice of gold nanostructures. The structure periodicity is 2 μm, and the interval between frames is 30 minutes. a) Vector plots of the optical nanostructure displacements. The vector lengths are enhanced relative to the spatial distance. A scale vector is plotted at the top right. b) High-contrast plots of a) with absolute vector lengths on a color scale. Scale bars are 10 μm. c) Reconstructed 3D time-lapse frames from the distortion data in a). Reprinted with permission from Nano Letters, 2017, 17 (12), pp 8018–8023. Copyright 2017 American Chemical Society.

Part III

RESULTS - DIFFRACTION-BASED DETECTION

6

DIFFRACTION ANALYSIS OF CELL ENSEMBLE RESPONSES

6.1 THE NEED FOR LABEL-FREE, HIGH-THROUGHPUT SENSORS

In vitro culturing of cells plays an important role in cancer research [133] and drug discovery [134] as cell-culture-based tests are frequently utilized in pre-clinical studies. The cost of these *in vitro* tests is considerably lower than the typical cost of clinical trials, and they therefore provide a useful first test for cheap and efficient drug discovery. Various hallmarks for cancer have been identified [135], and there exists a variety of assays for studying hallmarks such as cytotoxicity, genotoxicity, cell proliferation, apoptosis, wound healing, gene expression or protein expression [136]. These assays can be split into two broad categories: cell-based assays and biochemical assays [137]. They generally allow for high throughput screening [138], utilizing ensembles of cells. The experiments can be carried out in multi-well formats, thereby providing simultaneous results for multiple experimental parameters.

From among the phenotypic traits of a cell line, cytotoxicity is commonly assessed by utilizing dyes, such as trypan blue or red-fluorescent propidium iodide to probe the cell membrane integrity and thus differentiate between living and dead cells. Cell viability assays test for the metabolic activity of the cells, thereby generating an indirect measure of the number of viable cells. Typical viability assays are the MTT assay, which is a colorimetric assay that assesses the metabolic reduction of tetrazolium salts, and the ATP assay, which detects apoptosis or necrosis by sensing ATP levels using the enzyme luciferase. Cell proliferation can furthermore be assessed by monitoring the cells DNA synthesizing capability, e.g., by measuring the integration of the label-substances 3H-thymidine or 5-bromo-2'-deoxyuridine into the DNA.[1]

There are two key limitations that all these assays have in common. First, they are endpoint assays, providing only a single readout. Therefore, they can not provide information about time-resolved dynamics. Second, they utilize labels and are therefore invasive, which can alter the cellular function or response [122]. To overcome these limitations, electric cell-substrate impedance sensing has been introduced as a label-free technique that allows a continuous, real-time readout [139, 140]. In electric cell-substrate impedance sensing, cells are seeded on electrodes in specialized well-plates, and the impedance of the cell layer is measured, which correlates with the number of cells on the electrode. Impedance-based techniques have been used to measure cell proliferation [141] and cytotoxicity [142] as well as cell morphology changes[143]. Two similar, but optical techniques with

1 Further assays are summarized in the paper by Ramesh et al. [136].

the same advantages over traditional assays are surface plasmon resonance [144] and resonant waveguide grating [145]. In surface plasmon resonance sensors, a prism is utilized to induce an evanescent field on the metallic bottom of a well plate. The evanescent field is influenced by the refractive index of the cell layer in the well plate, and thus its resonant angle depends on the cell morphology and confluency [146]. This technique also has been utilized to measure cell morphology [147] but has not yet been incorporated in a high throughput setup [148]. In resonant waveguide grating, the evanescent field is induced by integrating optical gratings on the bottom of specialized and expensive well plates, which can be utilized in high throughput [149]. Thus, while cell-substrate impedance sensing and the two optical assay techniques allow for label-free, high throughput readouts of cytotoxicity, cell viability, cell proliferation, and cell morphology, all of them need specialized culture plates. This chapter investigates the feasibility of using a diffraction-based method to provide similar readouts while overcoming the limitation of requiring non-standard culture plates. To this end, the working principle of the proposed diffraction method is introduced. This working principle is validated by experiments and simulations, and drug screening experiments are performed.

6.2 WORKING PRINCIPLE OF THE DIFFRACTION METHOD

In this section, a diffraction method that can be utilized as the basis for a cell-based drug screening assay is introduced. The basic working principle of the method is visualized in Figure 6.1. The method employs a nano-structured diffraction grating, which simultaneously acts as a substrate for eukaryotic cells.[2] By illuminating the nano-structured grating with a coherent light source, the light gets diffracted on the grating, and a diffraction pattern occurs (see Section 2.3). The intensity of a diffraction peak is influenced by the ensemble of cells on top of the grating, as the cells change the optical path of some elementary light waves and thus alter the interference conditions of the resulting diffraction pattern. From the diffraction peak intensity changes - induced by the cell ensemble - specific physical properties of the cell ensemble, like its confluency and its average curvature can be inferred.

In the following subsection, the different optical phenomena, which occur due to the presence of adherent eukaryotic cells in the optical path, are discussed. To this end, an equation or model for the diffraction peak intensity that incorporates the various optical effects of the cells is derived. With the help of this equation, the working principle of the diffraction method can

2 Note that the grating can also be placed in a distance to the cells, as will be shown later, and thus does not limit the method to specialized culture plates. Additionally, the method is not limited to eukaryotic cells but can be used for any so-called phase objects, i.e., objects with a different refractive index than the surrounding medium.

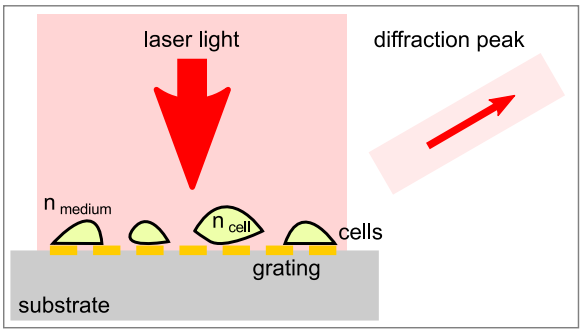

Figure 6.1: Working principle of the diffraction method. Laser light is diffracted by a grating, which acts as a substrate for cells. The intensity of a diffraction peak is recorded. From the change in diffraction peak intensity due to the presence of the cells, physical properties of the cells can be inferred.

be described in quantitative terms. The aforementioned physical properties of the cell ensemble are discussed in detail in Section 6.3.

An Optical Model of the Diffraction Peak Intensity

The optical model presented in this section has been derived in cooperation with Jonas Zähringer, and has previously been shown in the associated master thesis [150].

Diffraction on a grid of circular apertures has been discussed in Section 2.3. To obtain a term that is proportional to the intensity distribution of the diffraction pattern on a $N\,x\,N$ grid of nanostructures, Equation 2.31 is plugged into Equation 2.36. Omitting constants, this yields:

$$\begin{aligned} I(k_x, k_y) &\propto \left| J_1(k_x.k_y) \sum_{n=0}^{N-1} \sum_{m=0}^{N-1} e^{-i(k_x P n + k_y P m)} \right|^2 \\ &= \left| J_1(k_x, k_y) \sum_{n=1}^{N^2} e^{-i(k_x \cdot x_n + k_y \cdot y_n)} \right|^2 \end{aligned} \tag{6.1}$$

With this equation, the diffraction pattern of a periodic grid with given structure-positions (x_n, y_n) can be calculated. However, due to the cells on top of the grid, several optical effects occur, changing the resulting diffraction pattern. In order to quantitatively account for these effects, they have to be implemented into the diffraction Equation 6.1.
As shown in Table 4.2, eukaryotic cells have a refractive index that usually differs from the refractive index of the surrounding medium. Although the cellular refractive index can also differ within a cell or within different cell compartments, for this model it is assumed to be constant as argued in Section 4.4. This refractive index difference causes refraction of the laser light at the cell boundaries and thus results in optically distorted grid positions, which in turn change the interference condition of the diffracted

light. In order to calculate the distortions that are expected for each grid point, Equation 4.1 as derived in Section 4.4 can be utilized. However, there is one difference. Previously, the refracted light ray that was perpendicular to the substrate has been optically displaced. Here, instead, the optical displacement of the light ray that occurs at an angle θ and contributes to the diffraction intensity at that angle has to be calculated. Therefore Equation 4.1 has to be modified to:

$$\begin{aligned} d_x(x,y) = &\left(\tan\left(-\sin^{-1}\left(\sin\left(\tan^{-1}\left(\frac{\mathrm{d}h(x,y)}{\mathrm{d}x}\right)-\theta\right)\cdot\frac{n_1}{n_2}\right)\right.\right. \\ &\left.\left.+\tan^{-1}\left(\frac{\mathrm{d}h(x,y)}{\mathrm{d}x}\right)-\theta\right)*h(x,y) \end{aligned} \tag{6.2}$$

A derivation of this formula can be found in [150].

The change in the diffraction pattern of a grid with optically displaced structures is calculated by adding a distortion term $(\Delta x_n, \Delta y_n)$ to every grid structure.

$$I(k_x,k_y) \propto \left| J_1(k_x,k_y) \sum_{n=1}^{N^2} e^{-i(k_x\cdot(x_n+\Delta x_n)+k_y\cdot(y_n+\Delta y_n))} \right|^2 \tag{6.3}$$

Due to the difference in refractive index between the cell n_{Cell} and the medium n_{Medium}, additionally a phase shift φ is introduced by the adherent cells. This phase shift is given by the optical path length difference, with l_{Cell} being the path length the light travels through the cells, and l_{Medium} being the respective path length without the cells.

$$\varphi = 2\pi(n_{Cell}\, l_{Cell} - n_{Medium}\, l_{Medium})/\lambda_{vac} \tag{6.4}$$

This phase shift is added individually to each grid point, as it depends on the local shape of the cells on top of the corresponding grid point.

$$I(k_x,k_y) \propto \left| J_1(k_x,k_y) \sum_{n=1}^{N^2} e^{-i(k_x\cdot(x_n+\Delta x_n)+k_y\cdot(y_n+\Delta y_n)-\varphi_n(x_n,y_n))} \right|^2 \tag{6.5}$$

In addition to the intensity changes due to refractive index differences, the diffraction pattern is also influenced by the absorption and scattering of light due to the cells. If the cells are not evenly distributed on the grid, then at some grid points more light is absorbed by the cells, and thus the corresponding grid points do not contribute equally to the diffraction signal. Therefore, an extinction parameter A is introduced:

$$A(x,y) = e^{-(\kappa\cdot l_{Cell}(x,y))} \tag{6.6}$$

Here, κ is the material specific extinction coefficient. Adding an extinction

parameter to every grid point individually, the final model equation reads:

$$I(k_x, k_y) \propto \left| J_1(k_x, k_y) \sum_{n=1}^{N^2} A_n(x,y)\, e^{-i(k_x \cdot (x_n + \Delta x_n) + k_y \cdot (y_n + \Delta y_n) - \varphi_n(x_n, y_n))} \right|^2 \quad (6.7)$$

With this equation, relative changes to the diffraction pattern in general and to a diffraction peak intensity in particular, can be predicted if the changes are induced by cells on top of the diffraction grid. However, in order to utilize the model, several physical properties of the cells or the cell ensemble have to be obtained first. Table 6.1 summarizes these parameters and illustrates how they can be obtained.

physical quantity	relevant for	obtained from
n_{Medium}	distortion, phase	literature [104]
n_{Cell}	distortion, phase	literature [105]
κ	extinction	literature [150, 151]
$h_{Cell}(x,y)$	distortion, phase, extinction	3D shape
$\frac{\mathrm{d}h_{Cell}(x,y)}{\mathrm{d}x}, \frac{\mathrm{d}h_{Cell}(x,y)}{\mathrm{d}y}$	distortion, phase, extinction	3D shape
$l_{Medium}(x,y), l_{Cell}(x,y)$	phase, extinction	3D shape

Table 6.1: Summary of the physical parameters needed for the model.

6.3 EXPERIMENTAL VALIDATION OF THE DIFFRACTION MODEL

In this section, the optical model, which is derived in the previous section, is validated. Therefore, a setup is introduced, which allows measuring the 3D shape of the cells in a cell ensemble on top of a nano-structured grating over time via fluorescence microscopy. For each time-point, the respective 3D cell shapes then provide the parameters needed for the model (as summarized in Table 6.1). The setup furthermore allows to simultaneously measure the intensity of a diffraction peak of the laser-illuminated, cell-covered grating over time. Together, this direct measurement of the diffraction peak intensity and the simultaneous calculation of the peak intensity via the proposed model provide a means to compare the two methods and thus validate the model.

The combination of the two measurements is achieved by implementing the diffraction setup into a microscopy setup (see Figure 6.2). The microscopy setup is based on a Ti-E Eclipse inverted microscope as described in Section 3.3. Here, the utilized camera is a Zyla sCMOS camera (Andor Technology) with a field of view that is four times larger than the one of the previously utilized Clara E camera. This allows for imaging a grating with greater length and width and thus also enables measurements with more cells on the grating. For the 3D shape measurement, the cells are stained

as described in Section 3.3. Image z-stacks are recorded with a step size of 300 nm. For the diffraction measurement, a laser additionally illuminates the sample from the top. The diffraction illumination- and detection-part of the setup employs the same components as the diffraction setup introduced in Section 3.4. The only difference is that the substrate with the diffraction grating is directly attached as the bottom slide of a 6-channel μ-slide (6-channel sticky slide, ibidi). For a more detailed description, see [150].

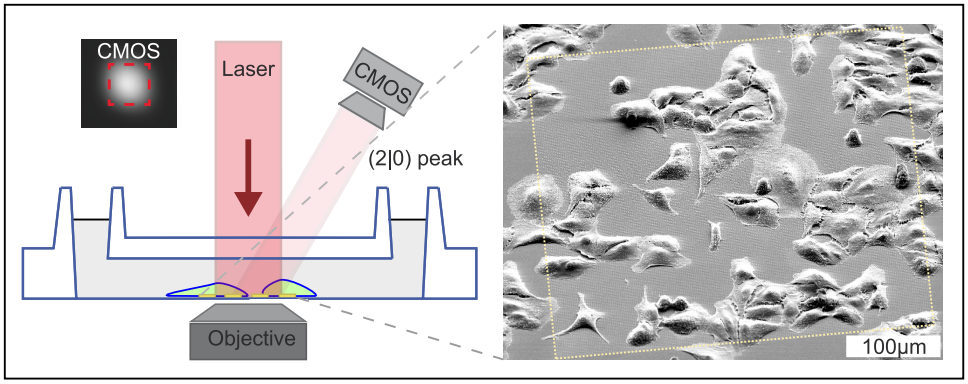

Figure 6.2: Integration of the diffraction setup into a microscope. The $(2|0)$-diffraction peak of a laser on a grating with adherent cells on top is measured with a CMOS sensor. Simultaneously, the 3D cell shapes are recorded utilizing fluorescence microscopy. This combination allows comparing the proposed model with the direct intensity measurement. The right panel shows a scanning electron micrograph of an ensemble of fixed A549 cells on a surface periodically patterned with gold nanostructures.

Validation Experiments

To validate the proposed model, two time-lapse measurements are performed, and the diffraction peak intensity, as well as the 3D cell shapes of the cells on top of the grating, are measured simultaneously. To this end, $A549$ cells are seeded directly on top of the gold-nanostructure diffraction grating with a size of $(120 * 120)\,\mu m^2$. The 3D cell shape and the $(2|0)$-diffraction peak is recorded over several hours. This peak was chosen for practical reasons and for a high signal-to-noise ratio as explained in Section 3.4. From the 3D cell shape and literature values (see Table 6.1), all the model parameters are obtained, and the model diffraction pattern is computed. The angle ϕ of the $(2|0)$-diffraction peak can be calculated via:

$$\phi_m = \arcsin\left(\frac{m \cdot \lambda}{p}\right) \tag{6.8}$$

Here, m is the order of the diffraction peak, p is the grid periodicity and λ is the wavelength of the illumination light. For the model, the intensity

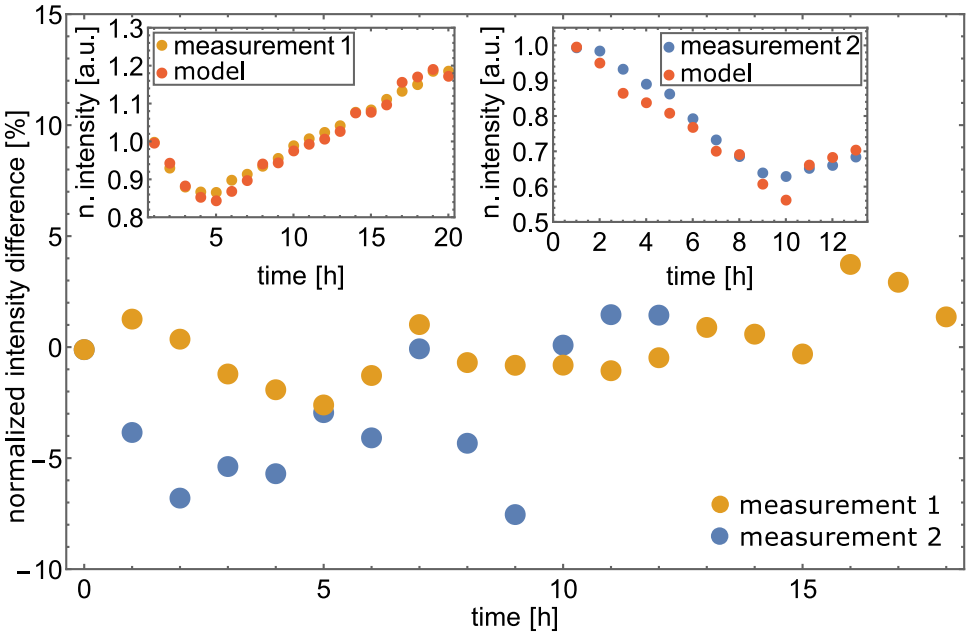

Figure 6.3: Intensity difference between the modeled and the measured diffraction peak over time, for two measurements with A549 cells on top of the diffraction grating. The insets show the modeled and the measured normalized intensities of the two separate measurements over time. Figure adapted from [150].

maximum around the angle ϕ is calculated by integrating the intensity over a solid angle that encapsulates the whole diffraction peak up to the first side-minimum.

Figure 6.3 shows that the modeled diffraction peak intensity change over time and the experimentally obtained diffraction peak intensity change are correlated with each other. The two insets show the measured and modeled relative intensity curves for the two measurements with A549 cells on top of the diffraction grating. The obtained 3D shapes of the cells on top of the grid, which have been used for the modeling, are furthermore depicted in Appendix A.5 at different time points. As the cells change their shape over time, the diffraction intensity changes as predicted by the model. In the main panel of the figure, the normalized intensity difference between measurement and model is plotted. For the depicted measurements, the absolute difference between the two is always within 10 %, with the average absolute difference being 2.0 %. A possible source for these differences is the simplification made in the modeling, where a constant refractive index is assumed for the whole cell. Another possible source for errors is the shape fitting that is performed using the fluorescence measurement of the cell membrane. Overall, however, the model's prediction is excellent as the coefficient of determination r^2 for the correlation between measurement and model is close to 1 for both measurements. For Measurement 1 it is: ${r_1}^2 = 0.986$ and for Measurement 2 it is: ${r_2}^2 = 0.945$.

The diffraction peak intensity change that is induced by the cell ensemble is quantitatively well described by the optical model provided in Equation

6.7. Therefore, the setup which is utilized in the remainder of this thesis omits the additional microscopy unit, which was used to measure the 3D cell shape of the cells in the cell ensemble. Instead, it is optimized to work as a diffraction assay in high throughput. The setup is introduced in detail in Section 3.4. The main difference is that in this setup the cells are not placed directly on the diffraction grating, but in a standard culture dish, e.g., a 6-channel slide. The diffraction grating is placed directly underneath the bottom of the culture dish[3] and a motorized stage allows moving the culture dish freely above the grating, thus enabling a high throughput setup with successive measurements of many different samples or channels. Additionally, the setup allows probing the confluency of the cell ensemble as well as primary cell morphology with a CMOS-sensor that images the interference pattern of the cell ensemble (holographic imaging setup, see Section 3.4 and [76]).
The fact that the cells are not placed directly on the diffraction grating but instead with a distance to it does not change the signal characteristics. Only the magnitude of the intensity change that is induced by the changes of the cell ensemble decreases with increasing distance between grating and cells. This is shown in detail in Appendix A.6. To maximize the signal to noise ratio and to guarantee continuity between measurements, the distance between the diffraction grating and the cells is thus minimized and kept constant in all the measurements.

A Simplified Proportionality Relation

In the previous subsection, it has been shown that the model is able to reliably predict the intensity change of the diffraction signal over time for a given cell ensemble. However, to employ the method for drug screening applications, the intensity signal is to be used as a readout. Therefore, the goal of this subsection is to conclude on the physical properties of the cell ensemble from the intensity signal. To provide a more intuitive understanding of the signal in the context of drug screening applications, the dependency of the diffraction intensity on the physical properties of the cell ensemble is derived in a simplified form.
From the previous considerations, resulting in Equation 6.7, it is apparent that the cell confluency, cell height, cell volume, and the cell curvature are the physical properties that change throughout a measurement and contribute to the intensity signal change. The refractive index and the extinction are cell-specific and should stay constant throughout a measurement. To deduce a simplified proportionality relation between the mentioned physical properties and the diffraction intensity, one can look at different cell ensemble states, defined by different confluency, cell volume and average cell curvature, and the corresponding diffraction intensity.
To this end, growth experiments starting with single cells on a grid, where

3 In the setup integrated into the microscope that is discussed above, this is not possible, since the objective utilized for the 3D cell shape measurement is placed directly under the specimen.

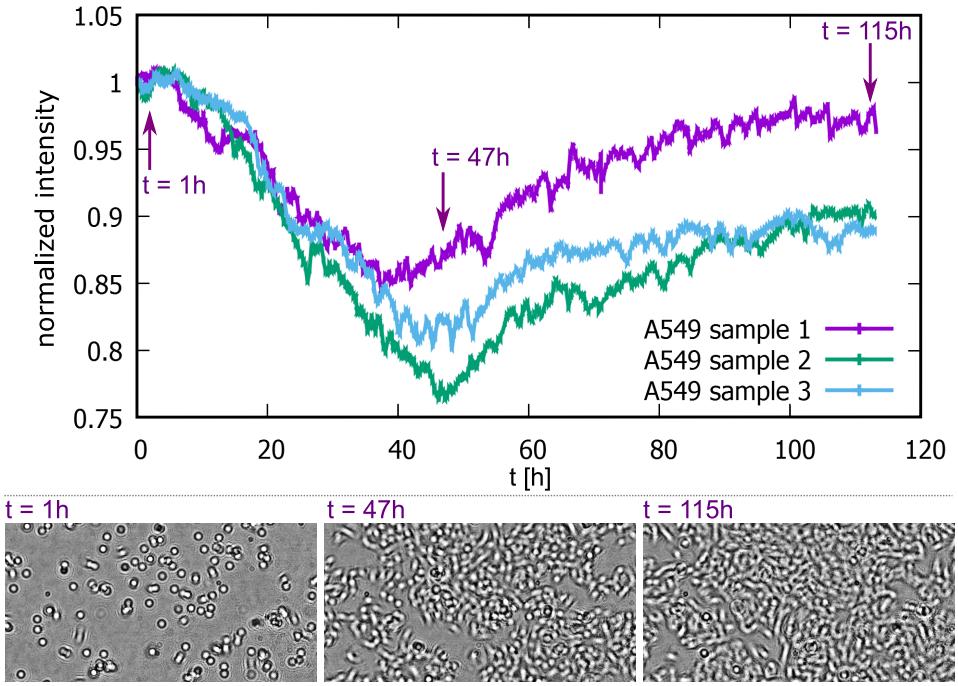

Figure 6.4: Normalized diffraction intensity evolution of three proliferating cell ensembles. The characteristic dip at around $40 - 50$ hours is due to the closing up of the cell ensemble. In the bottom panel, images of the cell ensemble, which are recorded with a CMOS sensor, corresponding to Sample 1 at three distinct times are shown, to visualize the corresponding confluency change.

many different ensemble states are observed, are carried out. The corresponding intensity curves for three such experiments are depicted in Figure 6.4. The observed dip in the diffraction intensity, here at around $40 - 50$ hours, is characteristic of all proliferation experiments and has been observed before [152]. To explain this characteristic, a simplified proposition is made as follows: As the cells grow, they induce more optical disturbances to the grid and thus the diffraction intensity drops. At a certain confluency, the cells form clusters and thus the overall curvature of the cell surface decreases. Lower overall curvature causes the induced disturbances to become more homogeneous over the cell ensemble and thus the diffraction intensity increases again. To show that this simplified proposition can explain the intensity curves in the proliferation experiments, it is summarized in a proportionality relation and simulations subsequently test this relation.

In Figure 6.5, four different and simplified states of a cell ensemble in a proliferation experiment are depicted. The cells are seeded in low confluency (a). They start to proliferate, causing the confluency to increase (b) and subsequently form small and then larger clusters and finally reach full confluency (c). This growth behavior can be observed in the lower panels of Figure 6.4. When a nearly confluent cell layer has been formed, the proliferating cells fill in the still unoccupied spaces, and hence a more uniform

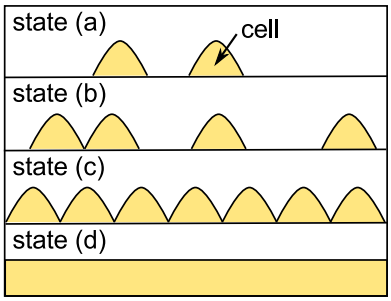

Figure 6.5: Different states of proliferating adherent cell ensemble. Cells are seeded as single cells with low confluency (a). They proliferate and then form smaller clusters (b). At full confluency (c), the cell ensemble is closing up and forms a closed uniform layer (d).

layer is formed (d).
To find a phenomenological relation between the observable physical quantities in the experiment, the qualitative change in confluency, overall cell volume and overall cell curvature in the transition from state (c) to state (d) is investigated. Here, as the cells have already formed a confluent layer, the confluency ($c_{ensemble}$) stays approximately constant. While the overall cell volume ($V_{ensemble}$) increases, the overall cell curvature decreases. Since the diffraction peak intensity is increasing in this part of the experiment, a linear relation can be formulated as follows:

$$I \propto \frac{V_{ensemble}}{\sum_{n=1}^{N} |\nabla h_n(x,y)|} \tag{6.9}$$

Here, $\sum_{n=1}^{N} |\nabla h_n(x,y)|$ is used as a measure for the overall cell curvature, with N being the number of grid point of the grating. Note that the linearity in the relationship is assumed for simplicity and will be tested in a simulation, later in this section.
For the transition from a low confluency state (a) to a certain higher confluency state (b), the experimentally measured diffraction intensity is decreasing. However, confluency, overall cell volume, and overall cell curvature are increasing linearly with the number of cells. The proportionality in Equation 6.9 thus equals to $\frac{V_{ensemble}}{\sum |\nabla h(x,y)|} = 1$. To still hold true for this transition, Equation 6.9 thus has to be expanded to:

$$I \propto \frac{V_{ensemble}}{c_{ensemble} \cdot \sum_{n=1}^{N} |\nabla h_n(x,y)|} = \frac{\bar{h}}{\sum_{n=1}^{N} |\nabla h_n(x,y)|} \tag{6.10}$$

Here, $c_{ensemble}$ is the confluency and $\bar{h}$ is the mean cell height. The relation states that the diffraction intensity is proportional to the mean cell height divided by the overall cell curvature. Therefore, the diffraction intensity can be understood to correspond to the inverse surface roughness of the cell ensemble.
To confirm the proposed proportionality relation, a proliferation experiment, in which also the 3D shape of the cell ensemble is measured, could in principle be performed. Due to photo-bleaching of the fluorescent dyes,

such an experiment is however technically challenging. Therefore, this test is performed by simulation. In this simulation, distinct cell shapes, which have been recorded in previous fluorescence experiments are chosen, and the cells are randomly distributed on the simulated lattice. The proliferation of these cells is subsequently simulated by allowing for typical cell volume increase and cell division, again known from previous fluorescence measurements, as well as a randomly simulated movement of the cells. A detailed description of the simulation is provided in [150]. In the simulation, as in an experiment, single cells grow and divide over time to form a layer of cells that is closing up. As shown in the previous section, utilizing Equation 6.7 provides a means to predict the cell diffraction intensity from the simulated cell shapes of the cell ensemble. Figure 6.6 shows the correlation between the simulation according to Equation 6.7 and according to Equation 6.10. As in the proliferation experiments shown in Figure 6.4, the diffraction intensity first decreases and then increases again. The curve of the normalized inverse surface roughness of the cell ensemble $\frac{\bar{h}}{\sum_{n=1}^{N}|\nabla h_n(x,y)|}$ shows a reasonably good agreement with the normalized diffraction intensity as the coefficient of determination is $r^2 = 0.86$.
In addition to the simulation, the normalized inverse surface roughness is

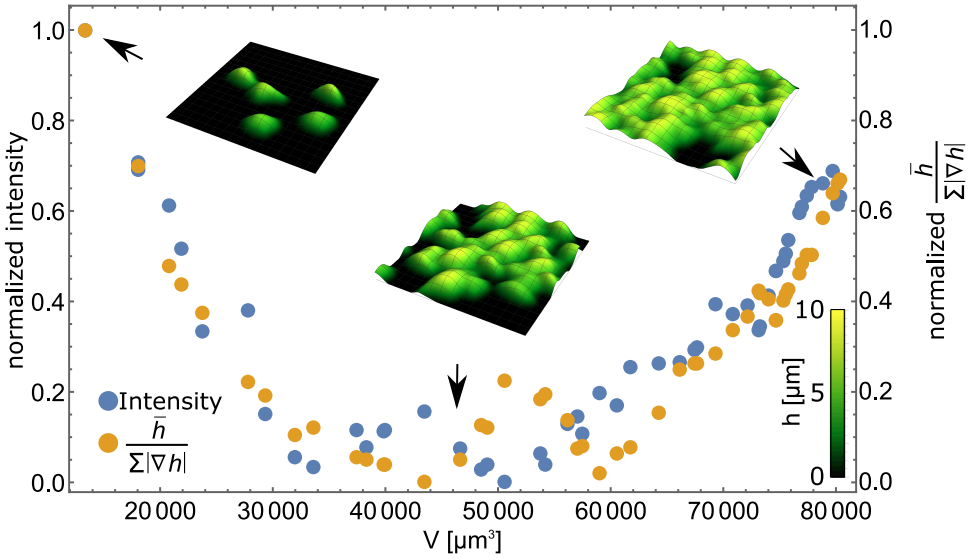

Figure 6.6: Simulation of cell proliferation. The diffraction intensity, calculated with Equation 6.7, and the inverse surface roughness, calculated with Equation 6.10, of a cell ensemble on a $(120 * 120)\,\mu m^2$ show a similar curve-behavior. Figure adapted from [150].

also calculated for the two measurements previously presented in Figure 6.3. These measurements do not comprise a whole proliferation experiment from a few single cells to a confluent ensemble, but only a shorter part of it. Hence, they do not show the characteristic proliferation curve. However, the derived relation still holds true reasonably well as can be seen in Figure 6.7. The correlation of the two curves yields a coefficient of determination of $r^2 = 0.86$ for Measurement 1 and $r^2 = 0.83$ for Measurement 2. The proportionality relation provided in this section therefore offers a reasonably

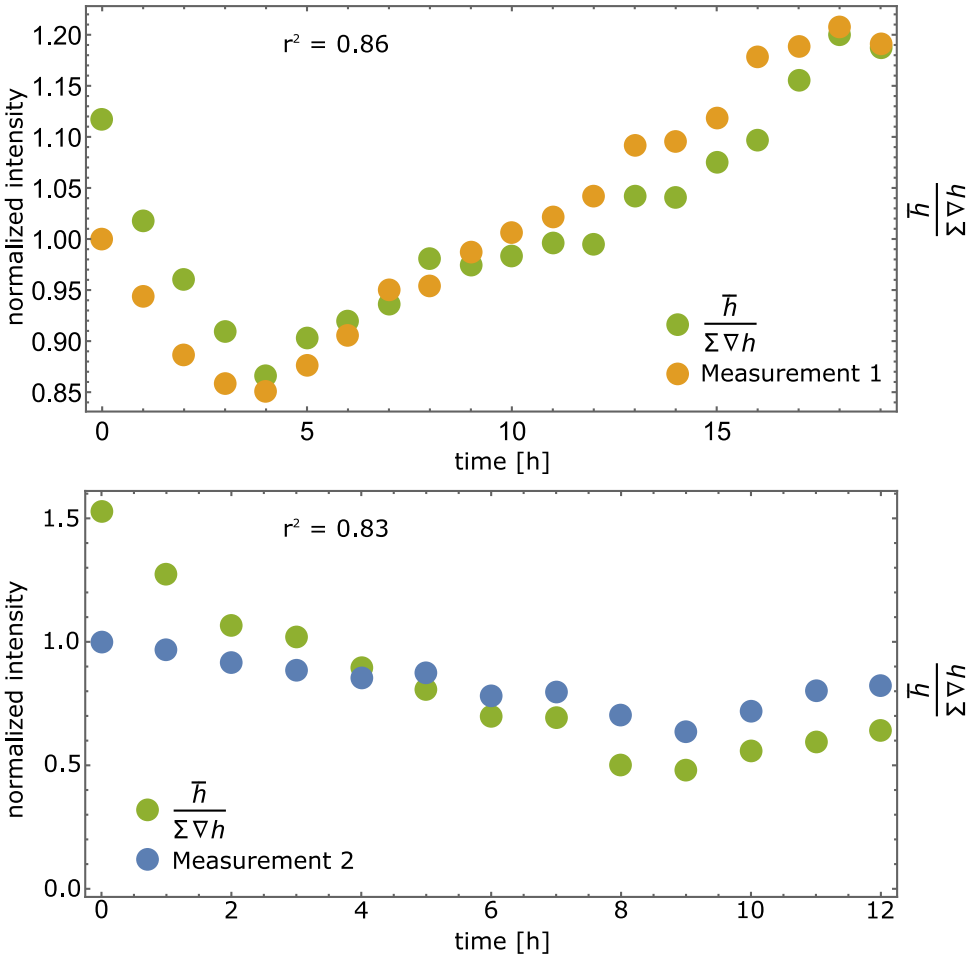

Figure 6.7: Measured diffraction intensity curve for two A549 cell ensembles and the corresponding normalized inverse surface roughness. The same scaling is used for both quantities.

accurate but much more intuitive understanding of the morphology and confluency of the measured cell ensemble from the measured diffraction intensity. It allows utilizing the intensity as an easy-to-use readout for key parameters of the cells. Therefore, in the following section, it is evaluated whether the diffraction method can be used for high throughput cell measurements based on an intensity readout.

6.4 DIFFRACTION-BASED DRUG SCREENING OF A459 AND PRIMARY CELLS

In this section, the diffraction method is used to probe dose-dependent cell ensemble responses to two different drugs. It is tested whether the drugs induce a morphological cell ensemble response that can be measured and resolved with the diffraction setup. The two utilized drugs are dimethyl sufloxide (DMSO) and cisplatin.

Dimethyl Sulfoxide

Dimethyl sufloxide (DMSO) is an organic solvent that is widely utilized in cell-based drug screening. It is often used as a solvent for drugs that do not dissolve well in water [153]. It also is employed in cryopreservation of cells, as it prevents the formation of ice crystals in the freezing process, which can lead to cell damage [154]. Studies show that in low concentrations and on short time scales, DMSO has no toxic effect on the cells [155, 156]. However, in this context, the definition of low concentrations varies from cell line to cell line. For neuronal cells, a DMSO concentration of 1 % was found to significantly inhibit cell viability [157, 158]. The same is reported for astrocytes, for DMSO concentrations higher than 5 % [159], while for enterocyte-like cells no cytotoxicity is found up to a concentration of 10 % [160]. Furthermore, DMSO has previously been employed as a morphology changing drug [161, 162]. In this section, it is investigated whether a dose-dependent cell morphology response of cell ensembles can be observed for two different cell lines with the diffraction setup.
For several non-small lung cancer cells such as *A*549 cells, it has been reported that DMSO changes the morphology of the cells and that a DMSO concentration of 5 % reduces cell viability to about 50 % [163]. Therefore, first *A*549 cells are exposed to DMSO, and the change in the diffraction intensity is analyzed. Figure 6.8 shows the signal change induced to a cell ensemble of *A*549 cells within 30 minutes. The characteristic signal change is induced by exchanging the cell-medium with a medium that is supplemented with 5 % DMSO. The sample is observed with the setup that is introduced at the beginning of Section 6.3. This allows a simultaneous recording of the diffraction intensity and the brightfield images of the cell ensemble on the diffraction grating to qualitatively observe cell morphology changes. As can be seen by the more pronounced edges in the inset images of the cell ensemble at various times, the DMSO causes the cells in the ensemble to round up gradually. Therefore, the overall cell curvature increases and thus according to Equation 6.10, the diffraction intensity decreases over time as is observed in the measurement. Note that the timescale of the DMSO experiments is much shorter than the one of the previously shown proliferation experiments since the cell morphology changes quicker.
To investigate whether a dose-dependence of the cell ensemble response to DMSO can be observed in A549 cells, the incubator setup introduced in Section 3.4 is utilized. In this setup, six different DMSO concentrations can be measured simultaneously in standard 6-channel slides. Figure 6.9 shows the cell ensemble response to DMSO concentrations between 0 % and 5 %. The confluency in each of the channels is constant at about 68 %. A clear dose-dependency can be observed as the characteristic intensity decrease over time increases with the DMSO concentration (see Figure 6.9 a)). To quantify the decrease of the diffraction intensity in a phenomenological

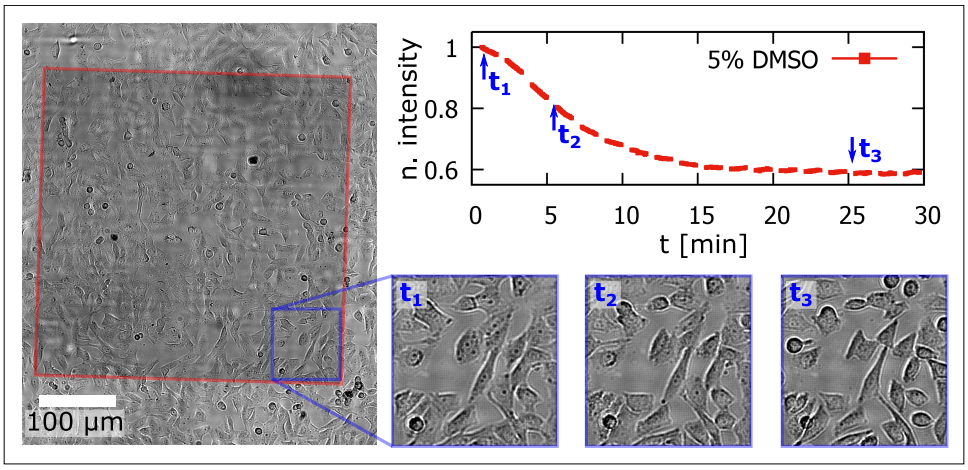

Figure 6.8: Diffraction intensity change due to changes induced to the *A*549 cells by addition of 5 % DMSO. The cell ensemble is seeded directly on the diffraction grating (red). The signal drop is due to the morphology change of the cells, as can be seen by the more pronounced edges of the cells at t_3.

way, a logistic function is fitted to the measured data.

$$f(t) = \frac{G}{1 + e^{-k \cdot (t - t_0)}} + 1 - G \tag{6.11}$$

Here, k characterizes the steepness of the curve, and G is the normalized intensity drop, which is the difference between the two plateaus of the function. When G is plotted against the DMSO concentration, as depicted in Figure 6.9 b), a linear dependency can be observed. This indicates that the cells morphology changes in a characteristic, dose-dependent manner when DMSO is added to the culture medium. This morphology change occurs almost instantaneous after the DMSO exposure and is completed within about 15 minutes.

In order to provide a critical discussion of these findings, an assessment of the possible methodical errors and of the accuracy of the method has to be made. As the cells also proliferate and migrate during a drug measurement, the diffraction intensity signal does not solely depend on the drug concentration but can be superimposed by these processes. In a typical proliferation experiment, the diffraction intensity can change up to 5 % within 30 minutes (see Figure 6.4). Thus, a noise of up to 5 % of the intensity signal is to be expected. Therefore, measuring DMSO concentrations below about 0.5 %, which cause signal drops smaller than 5 %, will be error-prone. Additionally, there is an upper boundary for the measurable DMSO concentration. By adding DMSO in concentrations higher than 10 % to the culture medium, turbulent mixing of the two fluids occurs. This mixing causes refractive index fluctuations in the DMSO-medium mixture that superimpose the cell-morphology-induced diffraction intensity changes and thus hinder their measurement.

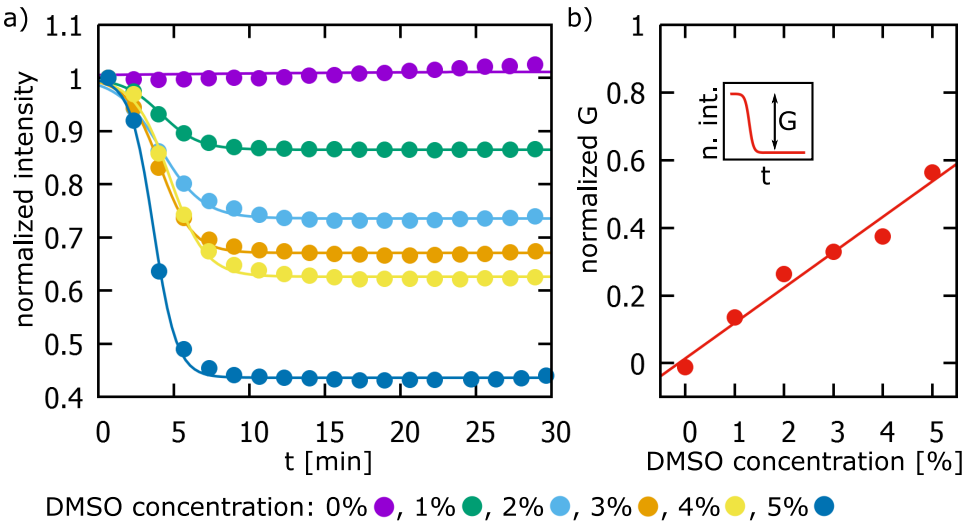

Figure 6.9: Dose-dependent diffraction intensity change to DMSO. a) Diffraction intensity change due to morphological changes induced to the *A*549 cell ensemble by addition of 0 % – 5 % DMSO. The induced signal drop is fitted with a logistic function. b) The signal drop *G* of the logistic fit function is plotted against the DMSO dose. A linear dependency can be observed.

Another source for errors are variations in the cell ensemble confluency between different measurements. As the cells are seeded and then adhere and grow in the channels, slight variations in the local confluency are unavoidable. For the measurements in this thesis, the confluency is determined with the holographic images of a CMOS sensor (see Section 3.4). The sensor is positioned next to the diffraction grating and the measurement slide can be moved to the sensor to provide an image of the exact area of the cell ensemble on top of the diffraction grating during a particular experiment. This method thus provides the means to determine the exact confluency of a cell ensemble on top of the diffraction grating. Variations in confluency of up to 10 % have been measured within single channels and also between the six different channels of one measurement slide, where a homogeneous confluency is expected.

As discussed above, the diffraction intensity depends on the confluency of the cell ensemble, and therefore the diffraction intensity change will also be influenced by the confluency. To analyze this confluency dependency, the DMSO measurement depicted in Figure 6.9 has been reproduced for five different confluencies. Figure 6.10 depicts the diffraction intensity change due to the addition of 5 % DMSO to the culture medium for each of these confluencies. The tested confluencies range from 25 % to 84 % and span the typical confluency range utilized in cell-culturing. The observed signal drop *G* due to the addition of 5 % DMSO increases with higher confluency. The signal drop is plotted against the confluency, and a linear relationship between confluency and *G* can be observed (see Figure 6.10 b)). This observation fits well with the intuitive understanding that in a more confluent cell layer with a proportionally higher cell number, the DMSO also causes

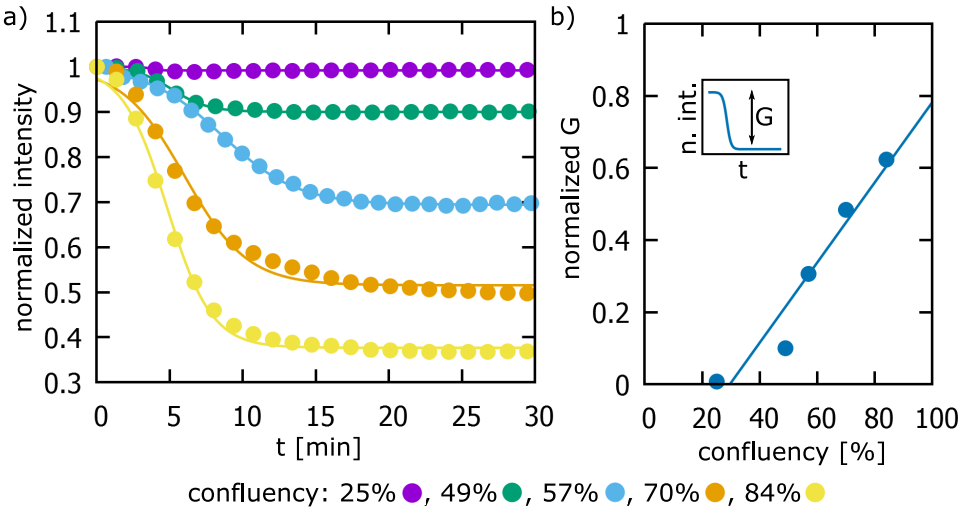

Figure 6.10: Confluency-dependent diffraction intensity change. a) Diffraction intensity course due to changes induced to the *A*549 cell ensemble by addition of 5 % DMSO for various confluencies. The induced signal drop is fitted with a logistic function. b) The signal drop *G* of the logistic fit function is plotted against the confluency. A linear dependency is indicated.

proportionally more cells to round up and thus decrease the diffraction intensity.

The observed confluency dependency illustrates the importance of a standardized and homogeneous cell seeding and thus a constant confluency in order to compare measurements. Furthermore, it shows that a higher measurement sensitivity can be expected for higher confluencies. Therefore, when applying the method as a drug screening assay, utilizing constant and high confluencies is beneficial.

To further investigate the dose-dependent morphology change induced to the cells by DMSO, the response of a second cell line is analyzed. To provide a contrast in the typical cell morphology and clustering in comparison to A549 cells, a primary human melanoma cell line is utilized. These cells do not form clusters like the A549 cells, but they maintain a very polarized and spread out cell shape (see Figure 6.11). Figure 6.12 shows the dose-dependent response of the primary cell line to DMSO concentrations of 0 % − 5 %. Here, the confluency of the cell ensemble is about 60% and therefore slightly below the one used for the A549 cells. However, the signal characteristic is the same as with the A549 cells, as the addition of increasing doses causes an increased signal drop. Again, there appears to be a linear relationship between the DMSO concentration and the signal drop. The normalized signal drop *G* of the 5 % DMSO measurement is about 0.4 and would fit surprisingly well into the linear confluency dependency of the A549 cells (see Figure 6.10). The main observable difference between the two cell lines is that the response time of the primary cells is faster, with the full signal drop occurring within about 3 minutes after the addition of DMSO. For the A549 cells, this response time is about 10 to 15 minutes. Since the initial cell shape of the primary cells is more spread out,

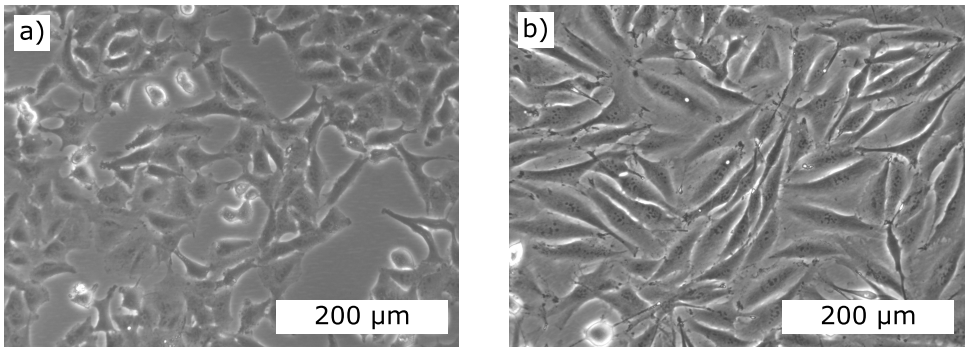

Figure 6.11: Phase-contrast microscopy images of cells with an objective magnification of 20 times. a) Cell culture of A549 cells. b) Cell culture of the utilized primary cell line. The primary cells show a more elongated and polarized cell shape in comparison to the A549 cells.

this more exposed and heterogeneous shape might be the reason for the faster response.
Together, the experiments in this subsection show that the introduced setup is able to measure drug-induced cell ensemble morphology responses and that the analyzed cell lines show a characteristic response in their morphology to DMSO. The response is dose-dependent but also confluency-dependent and cell-line-specific.

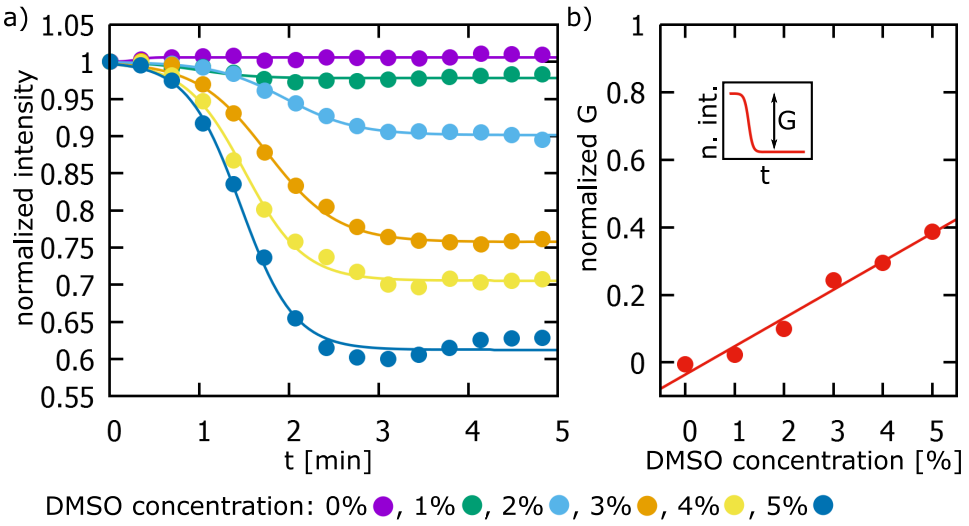

Figure 6.12: Dose-dependent diffraction intensity change to DMSO. a) Diffraction intensity change due to morphological changes induced to the cell ensemble of primary cells by addition of $0\,\% - 5\,\%$ DMSO. The induced signal drop is fitted with a logistic function. b) The signal drop G of the logistic fit function is plotted against the DMSO dose. Again, a linear dependency can be observed.

Cisplatin

The second drug investigated with the diffraction setup is *cis*-Diamminedichloroplatinum(II) (cisplatin). Cisplatin is used as a chemotherapeutic drug for the treatment of various types of cancers. It was first clinically introduced in 1978. Since then, the effects of the drug as well as its mechanism of action have been extensively studied *in vitro* [164]. Today, in non-small-cell lung cancer, the standard care procedure is to perform surgery followed by cisplatin-based chemotherapy [165, 166]. The mechanism of action of cisplatin is the following: It cross-links with DNA bases and interferes with the DNA repair mechanisms, thus damaging the DNA and inducing apoptosis in cancer cells [165]. Apoptosis is a cell program of controlled cell death that leads to morphological changes such as membrane budding and cell shrinkage [165]. Thus, cisplatin is chosen as a model drug as cisplatin-induced toxicity should provide a measurable signal in the diffraction setup.
Here, A549 cells, which are non-small lung cancer cells, are screened. They are cultured and seeded as described before (see Section 3.2). For the experiments, the cells are seeded in 6-channel μ-slides at a concentration of $3\,x\,10^5\,cells\,/\,ml$ and grown overnight, so they reach a confluency of about 70 % at the start of the measurement. Three 6-channel μ-slides are measured simultaneously, so 18 channels are analyzed in total. The cisplatin is normally dissolved in DMSO, but since DMSO can interfere with the cytotoxic properties of cisplatin [167], water is used instead. After overnight incubation, the growth medium in the culture dish is substituted with a preheated growth medium containing 1 % water with the final cisplatin concentration and the experiment is started immediately.
Experiments are conducted with the cells exposed to cisplatin concentrations of $0\,\mu M$, $5\,\mu M$, $10\,\mu M$, $20\,\mu M$, $40\,\mu M$, $80\,\mu M$ and $640\,\mu M$. The cell ensemble response to each concentration is measured in two different channels within one experiment, and the experiment is conducted three times. Figure 6.13 shows the averaged diffraction intensity signal over the six measurements at each concentration over 40 hours. In the control experiments, the intensity increases over time, as would be expected from the previous measurements with proliferating cell ensembles at high confluency (see Figure 6.8). The channels with a non-zero cisplatin concentration show a mostly monotonous decrease in the diffraction intensity over time, apart from a small increase at the start of the measurement in all but the highest cisplatin concentration measurements.[4] This decrease indicates morphological changes due to induced apoptosis. Figure 6.13 b) shows the dose dependency of the diffraction intensity decrease. Here, for simplicity, the signal drop G is defined as the normalized diffraction intensity difference between the start of the measurement and after 40 hours. The data points are plotted on a logarithmic x-axis, and a logistic fit is used, with the signal

4 One potential source for the increase in the intensity is a morphological response of the cells to the fresh culture medium or the addition of 1 % of water to the medium.

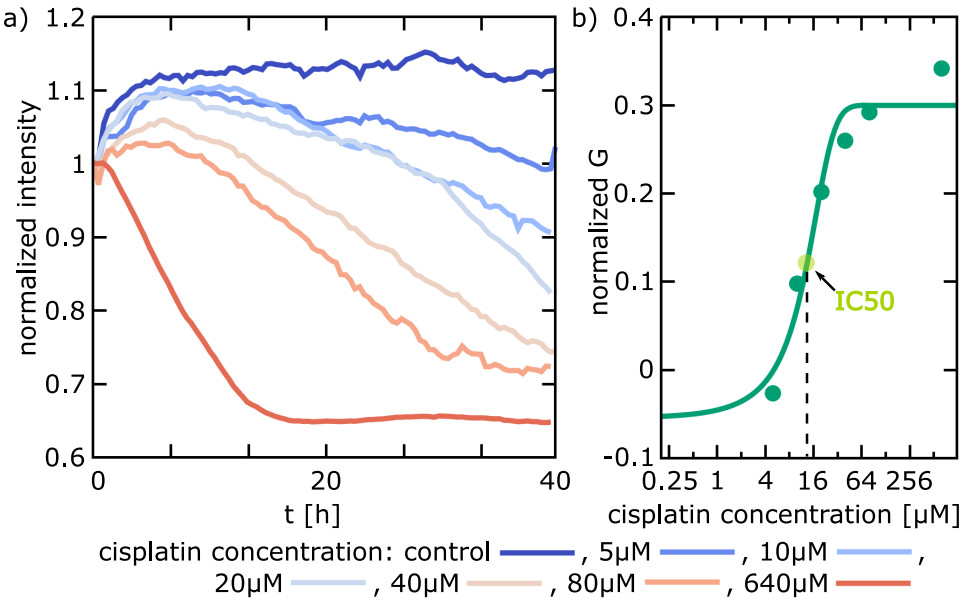

Figure 6.13: Dose-dependent diffraction intensity change of A549 cells due to cisplatin. a) Diffraction intensity course due to morphological changes induced to the cell ensemble of A549 cells by addition of various concentration of cisplatin. For each concentration, the average of six experiments is plotted. b) The normalized intensity change after 40 hours is plotted against the cisplatin concentration on a semi-logarithmic scale. A dose-dependent response is observed, as visualized by a logistic fit function, with the control serving as the offset of the function.

drop of the control serving as the offset of the logistic fit function.[5] Such a logistic fit is typically chosen to show the dose-dependent onset of drug response. It is used to assess the IC50 value of the chosen drug, which is defined as the drug concentration which causes 50 % of the maximum drug response [168]. Here, it is found that the IC50 value for cisplatin on A549 cells is about 10 μM.

The results that are presented here are in good agreement with literature findings. It has been shown previously that cell death occurs with a typical response time of 8 - 11 hours after cisplatin addition [164]. This is in agreement with the presented data, apart from the 640 μM concentration, which however is a concentration far from the IC50 value and has thus not been tested in the quoted reference. Furthermore, the dose-dependent response of A549 cells to cisplatin has been investigated before with the help of an MTT assay [169]. After 48 hours the viability of cells exposed to over 4 μM of cisplatin was found to be significantly reduced compared to lower concentrations. This differs in about a factor of two from the IC50 value obtained here. One possible source for this difference is a confluency dependent resistance of A549 cells to cisplatin [170]. The confluency of the cells, which is not indicated in the quoted publication, possibly differs from the confluency used here and thus might cause different drug-dependent

5 Thereby the control experiment defines the lower boundary of the logistic function.

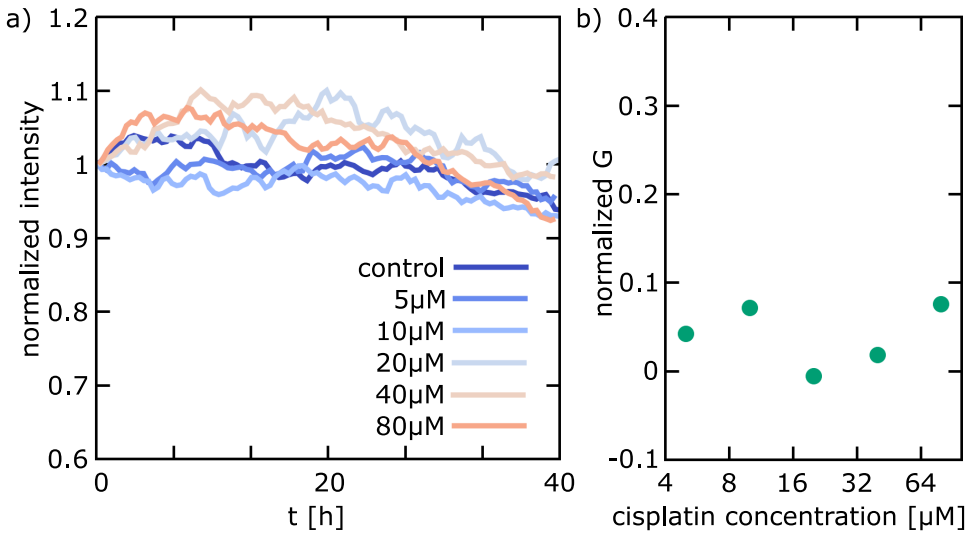

Figure 6.14: Diffraction intensity change of cisplatin-resistant MDA-MB-231 cells due to various doses of cisplatin. a) Diffraction intensity course induced to the cell ensemble of MDA-MB-231 cells by addition of various concentration of cisplatin. For each concentration, the average of three experiments is plotted. b) The normalized intensity change after 40 hours is plotted against the cisplatin concentration on a semi-logarithmic scale. No dose-dependent response is observed.

cell viability. By probing the drug-response under different confluencies, the diffraction setup could in the future be used to investigate confluency dependent resistance. The results presented here are of comparable quality and sensitivity to the results obtained with impedance-based techniques. While the impedance readout has been analyzed for different cell lines, these cell lines show similar response curves over 40 hours over a comparable range of cisplatin concentrations [164, 171].

For further validation, the response of cell ensembles of the human-breast-adenocarcinoma cell line MDA-MB-231 to cisplatin is tested. This cell line is resistant to cisplatin [164, 172], and should, therefore, show no dose-dependent response to different cisplatin concentrations in the diffraction setup. The experiment is conducted analogously to the experiment with A549 cells. Figure 6.14 a) depicts the cell ensemble response to cisplatin concentrations ranging from $0 - 80\,\mu M$ over 40 hours. For comparison, both axes are plotted in the same value-range as in Figure 6.13. In contrast to the A549 cells, the MDA-MB-231 cells do not exhibit a dose-dependent intensity drop over time. The intensity differences between the various cisplatin concentrations of the MDA-MB-231 cells are within typical cell-proliferation- and confluency- variations, as discussed above. In Figure 6.14 b), no dose-dependent onset of drug response is observable. These results support the claim that the MDA-MB-231 is resistant to cisplatin.

Together, these findings show that the diffraction setup can measure the

drug response of cell ensembles to cisplatin in the same time frame and with comparable signal stability as impedance-based techniques.

7 DIFFRACTION ANALYSIS OF 3D CELL CULTURE

7.1 THE NEED FOR 3D CELL CULTURE ASSAYS

In vitro cell-based assays, especially with regard to drug screening and drug discovery, are widely used in research and medicine. Such experiments provide a cheap and efficient means to study drug response in a high throughput manner in preclinical studies and in clinical trials before turning to more large-scale and costly animal studies. However, despite the widespread use of cell-based assays, it has been reported that the rate of successful translation of findings from preclinical research into approved drugs is low [173, 174]. One possible source for the low translation rate is the fact that the 2D cell culture does not adequately mimic the *in vivo* 3D environment of the cells, and thus produces misleading results. As a result, it has been suggested that 3D cell culture could provide a more natural environment and thus could lead to more accurate and predictive data for clinical trials. It has since been shown that cell responses in 3D culture can provide a better prediction for *in vivo* responses in animal testing than cell responses measured in 2D culture [175].

There are two main methods, to culture cells in 3D. The first is to culture the cells in 3D spheroids, which are clusters of cells that are typically embedded into a spheroidal substrate after seeding [176, 177]. This method provides cell clusters with cells in various states dependent on their location within the spheroid [178, 179], which mimics tumors particularly well [174]. However, for drug screening, the disadvantage of this approach is that the drug response from the cells in the different states can also be cell state dependent and heterogeneous. The second method is to embed the cells into a bio-compatible 3D matrix of polymers such as hydrogels [174, 180, 181]. In this method, cell-cell contacts are rare since the cells are randomly distributed within the hydrogel.[1] The advantage of this method is that due to the porous matrix, the cells are evenly supplied with oxygen, nutrients and drug molecules [182]. Additionally, the hydrogels can be designed with mesh-sizes on different length-scales or matrix-elements that are cleavable by the cells [79]. This allows for cell migration and proliferation and mimics the extracellular matrix well.

Both spheroids [176, 183, 184] and hydrogels [184] have been successfully applied as assays for bio-sensing. The most commonly utilized assays in this field are impedance-based assays that employ hydrogels [174, 185–187]. Impedance-based techniques can provide ensemble signals, which are independent of the localization of the cells within the hydrogel. However, until now, these techniques all rely on self-built setups, that are not com-

1 The random distribution of the cells occurs due to hydrogel fabrication process from the liquid form (see Section 3.5).

mercially available and use self-built sample chambers [180, 183, 185, 188]. This does hamper the reproducibility of the results and the comparability between different cell lines or drugs by other researchers [173]. Therefore, a technique that does not rely on specific impedance-measurement-enabling substrates, sample holders and setups, but instead can operate with standard lab-ware and offers a signal that is not affected by the localization of the cells within the hydrogel is of great interest. It further is desirable for the technique to enable a comparison between the drug response of cell ensembles in 2D monolayers and in 3D hydrogels, as this comparison can help to analyze the feasibility of 2D assays as viable *in vitro* models for individual research questions.
In the following section, the diffraction method is employed to measure drug responses of cell ensembles in 3D hydrogels as a proof of principle.

7.2 DIFFRACTION-BASED DRUG SCREENING IN 3D HYDROGELS

In this section, the A549 drug-screening and proliferation experiments, which have been presented in the last chapter for 2D cell ensembles, are repeated for cell ensembles in 3D hydrogels. For these experiments, the cells are not seeded onto a substrate, but the cell suspension is dissolved in a pre-polymer solution, which is then polymerized to a hydrogel by UV-illumination. All the components, and the process of the hydrogel fabrication are presented in Section 3.5. The resulting hydrogel covers the horizontally UV-illuminated area and ranges vertically from the bottom of the channel to the top of the channel. It has a mesh-size that is three orders of magnitude smaller than the cells but can be cleaved by the cells. Hence, the hydrogel offers an artificial extracellular matrix for the cells and at the same time allows the cells to migrate and proliferate. The hydrogels are polymerized in the same 6-channel µ-slides that were used in the 2D experiments. Furthermore, the diffraction setup is kept in the same configuration, which enables to compare the drug screening experiments in 2D (see Chapter 6) with the 3D experiments.
To measure the intensity of a diffraction peak through a hydrogel, the adjustment between the diffraction grid and the position of the hydrogel on top of the grid has to be very precise, as these two components are in the same order of magnitude. This is visualized in Figure 7.1. Here, the grid size is visualized by the green square. Multiple positions, where a stable diffraction signal is measurable, are marked. Such a stable diffraction peak occurs when the diffraction grid is either completely under the hydrogel or completely next to the hydrogel. In the areas where the diffraction grid would be only partially beneath the hydrogel, there is no distinct and stable diffraction peak due to scattering at the hydrogel. This is also true for areas that are only partially beneath the channel.
Note that in this configuration, a 2D and 3D experiment can be performed in parallel in the same channel in the future. However, this requires for cells to be seeded in the channel after the polymerization of the hydrogel. While such a combination is undoubtedly desirable for future experiments,

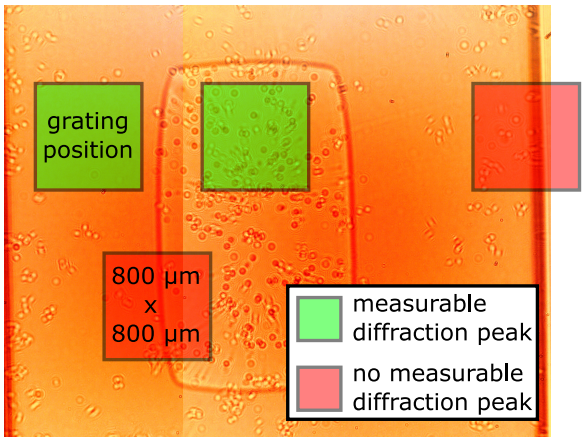

Figure 7.1: Image of a hydrogel within a channel of a 6-channel μ-slide. The image is stitched from two CMOS sensor images. The squares indicate possible positions of the diffraction grating underneath the channel, while the colors indicate whether or not a diffraction peak is measurable. The green squares highlight exemplary position, where the diffraction grating can be placed for measurement, either underneath the hydrogel or next to the hydrogel for reference. The red squares show exemplary positions, where a diffraction measurement would not be possible due to refraction either at the hydrogel border or at the channel border.

it requires to timely coordinate the confluency of the cells in the 2D monolayer and the cell density within the hydrogel to be ready for the start of the experiment at the same time. Furthermore, the cells in the monolayer can invade the hydrogel and cleave it at the edges, leading to a faster hydrogel degradation. For these reasons, and since this chapter should act as proof of principle, the 3D hydrogel results are compared to the previously made experiments in Chapter 6.

Proliferation in 3D Hydrogels

Figure 7.2 depicts the diffraction intensity over time for three different A549 cell ensembles in 3D hydrogels. As the cells proliferate, the diffraction intensity decreases over time. This is consistent with the diffraction theory, as more cells cause higher optical disturbance and a higher inhomogeneity in the optical path length of different light rays. In comparison to the 2D proliferation experiment, depicted in Figure 6.4, there is no increase in the diffraction intensity at the end of the measurement. In the 2D monolayer, such an increase could be attributed to the closing of the cell layer, which causes a more homogeneous layer than single cells. This in turn contributed to lower optical disturbance of the grating. In 3D, however, the cell ensemble does not form a single layer. Instead, the cells are still able to proliferate into the third dimension. An increase is only expected when the cells begin to fill up the hydrogel entirely in three dimensions. Experimental observation of this process is challenging though, as the cells cleave

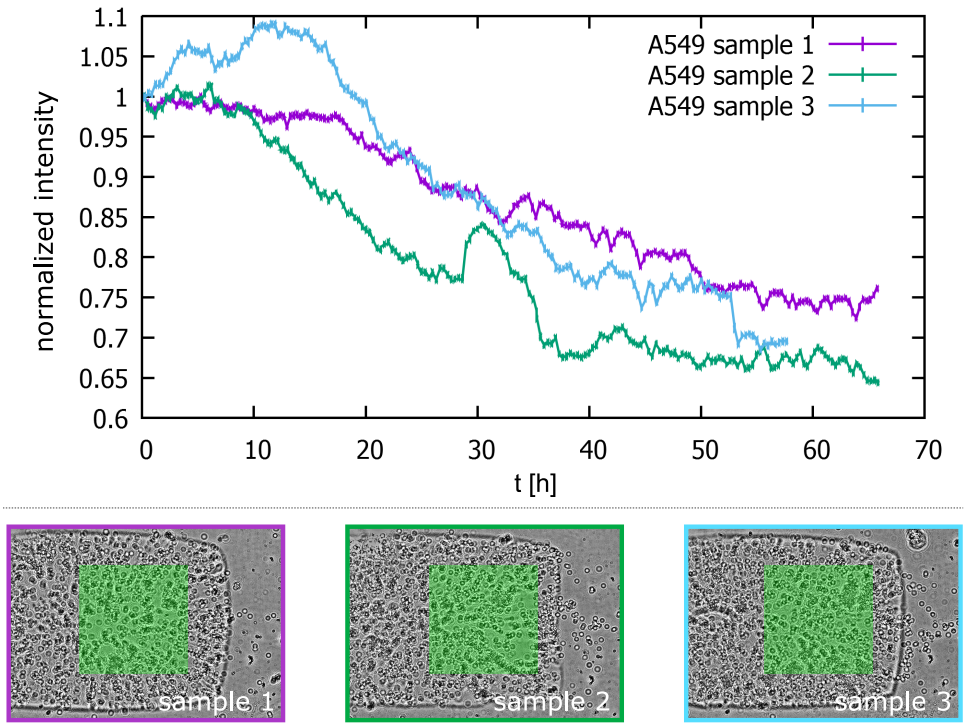

Figure 7.2: Normalized diffraction intensity plotted over time for three proliferating cell ensembles in 3D hydrogels. The characteristic intensity decrease due to proliferation is consistent with the 2D results. In the bottom panel, images of the corresponding cell ensembles, which are recorded with a CMOS sensor at the start of the experiment, show the position of the $800\,\mu m\,x\,800\,\mu m$ diffraction grating underneath the sample (light green).

and hence degrade the hydrogel over time.

Dose-Dependent Cell Response to DMSO

In Figure 7.3 a), the response of cell ensembles of A549 cells in 3D hydrogels to concentrations of $0\,\% - 5\,\%$ DMSO is shown. The characteristic signal drop that has been observed in the 2D experiments (see Figure 6.9) is reproduced in the 3D hydrogel experiments. When plotting the normalized signal drop G after 30 minutes (see Figure 7.3 b)), again a linear relationship between the signal drop and the DMSO-dose is observed. Compared to the 2D measurements, G is smaller in the 3D measurement for each DMSO concentration. Additionally, the dose-dependency is lower.[2] These differences can be attributed to a systematic discrepancies. It has been shown in the previous chapter that the intensity decrease is confluency dependent. This dependency is also true when comparing 2D and 3D measurements. In 3D though, the confluency is not a useful measure,

2 Here, the slope of the linear fit is synonymous with the dose-dependency.

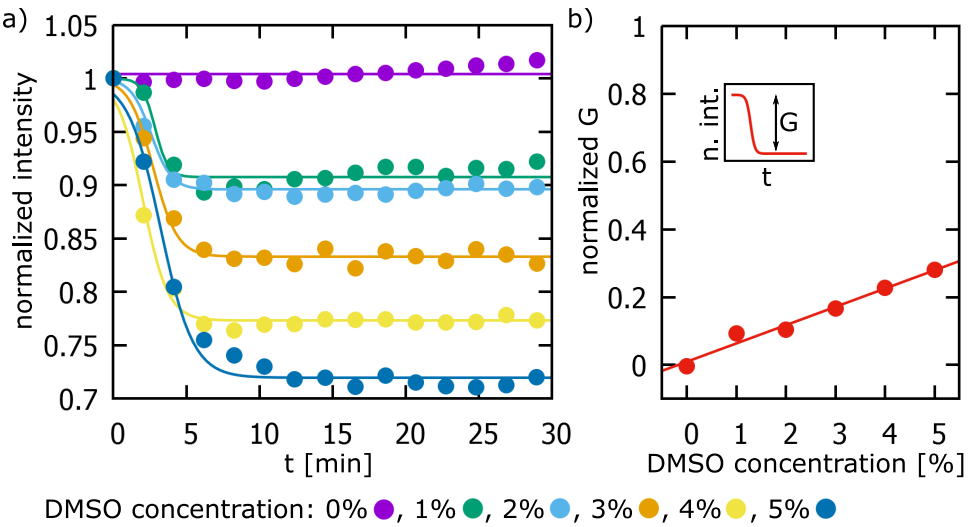

Figure 7.3: Dose-dependent diffraction intensity change of A549 cells in 3D hydrogels to DMSO. a) Diffraction intensity change due to morphological changes induced to the *A*549 cell ensemble in a hydrogel by addition of 0 % − 5 % DMSO. The induced signal drop is fitted with a logistic function. b) The signal drop G of the logistic fit function is plotted against the DMSO dose. A linear dependency can be observed.

as cells can grow on top of each other. Therefore, the overall cell number above the diffraction grating should be used as a measure to characterize the dependency when comparing 2D results with 3D results and hence should be kept about constant.

Dose-Dependent Cell Response to Cisplatin

The screening of A549 cells with different concentrations of cisplatin, which has been performed in 2D culture in Section 6.4 is repeated here for 3D hydrogels. The diffraction intensity over time is plotted in Figure 7.4 a). Fundamental differences occur in comparison to the 2D time evolution, shown in Figure 6.13 a). For the 2D culture, a dose-dependent onset of cisplatin-induced cell death occurs, which is characterized by an increase in the signal drop with higher cisplatin concentrations. Such behavior is not observed in the 3D hydrogels. Instead, while a dose-dependent behavior can be seen, this behavior is inverted in the shown 3D experiment. In order to explain this difference, the control measurement without any cisplatin can act as a reference. In the 3D hydrogel measurement, this reference plot is similar to the results of the proliferation experiment, which is shown in Figure 7.2. It can be assumed that the induced intensity change over time in the reference arises due to cell proliferation. As higher cisplatin concentrations show a smaller intensity drop and even an intensity increase for concentrations above $10\,\mu M$, this indicates that the cells in these cell ensembles did not proliferate like the cells in the control experiment. In

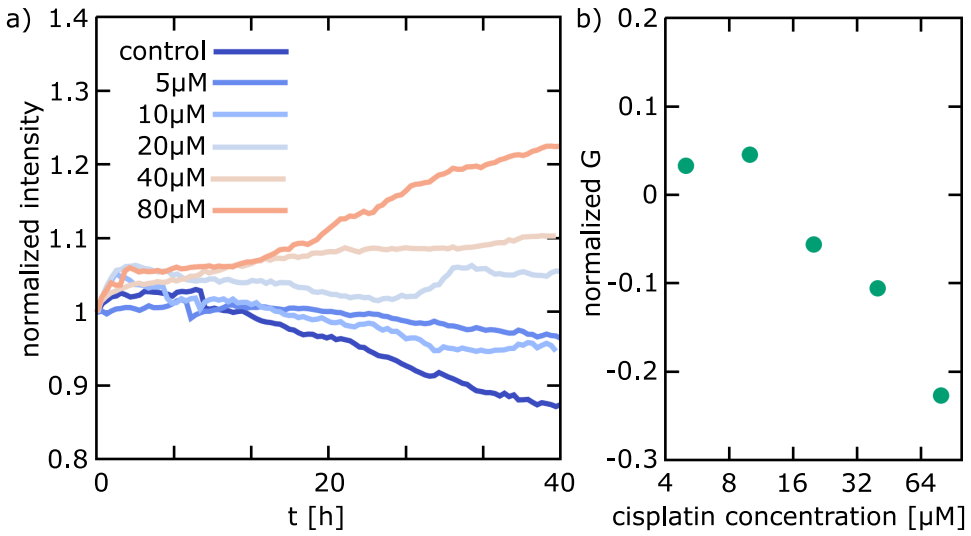

Figure 7.4: Dose-dependent diffraction intensity change of A549 cells in a 3D hydrogel due to cisplatin. a) Diffraction intensity course due to morphological changes induced to the cell ensemble of A549 cells by addition of various concentrations of cisplatin. For each concentration, the average of two experiments is plotted. b) The normalized intensity-change after 40 hours is plotted against the cisplatin concentration on a semi-logarithmic scale.

the Appendix A.7, two images of the cell ensembles after the measurement are depicted, which support this claim. A lack of proliferation, which is induced by cisplatin could hence explain the inverted behavior. However, this would also indicate that in the 3D experiment the intensity change is dominated by cell proliferation, while in 2D the rounding of the cells due to induced apoptosis dominates the intensity change. Furthermore, this difference can not solely explain an intensity increase over time. Therefore, a comparison between 2D and 3D cisplatin experiments should only be made after validation of the measured behavior and further testing.

2D/3D Comparability-Assessment

The three experiments performed in this chapter, show that several issues need to be addressed to provide a quantitative comparison between cell cultures in 2D monolayers and in 3D hydrogels.
First, in order to compare proliferation in 2D and in 3D, the cell ensembles above the diffraction grating have to have a similar number of cells at the start of the experiment. This can be achieved by moving away from the confluency as a measure of cell amount in 2D and by performing accurate counting.
With the DMSO experiments, it has been shown that the dose-dependency of A549 cells can be qualitatively reproduced in 3D hydrogels. For a quantitative assessment, again, the number of cells has to kept constant.

One parameter that is not impaired by the systematic differences between the 2D and 3D measurements is the time dependence of the drug-induced intensity change. Therefore, differences in the time-dependent response to a drug between 2D monolayers and 3D hydrogels can be readily tested with the presented method.
Additionally, the dose-dependent onset of a drug as e.g. seen in the cisplatin experiments can be compared between 2D and 3D cultures. For the cisplatin experiment, a quantitative comparison is omitted here, as the intensity change in the 3D measurement is assumed to be dominated by cell proliferation (see above). For drugs that act on shorter time scales however, it can be readily tested whether the IC50 value changes when moving to 3D cultures. Such research questions can provide viable insight for creating better *in vitro* models.
Together, the results presented in this chapter provide a proof of principle for drug screening in 3D hydrogels with the diffraction method. It was demonstrates that the diffraction method can provide an assay for 3D culture that utilizes only standard lab-ware. The method can further allow comparing results of 2D monolayers with 3D hydrogels within one measurement if the key points stated above are properly addressed.

Part IV

CONCLUSION

8

SUMMARY AND OUTLOOK

In this thesis, periodic nanostructures were employed as optical imaging- and diffraction-sensors in cell-based research. The introduced methods and the subsequent results were presented in two distinct parts: the image-based detection and the diffraction-based detection.

In the image-based detection, it was first discussed how distortions and image aberrations in general could limit the accuracy of localization methods, when imaging through biological specimens. It was proposed that a grid of periodic gold nanostructures could act as a reference specimen to detect such image distortions. A distortion quantification had not yet been performed for single cells, as the distortions were expected to be small.
Here, this work was able to obtain two key insights. First, a precise quantification of the optical distortion field induced by single adherent cells, could be provided with nanometer scale accuracy. In contrast to common assumptions, distortions of up to $400\,nm$ were found, which in turn significantly impair the accuracy of localization techniques. The second key insight is the derivation of a geometrical optics relation that connects the 3D cell shape with the optical distortions. This relation allows correcting the measured image distortions by measuring the 3D cell shape. It offers an easily implementable way to reduce distortions in single-cell images by a factor of three, and can hence improve localization accuracy in traction-force and fluorescence localization microscopy. Conversely, the derived relation was utilized to reconstruct the 3D cell shape from the distortion data, allowing quantitative 3D shape information to be acquired from a single 2D image. This in turn provides a fast, label-free method that can record the 3D cell shape and volume over time and is capable of resolving rapid changes. Figure 8.1 illustrates the utility of the derived relation.

In the second results-part of this thesis, which investigates the diffraction-based detection, the introduced nano-structured grid was utilized as a diffraction grating.
A diffraction setup was built and subsequently tested. This setup utilizes a laser to illuminate the nano-structured grating and records the intensity of a diffraction peak. It was theoretically and experimentally shown that cells on top of the diffraction grating change the diffraction peak intensity and that from the induced change, conclusions about the morphology of the cell ensemble on top of the grating can be made.
In drug screening, cell-based assays are utilized to study cytotoxicity. Common limitations of such assays are the need for labels or specialized culture dishes as well as the fact that they often only provide a single endpoint readout. Here, it was shown that the diffraction method could provide an

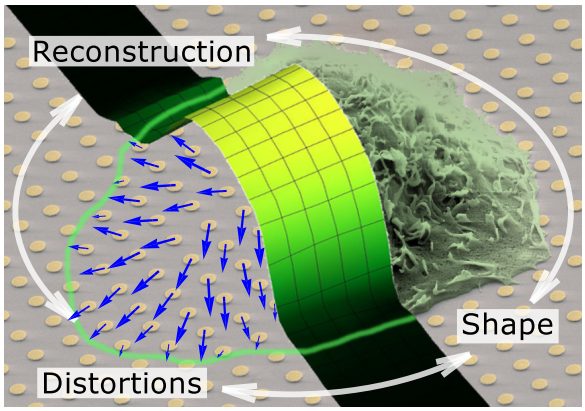

Figure 8.1: Collage to illustrate the utility provided by the derived geometrical optics relation. The relation enables a distortion correction for localization methods by measuring the 3D cell shape, e.g. with fluorescence microscopy. Conversely, the relation can be also employed to reconstruct the 3D shape of an adherent cell from a single 2D image without the need for labels. Reprinted with permission from Nano Letters, 2017, 17 (12), pp 8018–8023. Copyright 2017 American Chemical Society.

assay without these limitations. A cell-line-dependent and dose-dependent response to DMSO could be measured with the assay. Furthermore, a dose-dependent response to cisplatin was recorded for A549 cells while the cisplatin-resistant cell line MDA-MB-231 showed no morphological response to cisplatin.
Furthermore, the diffraction method was utilized in a proof of principle to screen cells in 3D hydrogels, using the same type of culture dishes.

Together, these findings highlight the potential that lies in utilizing nanostructures in cell-based research. In the future, all methods that were presented in this thesis can be improved upon.
The distortion quantification can be advanced in resolution and accuracy by employing densely spaced point emitters, e.g. through single-molecule nano-patterning [189]. This would open up the possibility for label-free, high-resolution, cell morphology or surface roughness measurements or investigation of smaller prokaryotic cells. Reconstruction and distortion quantification applications are furthermore not limited to single cells but can also be envisioned in the broader context of reconstruction and characterization of transparent 3D objects like micro-lenses or 3D gels. Additionally, the nanostructures could not only be used as optical references, but also as adhesion points of the cells on a passivated surface or within a microstructure confinement [113]. By employing a gradient in the distance between the nanostructure, such a system could provide spatial guiding for cell migration as well as an optical reference for 3D cell shape reconstruction.
In order to utilize the advantages of the diffraction setup as a label-free assay for drug screening in the future, systematic improvements can be made. First, larger diffraction gratings together with an expansion of the

laser beam diameter can be utilized to screen larger cell ensembles and thus provide a greater statistical relevance. Second, the high throughput capabilities, which are at the moment limited to 24 samples per measurement can be expanded by an improved sample-holder or smaller channels. With these improvements, the setup can be employed as an assay for high throughput screening of cell-line-dependent and dose-dependent drug responses as well as to screen for, e.g. confluency dependent resistance [170].
In order to establish the diffraction method also for 3D hydrogels, the derived diffraction model with a 2D cell layer should be expanded to 3D cell culture and the experimental results should be validated using this expanded model.
In the future, the diffraction method could additionally provide an opportunity to compare cell-responses within the two frameworks of 2D and 3D cell cultures, without the bias introduced by working with different setups. Such an assay would allow to assess whether 3D cell culture can bridge the gap between *in vitro* and *in vivo* studies.

APPENDIX

A.1 DERIVATION OF THE GEOMETRICAL OPTICS MODEL EQUATION

In Figure A.1, the refraction at the cell/medium interface, obtained using the approximations introduced in Section 4.4, is depicted in 2D. The main equation for the correction (see Equation 4.1) is derived as follows. Since the displacement D is perpendicular to the cell height h, by using the trigonometric function to one obtains:

$$D = \tan(\gamma) \cdot h \tag{A.1}$$

Since $\alpha = \beta + \gamma$ (see Figure A.1), this can be written as:

$$D = \tan(\alpha - \beta) \cdot h \tag{A.2}$$

Here, Snell´s law for the refraction between two surfaces can be written as:

$$\sin(\alpha) \cdot n_{Medium} = \sin(\beta) \cdot n_{Cell} \tag{A.3}$$

Rewriting for β gives:

$$\sin(\beta) = \sin(\alpha) \cdot \frac{n_{Medium}}{n_{Cell}} \tag{A.4}$$

$$\beta = \sin^{-1}\left(\sin(\alpha) \cdot \frac{n_{Medium}}{n_{Cell}}\right) \tag{A.5}$$

Now, inserting Equation A.5 into Equation A.2, one obtains:

$$D = \tan\left(\alpha - \left(\sin^{-1}\left(\sin(\alpha) \cdot \frac{n_{Medium}}{n_{Cell}}\right)\right)\right) \cdot h \tag{A.6}$$

Since h is orthogonal to D, the angle α corresponds to the angle between the tangent of the cell at the position of the refraction and the surface:

$$\frac{\mathrm{d}h}{\mathrm{d}x} = \tan(\alpha) \tag{A.7}$$

Rewriting for α gives:

$$\alpha = \tan^{-1}\left(\frac{\mathrm{d}h}{\mathrm{d}x}\right) \tag{A.8}$$

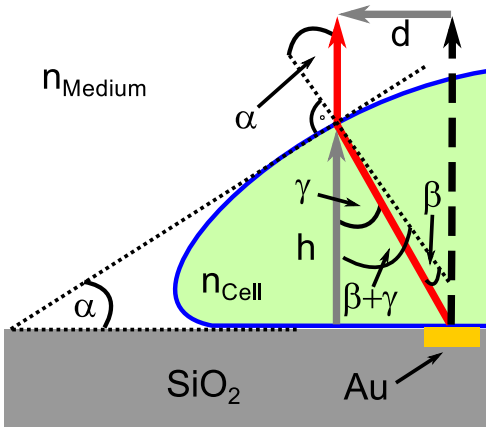

Figure A.1: 2D schematic of the refraction at the cell surface for a cell with constant refractive index. Reprinted with permission from Nano Letters, 2017, 17 (12), pp 8018–8023. Copyright 2017 American Chemical Society.

Inserting Equation A.8 into Equation A.6, we get Equation A.9:

$$D = \tan\left(\tan^{-1}\left(\frac{\mathrm{d}h}{\mathrm{d}x}\right) - \left(\sin^{-1}\left(\sin\left(\tan^{-1}\left(\frac{\mathrm{d}h}{\mathrm{d}x}\right)\right) \cdot \frac{n_{Medium}}{n_{Cell}}\right)\right)\right) \cdot h \tag{A.9}$$

Using $D = d$ finally yields Equation 4.1 (with $n_1 = n_{Medium}$ and $n_2 = n_{Cell}$):

$$\begin{aligned} d_x(x,y) = \tan\Bigg(&-\sin^{-1}\left(\sin\left(\tan^{-1}\left(\frac{\mathrm{d}h(x,y)}{\mathrm{d}x}\right)\right) \cdot \frac{n_{Medium}}{n_{Cell}}\right) \\ &+ \tan^{-1}\left(\frac{\mathrm{d}h(x,y)}{\mathrm{d}x}\right)\Bigg) * h(x,y) \end{aligned} \tag{A.10}$$

An analogous procedure for the y-direction yields the equation for the distortion vector:

$$\begin{aligned} d_y(x,y) = \tan\Bigg(&-\sin^{-1}\left(\sin\left(\tan^{-1}\left(\frac{\mathrm{d}h(x,y)}{\mathrm{d}y}\right)\right) \cdot \frac{n_{Medium}}{n_{Cell}}\right) \\ &+ \tan^{-1}\left(\frac{\mathrm{d}h(x,y)}{\mathrm{d}y}\right)\Bigg) * h(x,y) \end{aligned} \tag{A.11}$$

$$\vec{d}(x,y) = \begin{pmatrix} d_x(x,y) \\ d_y(x,y) \end{pmatrix} \tag{A.12}$$

A.2 QUALITY OF IMAGE DISTORTION CORRECTION

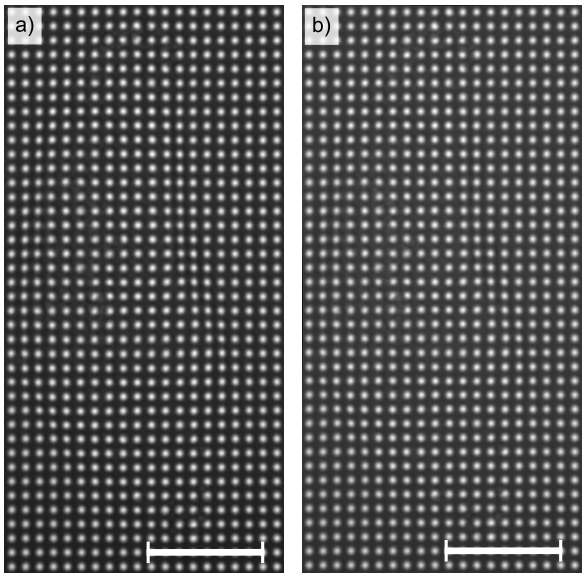

Figure A.2: a) Original, distorted image. b) Corrected image. Scale bars: 10 μm. Reprinted with permission from Nano Letters, 2017, 17 (12), pp 8018–8023. Copyright 2017 American Chemical Society.

To quantify the quality of the correction, one can consider the absolute change in distortion vector length at each structure (see Figure A.3 a)). In the area of the cell, very few structures show slightly larger distortions following the correction (red), while the majority of structure distortions are significantly reduced (green). This analysis does not distinguish between over- and under-corrected areas, which is why the angle φ between the corrected and the measured distortion vector is additionally investigated at each structure (see Figure A.3 b)). Under-corrected areas are defined as areas where the vectors before and after correction are pointing in the same direction ($|\varphi| < 90°$), whereas in over-corrected areas they point in opposite directions ($|\varphi| > 90°$). The border regions of the cell tend to be slightly under-corrected, as shown by the light colors corresponding to $|\varphi| < 90°$. One can assume that this is caused by a change in cell shape between the recording of the distorted image and the confocal measurement. Figure 4.7 e) combines Figure A.3 a) and b), omitting two different colors for the length correction by setting: $d_\varphi = ||\vec{d}_m| - |\vec{d}_c|| = |\Delta d|$.

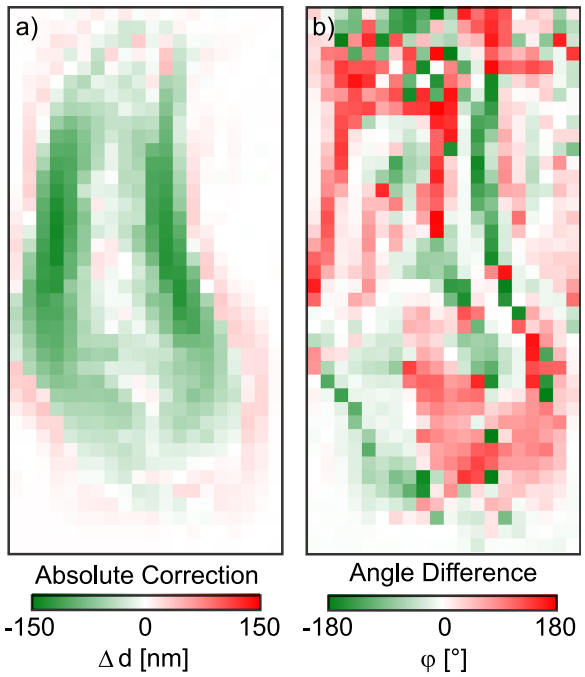

Figure A.3: a) Difference between the absolute vector lengths in the distorted and corrected image at each structure. b) Angular difference between the vectors in the distorted and corrected images at each structure. Reprinted with permission from Nano Letters, 2017, 17 (12), pp 8018–8023. Copyright 2017 American Chemical Society.

A.3 COMPARISON OF 3D CELL SHAPE FROM RECONSTRUCTION AND FROM CONFOCAL DATA

The reconstructed cell shapes are in good agreement with those measured by confocal microscopy, as shown in Figure A.4. The cell volume is calculated by interpolating the cell shape and integrating over the cell area, and shows only a 3% difference between the two measurements.

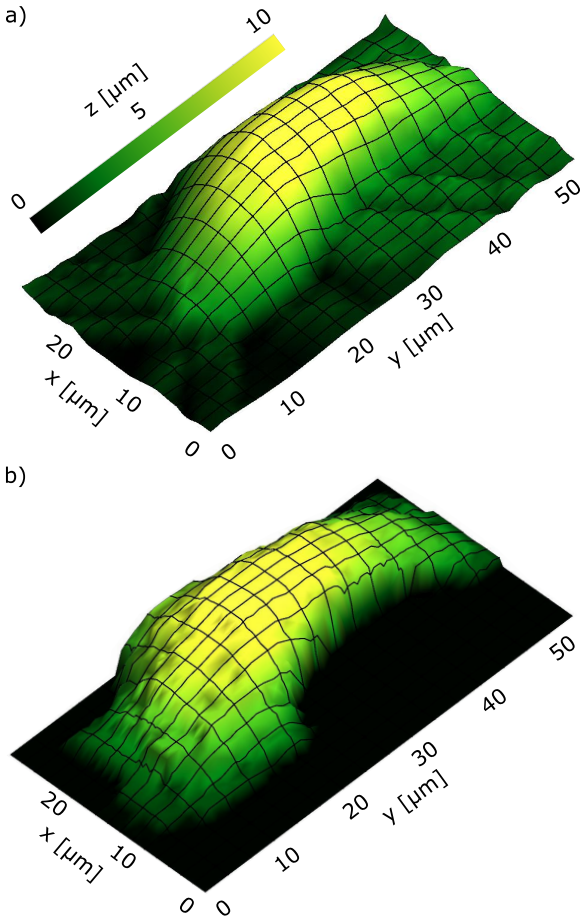

Figure A.4: a) Cell shape reconstructed from the distortion data. The background noise arises from the discrete data points. b) Cell shape measured by confocal microscopy. Reprinted with permission from Nano Letters, 2017, 17 (12), pp 8018–8023. Copyright 2017 American Chemical Society.

A.4 TIME LAPSE 3D RECONSTRUCTION

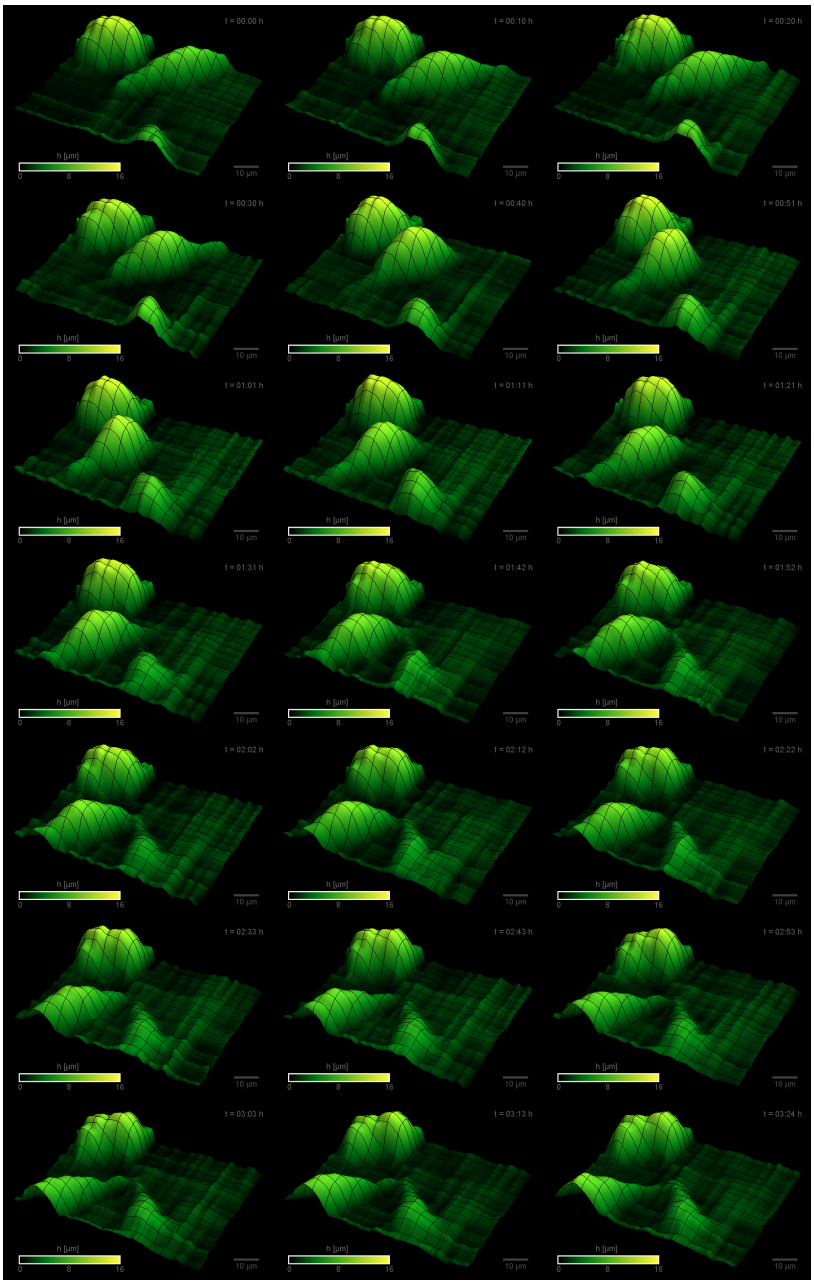

Figure A.5: Time series of two migrating and a dividing cell. The images are reconstructed from time lapse, label-free distortion measurements. The time difference between two subsequent frames is 610 seconds.

A.5 TIME LAPSE 3D FOR DIFFRACTION CORRLATION

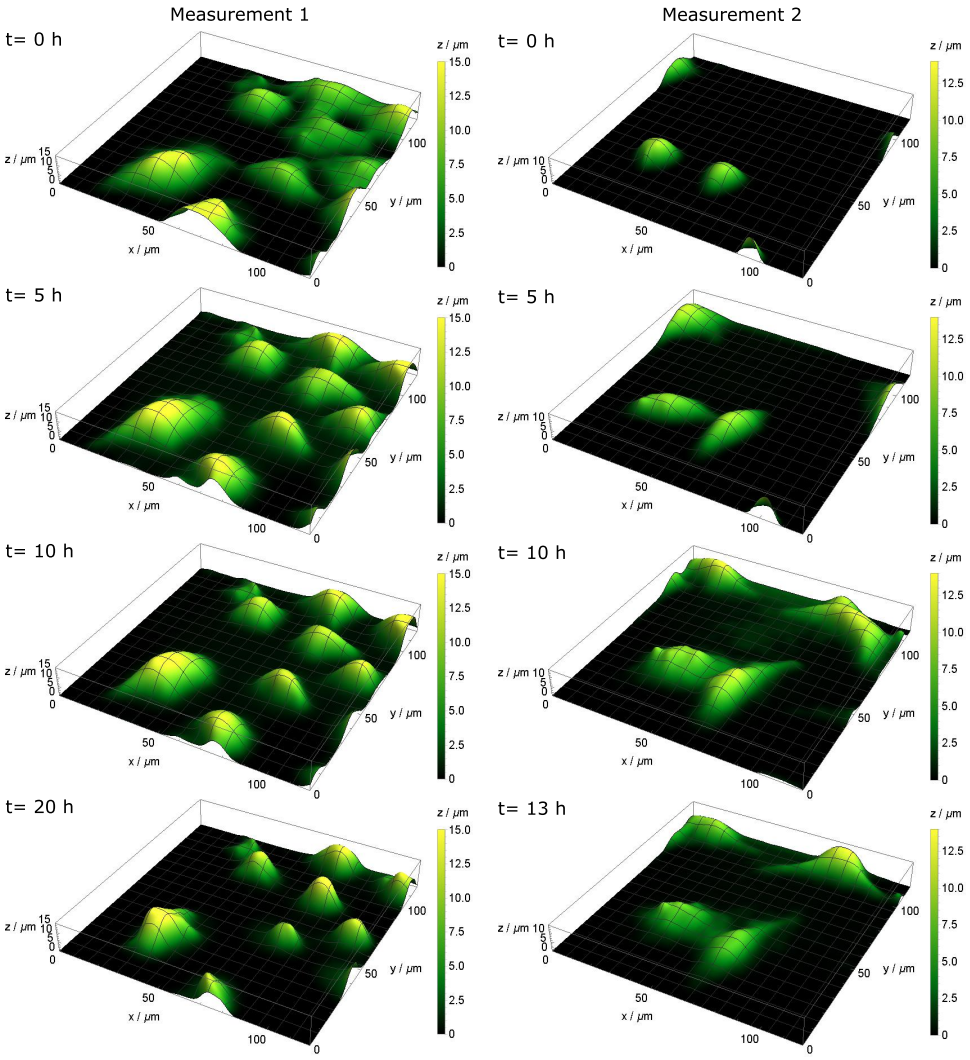

Figure A.6: Time series of two A549 cell ensemble measurements on a diffraction grid. The cells membrane is marked with a fluorescence label. Z-stacks of images are generated at each recorded time point. The reconstructed cell shapes are computed from the fluorescence data, using thresholding in mathematica.

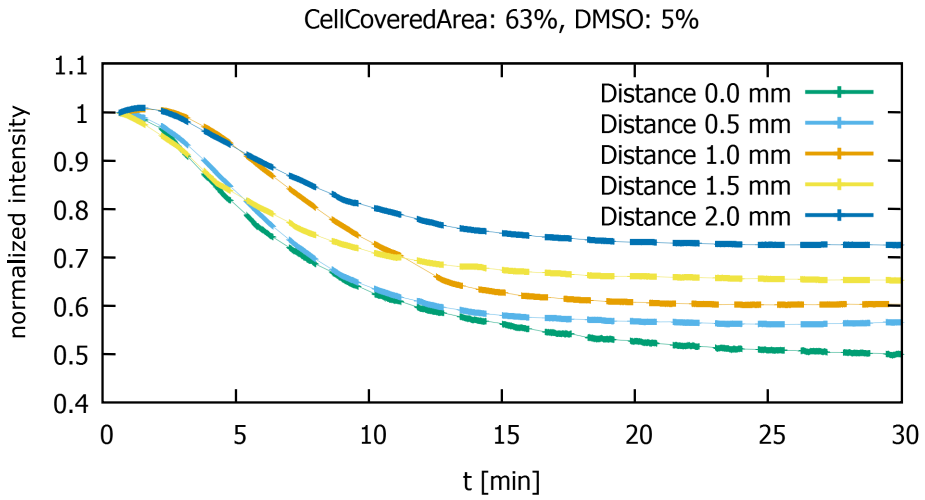

Figure A.7: Diffraction intensity change dependence on the distance between the A549 cell ensemble and the diffraction grating. The distance is measured from the bottom of the cell culture slide (6-channel).

A.6 DIFFRACTION SIGNAL DEPENDENCE ON GRATING DISTANCE

The model derived in Section 6.2 is able to predict the diffraction intensity for a cell ensemble directly on the diffraction grating. However, in the high throughput setup introduced in Section 3.4, the cells grow in a standard culture dish and the diffraction grating is placed directly under this dish. Therefore, there is a small distance between the cells and the grating. In order to show that the derived proportionality still holds, the difference between these two configurations in investigated here. To do so, a characteristic signal change is induced to the cell ensemble of A549 cells in both setups and the resulting intensity change is compared, depending on the distance between cells and grating. In Figure 6.8 the signal change over time, induced by a cell ensemble directly on a diffraction grid is depicted. This signal change is induced by exchanging the cell-medium with a medium that is supplemented with 5 % DMSO. This causes the cells in the ensemble to round up gradually, as can be seen by the sharper edges in the inset images of the cell layer at various times. The same experiment has been performed in the high throughput diffraction setup for various distances between the cell ensemble and the diffraction grating. This is depicted in Figure A.7. It can be seen that the characteristic signal that is induced by the medium supplemented with DMSO does not change, but that the magnitude of the signal change does decrease with increasing distance. Note that all experiments have been performed with cell ensembles, which have been cultured exactly the same and have been grown to approximately the same confluency. Still, the small difference in response time can be attributed to small difference in the cell ensemble confluency and state.

A.7 IMAGES COMPARISON OF CELLS IN 3D WITH AND WITHOUT CISPLATIN

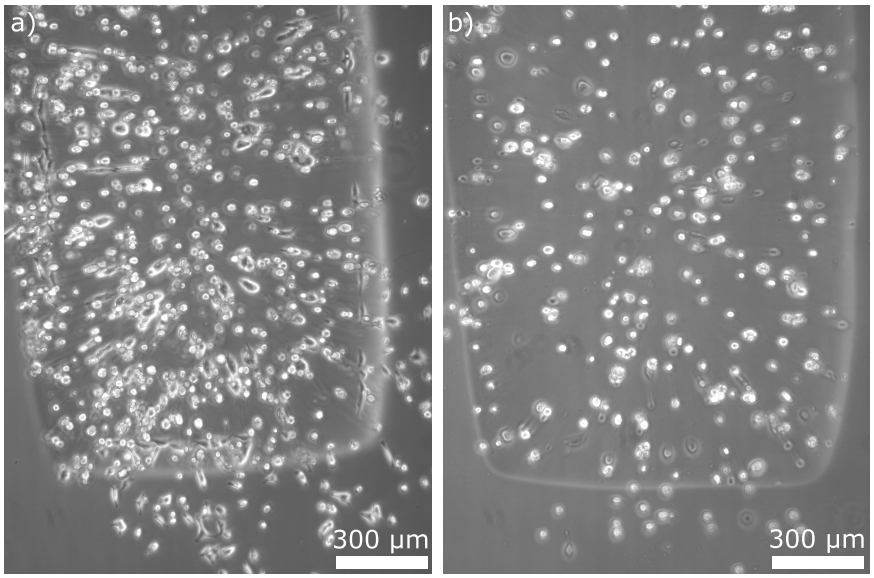

Figure A.8: Two A549 cell ensembles in 3D hydrogels. Both hydrogels had the same confluency at the beginning of the measurement. a) Cell ensemble after 40 hours of a diffraction measurement with standard cell culture medium. b). Cell ensemble after 40 hours of a diffraction measurement with medium that was supplemented with $80\,\mu M$ of cisplatin. The cells appear more rounded up and did not proliferate as much compared to the cells in a).

BIBLIOGRAPHY

[1] George M Stratton. "Upright vision and the retinal image." In: (1897).

[2] Ivo Kohler. "Experiments with goggles." In: *Scientific American* 206.5 (1962), pp. 62–73.

[3] Walter Gasson. "The oldest lens in the world." In: *Ophthalmic Optician* 12 (1972), pp. 1267–1272.

[4] George Sines and Yannis A Sakellarakis. "Lenses in antiquity." In: *American Journal of Archaeology* (1987), pp. 191–196.

[5] Savile Bradbury. *The evolution of the microscope*. Elsevier, 2014.

[6] Melvin L Rubin. "Spectacles: past, present, and future." In: *Survey of ophthalmology* 30.5 (1986), pp. 321–327.

[7] Brian J Ford. "From Dilettante to Diligent Experimenter, a Reappraisal of Leeuwenhoek as microscopist and investigator." In: *Biology History* 5.3 (1992), pp. 5–6.

[8] Timothy C Kriss and Vesna Martich Kriss. "History of the operating microscope: from magnifying glass to microneurosurgery." In: *Neurosurgery* 42.4 (1998), pp. 899–907.

[9] Dieter Gerlach. *Geschichte der Mikroskopie*. Harri Deutsch Verlag, 2009.

[10] Leonhard Möckl, Don C Lamb, and Christoph Bräuchle. "Super-resolved Fluorescence Microscopy: Nobel Prize in Chemistry 2014 for Eric Betzig, Stefan Hell, and William E. Moerner." In: *Angewandte Chemie International Edition* 53.51 (2014), pp. 13972–13977.

[11] Stefan W Hell and Ernst HK Stelzer. "Lens aberrations in confocal fluorescence microscopy." In: *Handbook of biological confocal microscopy*. Springer, 1995, pp. 347–354.

[12] Joel A. Kubby. *Adaptive Optics for Biological Imaging*. 1st ed. Boca Raton, FL, USA: CRC Press, 2013.

[13] Andrew M Sydor, Kirk J Czymmek, Elias M Puchner, and Vito Mennella. "Super-resolution microscopy: from single molecules to supramolecular assemblies." In: *Trends in cell biology* 25.12 (2015), pp. 730–748.

[14] Martin J Booth. "Adaptive optics in microscopy." In: *Philosophical Transactions of the Royal Society of London A: Mathematical, Physical and Engineering Sciences* 365.1861 (2007), pp. 2829–2843.

[15] Zhe Liu, Luke D Lavis, and Eric Betzig. "Imaging live-cell dynamics and structure at the single-molecule level." In: *Molecular cell* 58.4 (2015), pp. 644–659.

[16] Etienne Cuche, Frederic Bevilacqua, and Christian Depeursinge. "Digital holography for quantitative phase-contrast imaging." In: *Optics letters* 24.5 (1999), pp. 291–293.

[17] Jose-Philippe Perez. *Optik*. 1st ed. Heidelberg, Germany: Spektrum Akademischer Verlag GmbH, 1996.

[18] TE Furtak and MV Klein. *Optik*. 1988.

[19] Eugene Hecht. *Optics. 3rd Edition*. 3rd ed. USA: Addison Wesley Longman, 1998.

[20] Ernst Abbe. "Beiträge zur Theorie des Mikroskops und der mikroskopischen Wahrnehmung." In: *Archiv für mikroskopische Anatomie* 9.1 (1873), pp. 413–418.

[21] Bruce Alberts, Alexander Johnson, Julian Lewis, Martin Raff, Keith Roberts, and Peter Walter. "Molecular Biology of the Cell." In: (2002).

[22] Frits Zernike. "Phase contrast, a new method for the microscopic observation of transparent objects." In: *Physica* 9.7 (1942), pp. 686–698.

[23] Erich Sackmann and Rudolf Merkel. *Lehrbuch der Biophysik*. Wiley-VCH, 2010.

[24] John R Masters and Glyn N Stacey. "Changing medium and passaging cell lines." In: *Nature protocols* 2.9 (2007), p. 2276.

[25] David J Stephens and Victoria J Allan. "Light microscopy techniques for live cell imaging." In: *Science* 300.5616 (2003), pp. 82–86.

[26] Taewoo Kim, Renjie Zhou, Mustafa Mir, S Derin Babacan, P Scott Carney, Lynford L Goddard, and Gabriel Popescu. "White-light diffraction tomography of unlabelled live cells." In: *Nature Photonics* 8.3 (2014), p. 256.

[27] Gabriel Popescu, Takahiro Ikeda, Ramachandra R Dasari, and Michael S Feld. "Diffraction phase microscopy for quantifying cell structure and dynamics." In: *Optics letters* 31.6 (2006), pp. 775–777.

[28] Pierre Marquet, Benjamin Rappaz, Pierre J Magistretti, Etienne Cuche, Yves Emery, Tristan Colomb, and Christian Depeursinge. "Digital holographic microscopy: a noninvasive contrast imaging technique allowing quantitative visualization of living cells with subwavelength axial accuracy." In: *Optics letters* 30.5 (2005), pp. 468–470.

[29] Takahiro Ikeda, Gabriel Popescu, Ramachandra R Dasari, and Michael S Feld. "Hilbert phase microscopy for investigating fast dynamics in transparent systems." In: *Optics letters* 30.10 (2005), pp. 1165–1167.

[30] Elizabeth A Specht, Esther Braselmann, and Amy E Palmer. "A critical and comparative review of fluorescent tools for live-cell imaging." In: *Annual review of physiology* 79 (2017), pp. 93–117.

[31] Roger Y Tsien. *The green fluorescent protein*. 1998.

[32] James G Fujimoto and Daniel Farkas. *Biomedical optical imaging*. Oxford University Press, 2009.

[33] Akihiko Nakano. "Spinning-disk confocal microscopy—a cutting-edge tool for imaging of membrane traffic." In: *Cell structure and function* 27.5 (2002), pp. 349–355.

[34] Bi-Chang Chen, Wesley R Legant, Kai Wang, Lin Shao, Daniel E Milkie, Michael W Davidson, Chris Janetopoulos, Xufeng S Wu, John A Hammer, Zhe Liu, et al. "Lattice light-sheet microscopy: imaging molecules to embryos at high spatiotemporal resolution." In: *Science* 346.6208 (2014), p. 1257998.

[35] Ellen C Jensen. "Use of fluorescent probes: their effect on cell biology and limitations." In: *The Anatomical Record: Advances in Integrative Anatomy and Evolutionary Biology* 295.12 (2012), pp. 2031–2036.

[36] Daniel L Coutu and Timm Schroeder. "Probing cellular processes by long-term live imaging–historic problems and current solutions." In: *J Cell Sci* (2013), jcs–118349.

[37] RK Saetzler, J Jallo, HA Lehr, CM Philips, U Vasthare, KE Arfors, and RF Tuma. "Intravital fluorescence microscopy: impact of light-induced phototoxicity on adhesion of fluorescently labeled leukocytes." In: *Journal of Histochemistry & Cytochemistry* 45.4 (1997), pp. 505–513.

[38] Ram Dixit and Richard Cyr. "Cell damage and reactive oxygen species production induced by fluorescence microscopy: effect on mitosis and guidelines for non-invasive fluorescence microscopy." In: *The Plant Journal* 36.2 (2003), pp. 280–290.

[39] Eric Betzig, Stefan W Hell, and William E Moerner. "The Nobel Prize in Chemistry 2014." In: *Nobelprize. org. http://www. nobelprize. org/nobel_prizes/chemistry/laureates/2014/. Accessed* 24 (2015).

[40] Antoine G Godin, Brahim Lounis, and Laurent Cognet. "Super-resolution microscopy approaches for live cell imaging." In: *Biophysical journal* 107.8 (2014), pp. 1777–1784.

[41] Audrey M Glauert and Peter R Lewis. *Biological specimen preparation for transmission electron microscopy*. Vol. 80. Princeton University Press, 2014.

[42] Varun Rastogi, Naveen Puri, Swati Arora, Geetpriya Kaur, Lalita Yadav, and Rachna Sharma. "Artefacts: a diagnostic dilemma–a review." In: *Journal of clinical and diagnostic research: JCDR* 7.10 (2013), p. 2408.

[43] John Maxwell Cowley. *Diffraction physics*. Elsevier, 1995.

[44] Samira Hertrich, Frank Stetter, Adrian Ruhm, Thorsten Hugel, and Bert Nickel. "Highly hydrated deformable polyethylene glycol-tethered lipid bilayers." In: *Langmuir* 30.31 (2014), pp. 9442–9447.

[45] Stefan Fischer, Caroline Hartl, Kilian Frank, Joachim O Rädler, Tim Liedl, and Bert Nickel. "Shape and interhelical spacing of DNA origami nanostructures studied by small-angle X-ray scattering." In: *Nano letters* 16.7 (2016), pp. 4282–4287.

[46] Gerd Binnig, Calvin F Quate, and Ch Gerber. "Atomic force microscope." In: *Physical review letters* 56.9 (1986), p. 930.

[47] Wolfgang Ott, Markus A Jobst, Constantin Schoeler, Hermann E Gaub, and Michael A Nash. "Single-molecule force spectroscopy on polyproteins and receptor–ligand complexes: The current toolbox." In: *Journal of structural biology* 197.1 (2017), pp. 3–12.

[48] Ben C Platt and Roland Shack. "History and principles of Shack-Hartmann wavefront sensing." In: *Journal of Refractive Surgery* 17.5 (2001), S573–S577.

[49] Junzhong Liang, Bernhard Grimm, Stefan Goelz, and Josef F Bille. "Objective measurement of wave aberrations of the human eye with the use of a Hartmann–Shack wave-front sensor." In: *JOSA A* 11.7 (1994), pp. 1949–1957.

[50] S Hell, G Reiner, C Cremer, and Ernst HK Stelzer. "Aberrations in confocal fluorescence microscopy induced by mismatches in refractive index." In: *Journal of microscopy* 169.3 (1993), pp. 391–405.

[51] Sarah Frisken Gibson and Frederick Lanni. "Experimental test of an analytical model of aberration in an oil-immersion objective lens used in three-dimensional light microscopy." In: *JOSA A* 9.1 (1992), pp. 154–166.

[52] Alexander Egner and Stefan W Hell. "Aberrations in confocal and multi-photon fluorescence microscopy induced by refractive index mismatch." In: *Handbook of biological confocal microscopy*. Springer, 2006, pp. 404–413.

[53] Martin J Booth. "Adaptive optical microscopy: the ongoing quest for a perfect image." In: *Light: Science & Applications* 3.4 (2014), e165.

[54] Markus Rueckel, Julia A Mack-Bucher, and Winfried Denk. "Adaptive wavefront correction in two-photon microscopy using coherence-gated wavefront sensing." In: *Proceedings of the National Academy of Sciences* 103.46 (2006), pp. 17137–17142.

[55] Saad A Rahman and Martin J Booth. "Direct wavefront sensing in adaptive optical microscopy using backscattered light." In: *Applied optics* 52.22 (2013), pp. 5523–5532.

[56] Oscar Azucena, Justin Crest, Shaila Kotadia, William Sullivan, Xiaodong Tao, Marc Reinig, Donald Gavel, Scot Olivier, and Joel Kubby. "Adaptive optics wide-field microscopy using direct wavefront sensing." In: *Optics letters* 36.6 (2011), pp. 825–827.

[57] C Bourgenot, CD Saunter, GD Love, and JM Girkin. "Comparison of closed loop and sensorless adaptive optics in widefield optical microscopy." In: *Journal of the European Optical Society-Rapid publications* 8 (2013).

[58] Pierre Vermeulen, Eleonora Muro, Thomas Pons, Vincent Loriette, and Alexandra Fragola. "Adaptive optics for fluorescence wide-field microscopy using spectrally independent guide star and markers." In: *Journal of Biomedical Optics* 16.7 (2011), p. 076019.

[59] Na Ji, Daniel E Milkie, and Eric Betzig. "Adaptive optics via pupil segmentation for high-resolution imaging in biological tissues." In: *Nature methods* 7.2 (2010), p. 141.

[60] Z Kam, B Hanser, MGL Gustafsson, DA Agard, and JW Sedat. "Computational adaptive optics for live three-dimensional biological imaging." In: *Proceedings of the National Academy of Sciences* 98.7 (2001), pp. 3790–3795.

[61] Delphine Débarre, Edward J Botcherby, Tomoko Watanabe, Shankar Srinivas, Martin J Booth, and Tony Wilson. "Image-based adaptive optics for two-photon microscopy." In: *Optics letters* 34.16 (2009), pp. 2495–2497.

[62] Daniel Burke, Brian Patton, Fang Huang, Joerg Bewersdorf, and Martin J Booth. "Adaptive optics correction of specimen-induced aberrations in single-molecule switching microscopy." In: *Optica* 2.2 (2015), pp. 177–185.

[63] Martin J Booth, Delphine Débarre, and Alexander Jesacher. "Adaptive optics for biomedical microscopy." In: *Optics and photonics news* 23.1 (2012), pp. 22–29.

[64] Michael Schwertner, Martin J Booth, and Tony Wilson. "Specimen-induced distortions in light microscopy." In: *Journal of microscopy* 228.1 (2007), pp. 97–102.

[65] Robert J Noll. "Zernike polynomials and atmospheric turbulence." In: *JOsA* 66.3 (1976), pp. 207–211.

[66] Max Born and Emil Wolf. *Principles of optics: electromagnetic theory of propagation, interference and diffraction of light*. Elsevier, 2013.

[67] Mark AA Neil, Martin J Booth, and Tony Wilson. "New modal wave-front sensor: a theoretical analysis." In: *JOSA A* 17.6 (2000), pp. 1098–1107.

[68] Peter J Shaw and David J Rawlins. "The point-spread function of a confocal microscope: its measurement and use in deconvolution of 3-D data." In: *Journal of Microscopy* 163.2 (1991), pp. 151–165.

[69] Philipp Paulitschke. "Mechanische Charakterisierung einzelner periodisch angeordneter nanoskaliger GaAs-Säulen." PhD thesis. München, 2011.

[70] Donald J Giard, Stuart A Aaronson, George J Todaro, Paul Arnstein, John H Kersey, Harvey Dosik, and Wade P Parks. "In vitro cultivation of human tumors: establishment of cell lines derived from a series of solid tumors." In: *Journal of the National Cancer Institute* 51.5 (1973), pp. 1417–1423.

[71] Chiara Vecchi, Giuliana Montosi, and Antonello Pietrangelo. "Huh-7: A human "hemochromatotic" cell line." In: *Hepatology* 51.2 (2010), pp. 654–659.

[72] BR Brinkley, PT Beall, LJ Wible, ML Mace, Donna S Turner, and RM Cailleau. "Variations in cell form and cytoskeleton in human breast carcinoma cells in vitro." In: *Cancer research* 40.9 (1980), pp. 3118–3129.

[73] SC Bayliss, LD Buckberry, PJ Harris, and M Tobin. "Nature of the silicon-animal cell interface." In: *Journal of Porous Materials* 7.1-3 (2000), pp. 191–195.

[74] Steve Wolter, Anna Löschberger, Thorge Holm, Sarah Aufmkolk, Marie-Christine Dabauvalle, Sebastian Van De Linde, and Markus Sauer. "rapidSTORM: accurate, fast open-source software for localization microscopy." In: *Nature methods* 9.11 (2012), p. 1040.

[75] Vitor R Manfrinato, Jianguo Wen, Lihua Zhang, Yujia Yang, Richard G Hobbs, Bowen Baker, Dong Su, Dmitri Zakharov, Nestor J Zaluzec, Dean J Miller, et al. "Determining the resolution limits of electron-beam lithography: direct measurement of the point-spread function." In: *Nano letters* 14.8 (2014), pp. 4406–4412.

[76] Valentin Stierle. "Characterizing Cellular Behavior With Lensless Microscopy." PhD thesis. München, 2018.

[77] Francisco F Medina, Jorge Garcia-Sucerquia, Roman Castaneda, and Giorgio Matteucci. "Angular criterion to distinguish between Fraunhofer and Fresnel diffraction." In: *Optik-International Journal for Light and Electron Optics* 115.11-12 (2004), pp. 547–552.

[78] Julian Aschauer. "High Throughput Interferometric Assay for Antimicrobial Susceptibility Testing in Ultra-Low Volume." MA thesis. München, 2018.

[79] Miriam Dietrich, Hugo Le Roy, David B Brückner, Hanna Engelke, Roman Zantl, Joachim O Rädler, and Chase P Broedersz. "Guiding 3D cell migration in deformed synthetic hydrogel microstructures." In: *Soft matter* 14.15 (2018), pp. 2816–2826.

[80] Benjamin D Fairbanks, Michael P Schwartz, Christopher N Bowman, and Kristi S Anseth. "Photoinitiated polymerization of PEG-diacrylate with lithium phenyl-2, 4, 6-trimethylbenzoylphosphinate: polymerization rate and cytocompatibility." In: *Biomaterials* 30.35 (2009), pp. 6702–6707.

[81] Jürgen Stephan, Felix Keber, Valentin Stierle, Joachim O Rädler, and Philipp Paulitschke. "Single-Cell Optical Distortion Correction and Label-Free 3D Cell Shape Reconstruction on Lattices of Nanostructures." In: *Nano letters* 17.12 (2017), pp. 8018–8023.

[82] James B Pawley. "Limitations on optical sectioning in live-cell confocal microscopy." In: *Scanning* 24.5 (2002), pp. 241–246.

[83] Martin J Booth, Michael Schwertner, and Tony Wilson. "Specimen-induced aberrations and adaptive optics for microscopy." In: *Advanced Wavefront Control: Methods, Devices, and Applications III*. Vol. 58-94. International Society for Optics and Photonics. 2005, p. 589403.

[84] Micah Dembo and Yu-Li Wang. "Stresses at the cell-to-substrate interface during locomotion of fibroblasts." In: *Biophysical journal* 76.4 (1999), pp. 2307–2316.

[85] Pere Roca-Cusachs, Vito Conte, and Xavier Trepat. "Quantifying forces in cell biology." In: *Nature cell biology* 19.7 (2017), p. 742.

[86] Ingmar Schoen, Wei Hu, Enrico Klotzsch, and Viola Vogel. "Probing cellular traction forces by micropillar arrays: contribution of substrate warping to pillar deflection." In: *Nano letters* 10.5 (2010), pp. 1823–1830.

[87] Myriam Reffay, Maria-Carla Parrini, Olivier Cochet-Escartin, Benoıt Ladoux, Axel Buguin, S Coscoy, François Amblard, Jacques Camonis, and Pascal Silberzan. "Interplay of RhoA and mechanical forces in collective cell migration driven by leader cells." In: *Nature cell biology* 16.3 (2014), p. 217.

[88] Huw Colin-York, Dilip Shrestha, James H Felce, Dominic Waithe, Emad Moeendarbary, Simon J Davis, Christian Eggeling, and Marco Fritzsche. "Super-resolved traction force microscopy (STFM)." In: *Nano letters* 16.4 (2016), pp. 2633–2638.

[89] Wesley R Legant, Colin K Choi, Jordan S Miller, Lin Shao, Liang Gao, Eric Betzig, and Christopher S Chen. "Multidimensional traction force microscopy reveals out-of-plane rotational moments about focal adhesions." In: *Proceedings of the National Academy of Sciences* 110.3 (2013), pp. 881–886.

[90] Hedde van Hoorn, Rolf Harkes, Ewa M Spiesz, Cornelis Storm, Danny van Noort, Benoit Ladoux, and Thomas Schmidt. "The nanoscale architecture of force-bearing focal adhesions." In: *Nano letters* 14.8 (2014), pp. 4257–4262.

[91] Hayri E Balcioglu, Hedde van Hoorn, Dominique M Donato, Thomas Schmidt, and Erik HJ Danen. "The integrin expression profile modulates orientation and dynamics of force transmission at cell–matrix adhesions." In: *J Cell Sci* 128.7 (2015), pp. 1316–1326.

[92] Waldemar Hallstrom, Monica Lexholm, Dmitry B Suyatin, Greger Hammarin, Dan Hessman, Lars Samuelson, Lars Montelius, Martin Kanje, and Christelle N Prinz. "Fifteen-piconewton force detection from neural growth cones using nanowire arrays." In: *Nano letters* 10.3 (2010), pp. 782–787.

[93] Prasana K Sahoo, Richard Janissen, Moniellen P Monteiro, Alessandro Cavalli, Duber M Murillo, Marcus V Merfa, Carlos L Cesar, Hernandes F Carvalho, Alessandra A de Souza, Erik PAM Bakkers, et al. "Nanowire arrays as cell force sensors to investigate adhesin-enhanced holdfast of single cell bacteria and biofilm stability." In: *Nano letters* 16.7 (2016), pp. 4656–4664.

[94] Aldeliane M da Silva, Prasana K Sahoo, Alessandro Cavalli, Alessandra A de Souza, Erik PAM Bakkers, Carlos L Cesar, Richard Janissen, and Monica A Cotta. "Nanowire Arrays as Force Sensors with Super-Resolved Localization Position Detection: Application to Optical Measurement of Bacterial Adhesion Forces." In: *Small Methods* (2018), p. 1700411.

[95] Zhen Li, Henrik Persson, Karl Adolfsson, Laura Abariute, Magnus T Borgström, Dan Hessman, Kalle Åström, Stina Oredsson, and Christelle N Prinz. "Cellular traction forces: a useful parameter in cancer research." In: *Nanoscale* 9.48 (2017), pp. 19039–19044.

[96] Juergen A Steyer and Wolf Almers. "A real-time view of life within 100 nm of the plasma membrane." In: *Nature reviews Molecular cell biology* 2.4 (2001), p. 268.

[97] Liang Gao, Lin Shao, Christopher D Higgins, John S Poulton, Mark Peifer, Michael W Davidson, Xufeng Wu, Bob Goldstein, and Eric Betzig. "Noninvasive imaging beyond the diffraction limit of 3D dynamics in thickly fluorescent specimens." In: *Cell* 151.6 (2012), pp. 1370–1385.

[98] Bonnie O Leung and Keng C Chou. "Review of super-resolution fluorescence microscopy for biology." In: *Applied spectroscopy* 65.9 (2011), pp. 967–980.

[99] Colin J Fuller and Aaron F Straight. "Imaging nanometre-scale structure in cells using in situ aberration correction." In: *Journal of microscopy* 248.1 (2012), pp. 90–101.

[100] Roman I Koning, Vladimir G Kutchoukov, Cornelis W Hagen, and Abraham J Koster. "Nanofabrication of a gold fiducial array on specimen support for electron tomography." In: *Ultramicroscopy* 135 (2013), pp. 99–104.

[101] M Schnedler, PH Weidlich, V Portz, D Weber, RE Dunin-Borkowski, and Ph Ebert. "Correction of nonlinear lateral distortions of scanning probe microscopy images." In: *Ultramicroscopy* 136 (2014), pp. 86–90.

[102] Alexander D Corbett, Rebecca AB Burton, Gil Bub, Patrick S Salter, Simon Tuohy, Martin J Booth, and Tony Wilson. "Quantifying distortions in two-photon remote focussing microscope images using a volumetric calibration specimen." In: *Frontiers in physiology* 5 (2014), p. 384.

[103] Philipp Paulitschke, Felix Keber, Andrej Lebedev, Jürgen Stephan, Bert Lorenz, Sebastian Hasselmann, Doris Heinrich, and Eva Weig. "Ultra-flexible nanowire array for label-and distortion-free cellular force tracking." In: *Nano Letters* (2018).

[104] Lorena Diéguez, N Darwish, M Mir, Elena Martinez, M Moreno, and Josep Samitier. "Effect of the refractive index of buffer solutions in evanescent optical biosensors." In: *Sensor letters* 7.5 (2009), pp. 851–855.

[105] Zachary A Steelman, Will J Eldridge, Jacob B Weintraub, and Adam Wax. "Is the nuclear refractive index lower than cytoplasm? Validation of phase measurements and implications for light scattering technologies." In: *Journal of biophotonics* 10.12 (2017), pp. 1714–1722.

[106] PY Liu, LK Chin, W Ser, HF Chen, C-M Hsieh, C-H Lee, K-B Sung, TC Ayi, PH Yap, B Liedberg, et al. "Cell refractive index for cell biology and disease diagnosis: past, present and future." In: *Lab on a Chip* 16.4 (2016), pp. 634–644.

[107] Wonshik Choi, Christopher Fang-Yen, Kamran Badizadegan, Seungeun Oh, Niyom Lue, Ramachandra R Dasari, and Michael S Feld. "Tomographic phase microscopy." In: *Nature methods* 4.9 (2007), p. 717.

[108] Niyom Lue, Wonshik Choi, Gabriel Popescu, Zahid Yaqoob, Kamran Badizadegan, Ramachandra R Dasari, and Michael S Feld. "Live cell refractometry using Hilbert phase microscopy and confocal reflectance microscopy." In: *The Journal of Physical Chemistry A* 113.47 (2009), pp. 13327–13330.

[109] Claire L Curl, Catherine J Bellair, Trudi Harris, Brendan E Allman, Peter J Harris, Alastair G Stewart, Ann Roberts, Keith A Nugent, and Lea MD Delbridge. "Refractive index measurement in viable cells using quantitative phase-amplitude microscopy and confocal microscopy." In: *Cytometry Part A: The Journal of the International Society for Analytical Cytology* 65.1 (2005), pp. 88–92.

[110] Albert Brunsting and Paul F Mullaney. "Differential light scattering from spherical mammalian cells." In: *Biophysical journal* 14.6 (1974), p. 439.

[111] Na Ji, Daniel E Milkie, and Eric Betzig. "Adaptive optics via pupil segmentation for high-resolution imaging in biological tissues." In: *Nature methods* 7.2 (2009), p. 141.

[112] H MichelleáGrandin et al. "Micro-well arrays for 3D shape control and high resolution analysis of single cells." In: *Lab on a Chip* 7.8 (2007), pp. 1074–1077.

[113] Peter JF Röttgermann, Alicia Piera Alberola, and Joachim O Rädler. "Cellular self-organization on micro-structured surfaces." In: *Soft Matter* 10.14 (2014), pp. 2397–2404.

[114] Melissa G Mendez, Shin-Ichiro Kojima, and Robert D Goldman. "Vimentin induces changes in cell shape, motility, and adhesion during the epithelial to mesenchymal transition." In: *The FASEB Journal* 24.6 (2010), pp. 1838–1851.

[115] Rohan Samarakoon and Paul J Higgins. "MEK/ERK pathway mediates cell-shape-dependent plasminogen activator inhibitor type 1 gene expression upon drug-induced disruption of the microfilament and microtubule networks." In: *J Cell Sci* 115.15 (2002), pp. 3093–3103.

[116] Donald E Ingber, Deepa Prusty, Zhengqi Sun, Hannah Betensky, and Ning Wang. "Cell shape, cytoskeletal mechanics, and cell cycle control in angiogenesis." In: *Journal of biomechanics* 28.12 (1995), pp. 1471–1484.

[117] Amandine Pitaval, Qingzong Tseng, Michel Bornens, and Manuel Théry. "Cell shape and contractility regulate ciliogenesis in cell cycle–arrested cells." In: *The Journal of cell biology* 191.2 (2010), pp. 303–312.

[118] Thomas D Pollard, William C Earnshaw, Jennifer Lippincott-Schwartz, and Graham Johnson. *Cell Biology E-Book*. Elsevier Health Sciences, 2016.

[119] Ryuji Kato, Megumi Matsumoto, Hiroto Sasaki, Risako Joto, Mai Okada, Yurika Ikeda, Kei Kanie, Mika Suga, Masaki Kinehara, Kana Yanagihara, et al. "Parametric analysis of colony morphology of non-labelled live human pluripotent stem cells for cell quality control." In: *Scientific reports* 6 (2016), p. 34009.

[120] Aimee L Edinger and Craig B Thompson. "Death by design: apoptosis, necrosis and autophagy." In: *Current opinion in cell biology* 16.6 (2004), pp. 663–669.

[121] Fumiko Matsuoka, Ichiro Takeuchi, Hideki Agata, Hideaki Kagami, Hirofumi Shiono, Yasujiro Kiyota, Hiroyuki Honda, and Ryuji Kato. "Morphology-based prediction of osteogenic differentiation potential of human mesenchymal stem cells." In: *PloS one* 8.2 (2013), e55082.

[122] Linliang Yin, Wei Wang, Shaopeng Wang, Fenni Zhang, Shengtao Zhang, and Nongjian Tao. "How does fluorescent labeling affect the binding kinetics of proteins with intact cells?" In: *Biosensors and Bioelectronics* 66 (2015), pp. 412–416.

[123] Jaroslav Icha, Michael Weber, Jennifer C Waters, and Caren Norden. "Phototoxicity in live fluorescence microscopy, and how to avoid it." In: *Bioessays* 39.8 (2017), p. 1700003.

[124] Biao Xi, Naichen Yu, Xiaobo Wang, Xiao Xu, and Yama Abassi. "The application of cell-based label-free technology in drug discovery." In: *Biotechnology Journal: Healthcare Nutrition Technology* 3.4 (2008), pp. 484–495.

[125] Jiranuwat Sapudom, Johannes Waschke, Katja Franke, Mario Hlawitschka, and Tilo Pompe. "Quantitative label-free single cell tracking in 3D biomimetic matrices." In: *Scientific Reports* 7.1 (2017), p. 14135.

[126] Lena Kastl, Michael Isbach, Dieter Dirksen, Jürgen Schnekenburger, and Björn Kemper. "Quantitative phase imaging for cell culture quality control." In: *Cytometry Part A* 91.5 (2017), pp. 470–481.

[127] Benjamin Rappaz, Pierre Marquet, Etienne Cuche, Yves Emery, Christian Depeursinge, and Pierre J Magistretti. "Measurement of the integral refractive index and dynamic cell morphometry of living cells with digital holographic microscopy." In: *Optics express* 13.23 (2005), pp. 9361–9373.

[128] Daniel Boss, Jonas Kühn, Pascal Jourdain, Christian D Depeursinge, Pierre J Magistretti, and Pierre P Marquet. "Measurement of absolute cell volume, osmotic membrane water permeability, and refractive index of transmembrane water and solute flux by digital holographic microscopy." In: *Journal of biomedical optics* 18.3 (2013), p. 036007.

[129] Alexander Khmaladze, Rebecca L Matz, Tamir Epstein, Joshua Jasensky, Mark M Banaszak Holl, and Zhan Chen. "Cell volume changes during apoptosis monitored in real time using digital holographic microscopy." In: *Journal of Structural Biology* 178.3 (2012), pp. 270–278.

[130] Matthew F Peters, François Vaillancourt, Madeleine Heroux, Manon Valiquette, and Clay W Scott. "Comparing label-free biosensors for pharmacological screening with cell-based functional assays." In: *Assay and drug development technologies* 8.2 (2010), pp. 219–227.

[131] Else K Hoffmann, Ian H Lambert, and Stine F Pedersen. "Physiology of cell volume regulation in vertebrates." In: *Physiological reviews* 89.1 (2009), pp. 193–277.

[132] Steffen Hamann, Jens Folke Kiilgaard, Thomas Litman, Francisco J Alvarez-Leefmans, Benny R Winther, and Thomas Zeuthen. "Measurement of cell volume changes by fluorescence self-quenching." In: *Journal of fluorescence* 12.2 (2002), pp. 139–145.

[133] Hans G Drexler, Yoshinobu Matsuo, and Roderick AF MacLeod. "Continuous hematopoietic cell lines as model systems for leukemia–lymphoma research." In: *Leukemia research* 24.11 (2000), pp. 881–911.

[134] Elisa Michelini, Luca Cevenini, Laura Mezzanotte, Andrea Coppa, and Aldo Roda. "Cell-based assays: fuelling drug discovery." In: *Analytical and bioanalytical chemistry* 398.1 (2010), pp. 227–238.

[135] Otília Menyhárt, Hajnalka Harami-Papp, Saraswati Sukumar, Reinhold Schäfer, Luca Magnani, Oriol de Barrios, and Balázs Győrffy. "Guidelines for the selection of functional assays to evaluate the hallmarks of cancer." In: *Biochimica et Biophysica Acta (BBA)-Reviews on Cancer* 1866.2 (2016), pp. 300–319.

[136] Aarthi Ramesh, Aishwarya Pattabhi, and Maddaly Ravi. "Assays Used in vitro to Study Cancer Cell Lines." In: *Life Science Research* 1.01 (2016), pp. 19–24.

[137] G Sitta Sittampalam, Nathan P Coussens, K Brimacombe, A Grossman, M Arkin, D Auld, C Austin, J Baell, B Bejcek, TDY Chung, et al. "Assay guidance manual." In: (2004).

[138] Kevin Slater. "Cytotoxicity tests for high-throughput drug discovery." In: *Current opinion in biotechnology* 12.1 (2001), pp. 70–74.

[139] Ivar Giaever and Charles R Keese. "A morphological biosensor for mammalian cells." In: *Nature* 366.6455 (1993), pp. 591–592.

[140] Joachim Wegener, Charles R Keese, and Ivar Giaever. "Electric cell–substrate impedance sensing (ECIS) as a noninvasive means to monitor the kinetics of cell spreading to artificial surfaces." In: *Experimental cell research* 259.1 (2000), pp. 158–166.

[141] Youchun Xu, Xinwu Xie, Yong Duan, Lei Wang, Zhen Cheng, and Jing Cheng. "A review of impedance measurements of whole cells." In: *Biosensors and Bioelectronics* 77 (2016), pp. 824–836.

[142] AF Mansor, I Ibrahim, I Voiculescu, and AN Nordin. "Screen printed impedance biosensor for cytotoxicity studies of lung carcinoma cells." In: *International Conference for Innovation in Biomedical Engineering and Life Sciences*. Springer. 2015, pp. 122–126.

[143] Naichen Yu, Josephine M Atienza, Jerome Bernard, Sebastien Blanc, Jenny Zhu, Xiaobo Wang, Xiao Xu, and Yama A Abassi. "Real-time monitoring of morphological changes in living cells by electronic cell sensor arrays: an approach to study G protein-coupled receptors." In: *Analytical chemistry* 78.1 (2006), pp. 35–43.

[144] Rudolf Robelek. "Surface plasmon resonance sensors in cell biology: basics and application." In: *Bioanalytical Reviews* 1.1 (2009), p. 57.

[145] Ye Fang, Ann M Ferrie, Norman H Fontaine, John Mauro, and Jitendra Balakrishnan. "Resonant waveguide grating biosensor for living cell sensing." In: *Biophysical journal* 91.5 (2006), pp. 1925–1940.

[146] Shijie Deng, Xinglong Yu, Ran Liu, Weixing Chen, and Peng Wang. "A two-compartment microfluidic device for long-term live cell detection based on surface plasmon resonance." In: *Biomicrofluidics* 10.4 (2016), p. 044109.

[147] Jean-Sébastien Maltais, Jean-Bernard Denault, Louis Gendron, and Michel Grandbois. "Label-free monitoring of apoptosis by surface plasmon resonance detection of morphological changes." In: *Apoptosis* 17.8 (2012), pp. 916–925.

[148] Ye Fang. "Label-free biosensors for cell biology." In: *International Journal of Electrochemistry* 2011 (2011).

[149] Norbert Orgovan, Beatrix Peter, Szilvia Bősze, Jeremy J Ramsden, Bálint Szabó, and Robert Horvath. "Dependence of cancer cell adhesion kinetics on integrin ligand surface density measured by a high-throughput label-free resonant waveguide grating biosensor." In: *Scientific reports* 4 (2014), p. 4034.

[150] Jonas Zähringer. "Interferometric Analysis of Eukaryotic Cell Ensembles in 2D monolayer and 3D culture." MA thesis. München, 2018.

[151] Luis Polo-Parada, Gerardo Gutiérrez-Juárez, David Cywiak, Rafael Pérez-Solano, and Gary A Baker. "Spectrophotometric analysis at the single-cell level: elucidating dispersity within melanic immortalized cell populations." In: *Analyst* 142.9 (2017), pp. 1482–1491.

[152] David Volbers. "Real-Time Interferometric Cell Ensemble Analysis." MA thesis. München, 2014.

[153] Nuno C Santos, J Figueira-Coelho, João Martins-Silva, and Carlota Saldanha. "Multidisciplinary utilization of dimethyl sulfoxide: pharmacological, cellular, and molecular aspects." In: *Biochemical pharmacology* 65.7 (2003), pp. 1035–1041.

[154] Katy Phelan and Kristin M May. "Basic techniques in mammalian cell tissue culture." In: *Current protocols in cell biology* 66.1 (2015), pp. 1–1.

[155] Josimeri Hebling, L Bianchi, FG Basso, DL Scheffel, DG Soares, MRO Carrilho, David Henry Pashley, L Tjäderhane, and CA de Souza Costa. "Cytotoxicity of dimethyl sulfoxide (DMSO) in direct contact with odontoblast-like cells." In: *Dental Materials* 31.4 (2015), pp. 399–405.

[156] DR Branch, S Calderwood, MA Cecuiti, R Herst, and H Solh. "Hematopoietic progenitor cells are resistant to dimethyl sulfoxide toxicity." In: *Transfusion* 34.10 (1994), pp. 887–890.

[157] Joana Galvao, Benjamin Davis, Mark Tilley, Eduardo Normando, Michael R Duchen, and M Francesca Cordeiro. "Unexpected low-dose toxicity of the universal solvent DMSO." In: *The FASEB Journal* 28.3 (2014), pp. 1317–1330.

[158] Chen Zhang, Yuanying Deng, Hongmei Dai, Wenjuan Zhou, Jing Tian, Guoying Bing, and Lingling Zhao. "Effects of dimethyl sulfoxide on the morphology and viability of primary cultured neurons and astrocytes." In: *Brain research bulletin* 128 (2017), pp. 34–39.

[159] Chan Yuan, Junying Gao, Jichao Guo, Lei Bai, Charles Marshall, Zhiyou Cai, Linmei Wang, and Ming Xiao. "Dimethyl sulfoxide damages mitochondrial integrity and membrane potential in cultured astrocytes." In: *PloS one* 9.9 (2014), e107447.

[160] Georges Da Violante, Naima Zerrouk, Isabelle Richard, Gérard Provot, Jean Claude Chaumeil, and Philippe Arnaud. "Evaluation of the cytotoxicity effect of dimethyl sulfoxide (DMSO) on Caco2/TC7 colon tumor cell cultures." In: *Biological and pharmaceutical bulletin* 25.12 (2002), pp. 1600–1603.

[161] E Borenfreund, M Steinglass, G Korngold, and A Bendich. "Effect of dimethyl sulfoxide and dimethylformamide on the growth and morphology of tumor cells." In: *Annals of the New York Academy of Sciences* 243.1 (1975), pp. 164–171.

[162] Rajarshi Pal, Murali Krishna Mamidi, Anjan Kumar Das, and Ramesh Bhonde. "Diverse effects of dimethyl sulfoxide (DMSO) on the differentiation potential of human embryonic stem cells." In: *Archives of toxicology* 86.4 (2012), pp. 651–661.

[163] Chi-Chung Wang, Sheng-Yi Lin, Yi-Hua Lai, Ya-Jung Liu, Yuan-Lin Hsu, and Jeremy JW Chen. "Dimethyl sulfoxide promotes the multiple functions of the tumor suppressor HLJ1 through activator protein-1 activation in NSCLC cells." In: *PloS one* 7.4 (2012), e33772.

[164] Hamed Alborzinia, Suzan Can, Pavlo Holenya, Catharina Scholl, Elke Lederer, Igor Kitanovic, and Stefan Wölfl. "Real-time monitoring of cisplatin-induced cell death." In: *PloS one* 6.5 (2011), e19714.

[165] Shaloam Dasari and Paul Bernard Tchounwou. "Cisplatin in cancer therapy: molecular mechanisms of action." In: *European journal of pharmacology* 740 (2014), pp. 364–378.

[166] Jean-Pierre Pignon, Hélène Tribodet, Giorgio V Scagliotti, Jean-Yves Douillard, Frances A Shepherd, Richard J Stephens, Ariane Dunant, Valter Torri, Rafael Rosell, Lesley Seymour, et al. "Lung adjuvant cisplatin evaluation: a pooled analysis by the LACE Collaborative Group." In: *Journal of clinical oncology* 26.21 (2008), pp. 3552–3559.

[167] Matthew D Hall, Katherine A Telma, Ki-Eun Chang, Tobie D Lee, James P Madigan, John R Lloyd, Ian S Goldlust, James D Hoeschele, and Michael M Gottesman. "Say no to DMSO: dimethylsulfoxide inactivates cisplatin, carboplatin, and other platinum complexes." In: *Cancer research* (2014).

[168] JL Sebaugh. "Guidelines for accurate EC50/IC50 estimation." In: *Pharmaceutical statistics* 10.2 (2011), pp. 128–134.

[169] Carly St Germain, Nima Niknejad, Laurie Ma, Kyla Garbuio, Tsonwin Hai, and Jim Dimitroulakos. "Cisplatin Induces Cytotoxicity through the Mitogen-Activated Protein Kinase Pathways ana Activating Transcription Factor 3." In: *Neoplasia* 12.7 (2010), pp. 527–538.

[170] Saki Yokokura, Nobuhiro Kanaji, Akira Tadokoro, Shigeyuki Yokokura, Norimitsu Kadowaki, and Shuji Bandoh. "Confluence-dependent resistance to cisplatin in lung cancer cells is regulated by transforming growth factor-beta." In: *Experimental lung research* 42.4 (2016), pp. 175–181.

[171] Qingjun Liu, Jinjiang Yu, Lidan Xiao, Johnny Cheuk On Tang, Yu Zhang, Ping Wang, and Mo Yang. "Impedance studies of bio-behavior and chemosensitivity of cancer cells by micro-electrode arrays." In: *Biosensors and Bioelectronics* 24.5 (2009), pp. 1305–1310.

[172] David Guay, Audrey-Ann Evoy, Eric Paquet, Chantal Garand, Magdalena Bachvarova, Dimcho Bachvarov, and Michel Lebel. "The strand separation and nuclease activities associated with YB-1 are dispensable for cisplatin resistance but overexpression of YB-1 in MCF7 and MDA-MB-231 breast tumor cells generates several chemoresistance

signatures." In: *The international journal of biochemistry & cell biology* 40.11 (2008), pp. 2492–2507.

[173] Florian Prinz, Thomas Schlange, and Khusru Asadullah. "Believe it or not: how much can we rely on published data on potential drug targets?" In: *Nature reviews Drug discovery* 10.9 (2011), p. 712.

[174] Rasheena Edmondson, Jessica Jenkins Broglie, Audrey F Adcock, and Liju Yang. "Three-dimensional cell culture systems and their applications in drug discovery and cell-based biosensors." In: *Assay and drug development technologies* 12.4 (2014), pp. 207–218.

[175] Jungwoo Lee, Meghan J Cuddihy, and Nicholas A Kotov. "Three-dimensional cell culture matrices: state of the art." In: *Tissue Engineering Part B: Reviews* 14.1 (2008), pp. 61–86.

[176] Alexandra Reininger-Mack, Hagen Thielecke, and Andrea A Robitzki. "3D-biohybrid systems: applications in drug screening." In: *TRENDS in Biotechnology* 20.2 (2002), pp. 56–61.

[177] Cornelia Hildebrandt, Heiko Büth, Sungbo Cho, Hagen Thielecke, et al. "Detection of the osteogenic differentiation of mesenchymal stem cells in 2D and 3D cultures by electrochemical impedance spectroscopy." In: *Journal of biotechnology* 148.1 (2010), pp. 83–90.

[178] Jong Bin Kim. "Three-dimensional tissue culture models in cancer biology." In: *Seminars in cancer biology*. Vol. 15. 5. Elsevier. 2005, pp. 365–377.

[179] Divya Khaitan, Sudhir Chandna, MB Arya, and BS Dwarakanath. "Establishment and characterization of multicellular spheroids from a human glioma cell line; Implications for tumor therapy." In: *Journal of translational medicine* 4.1 (2006), p. 12.

[180] JP Frampton, MR Hynd, JC Williams, ML Shuler, and W Shain. "Three-dimensional hydrogel cultures for modeling changes in tissue impedance around microfabricated neural probes." In: *Journal of neural engineering* 4.4 (2007), p. 399.

[181] Tien Anh Nguyen, Tsung-I Yin, Diego Reyes, and Gerald A Urban. "Microfluidic chip with integrated electrical cell-impedance sensing for monitoring single cancer cell migration in three-dimensional matrixes." In: *Analytical chemistry* 85.22 (2013), pp. 11068–11076.

[182] Lihong Zhou, Guoyou Huang, Shuqi Wang, Jinhui Wu, Won Gu Lee, Yongmei Chen, Feng Xu, and Tianjian Lu. "Advances in cell-based biosensors using three-dimensional cell-encapsulating hydrogels." In: *Biotechnology journal* 6.12 (2011), pp. 1466–1476.

[183] Daniel Kloß, Michael Fischer, Andrée Rothermel, Jan C Simon, and Andrea A Robitzki. "Drug testing on 3D in vitro tissues trapped on a microcavity chip." In: *Lab on a Chip* 8.6 (2008), pp. 879–884.

[184] Francesco Pampaloni and Ernst HK Stelzer. "Three-dimensional cell cultures in toxicology." In: *Biotechnology and Genetic Engineering Reviews* 26.1 (2009), pp. 117–138.

[185] Kin Fong Lei, Min-Hsien Wu, Che-Wei Hsu, and Yi-Dao Chen. "Real-time and non-invasive impedimetric monitoring of cell proliferation and chemosensitivity in a perfusion 3D cell culture microfluidic chip." In: *Biosensors and Bioelectronics* 51 (2014), pp. 16–21.

[186] Kin Fong Lei, Chia-Hao Huang, and Ngan-Ming Tsang. "Impedimetric quantification of cells encapsulated in hydrogel cultured in a paper-based microchamber." In: *Talanta* 147 (2016), pp. 628–633.

[187] Chiara Canali, Arto Heiskanen, Haseena Bashir Muhammad, Per Høyum, Fred-Johan Pettersen, Mette Hemmingsen, Anders Wolff, Martin Dufva, Ørjan Grøttem Martinsen, and Jenny Emnéus. "Bioimpedance monitoring of 3D cell culturing—Complementary electrode configurations for enhanced spatial sensitivity." In: *Biosensors and Bioelectronics* 63 (2015), pp. 72–79.

[188] Sun-Mi Lee, Nalae Han, Rimi Lee, In-Hong Choi, Yong-Beom Park, Jeon-Soo Shin, and Kyung-Hwa Yoo. "Real-time monitoring of 3D cell culture using a 3D capacitance biosensor." In: *Biosensors and Bioelectronics* 77 (2016), pp. 56–61.

[189] Stefan Howorka and Jan Hesse. "Microarrays and single molecules: an exciting combination." In: *Soft Matter* 10.7 (2014), pp. 931–941.

PUBLICATIONS

ASSOCIATED PUBLICATIONS:

"Single-Cell Optical Distortion Correction and Label-Free 3D Cell Shape Reconstruction on Lattices of Nanostructures"
by Stephan, Jürgen and Keber, Felix and Stierle, Valentin and Rädler, Joachim O. and Paulitschke, Philipp.
In: Nano letters 17.12 (2017), pp. 8018–8023. [81]

"Ultra-Flexible Nanowire Array for Label- and Distortion-Free Cellular Force Tracking"
by Paulitschke, Philipp and Keber, Felix and Lebedev, Andrej and Stephan, Jürgen and Lorenz, Bert and Hasselmann, Sebastian and Heinrich, Doris and Weig, Eva.
In: Nano letters, Article ASAP, 2018, DOI: 10.1021/acs.nanolett.8b02568 [103]

FURTHER PUBLICATIONS:

"Proteomics Identifies a Marker Signature of MAPKi Resistance in Melanoma"
by Paulitschke, Verena and Eichhoff, Ossia and Gerner, Christopher and Paulitschke, Philipp and Bileck, Andrea and Mohr, Thomas and Cheng, Phil, and Leitner, Alexander and Knapp, Bernhard and Zila, Nina and Chatziisaak, Theodora-Pagona and Stephan, Jürgen and Mangana, Joanna and Guenova, Emmanuella and Saulite, Ieva and Freiberger, Sandra and Irmisch, Anja and Kunstfeld, Rainer and Pehamberger, Hubert and Aebersold, Ruedi and Dummer, Reinhard.
Submitted to EMBO Molecular Medicine.

ACKNOWLEDGMENTS

I hereby would like to thank all the people that contributed directly or indirectly to this work, namely:

Prof. Joachim Rädler for your supervision of this work, your ideas, and your guidance.

Philipp Paulitschke for your feedback, your support, your vision, and for your ability to motivate your peers. I have learned a lot and really enjoyed working in your group!

I would like to thank all my collaborators, the current and former members of the group, my friends, and all the other people that supported me, namely:

Andrea Cooke, Andrej Lebedey, Anita Reiser, Anton Heindl, Alexander Bock, Alexandra Fink, Alexandra Murschhauser, Bert Lorenz, Börn Meier, Carolin Leonhardt, Christoph Schreiber, Clemens Liewald, David Brucker, David Volbers, Dieter Trautzsch, Prof. Doris Heinrich, Emanuel Reithmann, Ester Porcellato, Prof. Eva Weig, Felix Keber, Felix Segerer, Florian Forster, Florian Pils, Gerlinde Schwake, Janina Roemer, Jonas Zähringer, Josef Hirte, Julian Aschauer, Konstantin Ditzel, Leonard Schendel, Magnus Bauer, Mandy Häusler, Marco Selig, Marc Vogt, Margarita Rüter-Stimpfle, Margarete Meixner, Martina Edenhofer, Matthias Hauck, Matthias Zorn, Mihael Kodric, Miriam Balles, Peter Freiwang, Peter Röttgermann, Philip Böhm, Philipp Altpeter, Philipp Nickels, Rafal Krzyszton, Regina Wittig, Reinhold Rath, Ricarda Berger, Sebastian Hasselmann, Sergey Platonov, Silke Bergeler, Simon Lanzmich, Sonja Westermayer, Sophia Schaffer, Stefan Fischer, Stephan Manus, Stephan Zöllinger, Susanne Kempter, Svenja Lippok, Tatjana Lamparter, Thomas Zettl, Timon Funk, Tobias Verdorfer, Valentin Stierle, and all the other members of the Rädler chair.

Last but not least, I want to thank my family and Romana for their unconditional support.

Thank you!